The economically feasible synthesis of porous silicon for lithium-ion battery anodes via the magnesiothermic reduction of silica at ultra-low temperatures

By:

Maximilian Yan

A thesis submitted in partial fulfilment of the requirements for the degree of
Doctor of Philosophy

The University of Sheffield
Faculty of Engineering
Chemical and Biological Engineering Department

Primary supervisor: Professor Siddharth V. Patwardhan
Secondary supervisor: Professor Solomon F. Brown

29/07/2022

Summary

In the electric vehicle (EV) sector, lithium-ion batteries are the energy device of choice however its energy density still leaves EVs unable to compete with their fossil fuelled counterparts in terms distance travelled on a single refuel event. The search for more energy dense materials has found that the most promising high-energy anode material is silicon, with a theoretical specific capacity 3579 mAh/g, compared to 372 mAh/g for the presently used graphite anode. The capacity of silicon fades quickly due to its anisotropic volumetric expansion of 280% at maximum lithiation capacity, causing the silicon particles to fracture and exfoliate. Creating void space in the silicon allows the dissipation of mechanical stresses, minimising anode degradation. While the existing method of manufacturing silicon is geared towards the transistor and metallurgy sectors, it is not suitable for making porous silicon (p-Si). The method requires temperatures ≥2000°C followed by etching of the silicon in HF to produce p-Si. The magnesiothermic reduction (MgTR) is an alternative, more efficient bulk method of manufacturing p-Si which operates at 650°C. This method has been researched heavily since its first report in 2007, with studies showing that it can reduce commercial precipitated silica, glass, and even rice husks. The cost of producing p-Si via the MgTR using the methods reported in literature were calculated in this thesis. Strategies for lowering the temperature requirement, whilst increasing the yield and capacity of the p-Si are presented in this thesis. By incorporating nano-sized silica particles ≥7nm into the reaction mixture, the MgTR can be triggered at 380°C, achieving a high yield of 80%. p-Si produced at 380°C was able to achieve an initial discharge capacity of 1800 mAh/g, fading to a stable 1000 mAh/g after 100 cycles. Going from 650°C to 380°C, the energy cost was cut by 34% from £7.50 to £4.90/kg, and the total cost of production (TCOP) was cut by 17%, from £79/kg to £51/kg at 1500 kg/batch scale. This was much lower than the market price of SiO anode materials, which was ~£160/kg. The TCOP of the low-temperature method could be decreased further to £48/kg at scales ≥1500 kg, making the magnesiothermic reduction a highly competitive process for the large-scale production of p-Si.

Acknowledgements

This PhD has presented me with many challenges which I would not have overcome were it not for the people around me. I would firstly like to thank past members of the Energy Storage CDT. Sam Homan, for the many discussions on topics ranging from thermodynamics to particle physics that have benefitted my work and quenched my thirst for knowledge. I started this PhD with a degree in Chemical Engineering and limited knowledge in the field of Materials Science, so I am thankful to Laura Wheatcroft, the knowledgeable materials scientist who was always willing to answer my mostly silly questions on crystallography and phase diagrams. Huge thanks goes to Jake Entwistle for introducing me to the magnesiothermic reduction, enabling me to build a solid foundation of understanding of the field. I thank Laurie Middlemiss for creating a fun and cheerful research environment, livening up the days when work seemed slow, and motivation was low.

Secondly, I would like to thank Dr. Mita Dasog for the privilege of working with her and her talented group chemists. I am grateful to all the members of the Dasog group for creating such wonderful work and social environments, making me feel welcome as a visiting researcher, and as a tourist in Nova Scotia. In particular, I would like to thank Sarah Martell who has an incredible amount of energy and enthusiasm for research. Being able work alongside and bounce ideas off someone with extensive knowledge on the magnesiothermic reduction allowed me to greatly improve my own knowledge base and produce my best work.

Thirdly, I would like to thank the Prof. Gregory Beaucage, for enhancing my experience as a PhD student, encouraging me to engage in extra-curricular activities which allowed me to develop my skills within and without research. My deepest thanks goes to my supervisor Prof. Siddharth Patwardhan for his guidance, patience, encouragement, allowing me to be independent, challenging me, giving me the freedom to make my own mistakes and helping me achieve success.

Finally, I would like to thank Tess, my parents and my sister Samantha for their unending support and patience throughout my doctoral studies.

Contents

1. Introduction

Lithium-ion batteries (LIB) can be found in almost every device in the portable technologies sector. Its high operating voltages (>3V) makes it well suited to energy intensive applications such as grid-scale energy storage and electric vehicles. A lithium-ion cell (Figure 1.1) consists of two electrodes immersed in a liquid electrolyte, and connected externally through an electronic circuit[1].

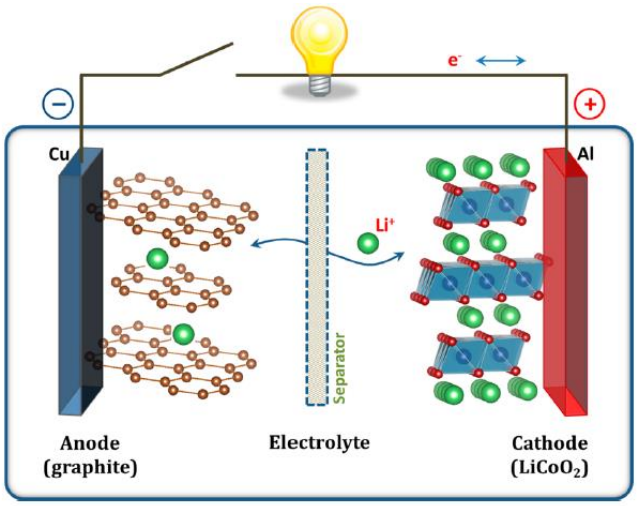

Figure 1.1: Schematic showing key components of a lithium ion cell. Image taken from ref[1].

The electrode material, which is in a powder form, is connected to a current collector – copper for the anode and aluminium for the cathode. A separator is placed in the electrolyte in between the electrodes to prevent contact and subsequent short-circuiting between the two electrodes. To travel from one electrode to the other, lithium ions move through the electrolyte whilst electrons are forced through the external electronic circuit. In this way, the energy from the flow of electrons can be harvested for useful work.

Lithium-ion batteries have greatly benefitted portable devices as well as the broad category of energy storage applications, in a way that preceding battery chemistries have not[2]. Their higher operating cell voltage equates to much higher energy densities than earlier battery technologies, so they have catalysed the development of other technologies that require energy storage, such as electric vehicles, renewable energy generation. The lead acid battery has been used in vehicles with

combustion engines for decades and is suited for low-capacity duties such as ignition and providing auxiliary power. The highest specific energy density that can be achieved with this chemistry is 50 Wh/kg (Figure 1.2)[3], an order of magnitude lower than that of lithium-ion cells. Another common cell type is the nickel-cadmium cell. This type of cell is available in AA cell constructions and are used in portable electronic applications. Although this cell possesses a higher specific energy density of 70 Wh/kg higher than lead acid.

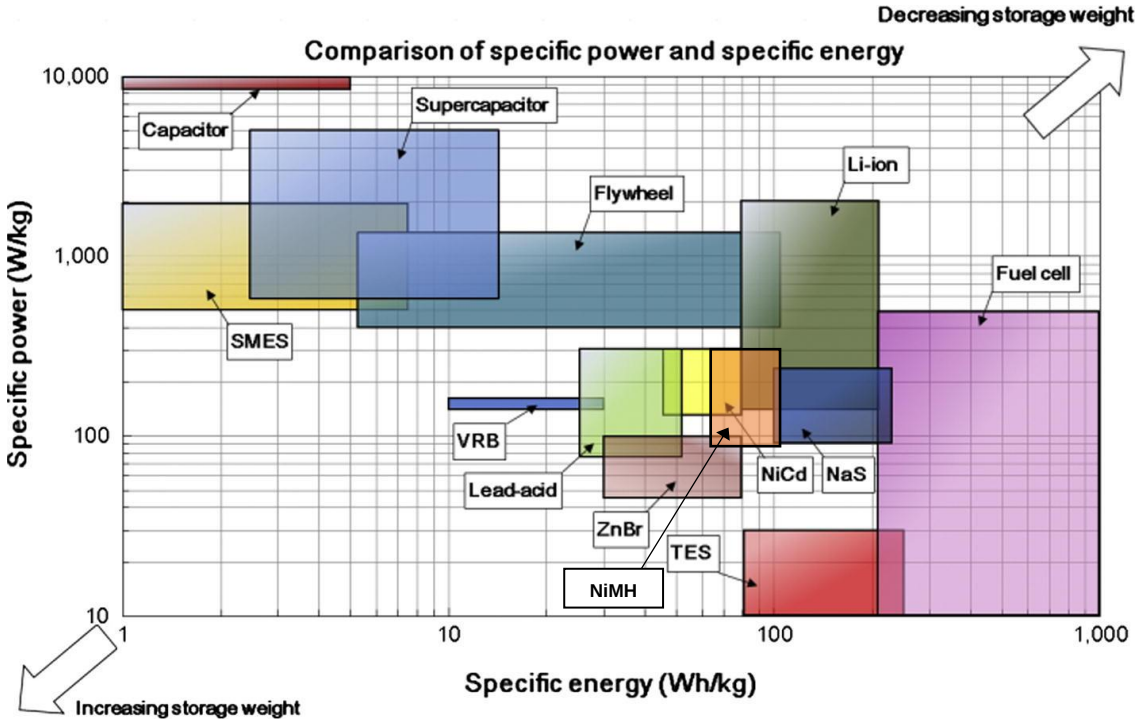

Figure 1.2: Ragone plot comparing the specific energy and specific power of different energy storage devices. Image adapted from[3]. For clarification, the yellow region represents the specific power and energy of NiCd while the orange region represents that of NiMH.

However, in these sectors, the performance of a lithium-ion battery is still the limiting factor. For example, the energy density (gravimetric and volumetric), although high in electrochemical energy storage terms, is low compared to hydrocarbons, the conventional medium for storing energy in the transportation sector[4]. In general, to store enough energy for a car to travel 500 km, 33 kg of fuel is required whereas a lithium-ion battery weighing more than 10x this amount is required (Figure 1.3)[4].

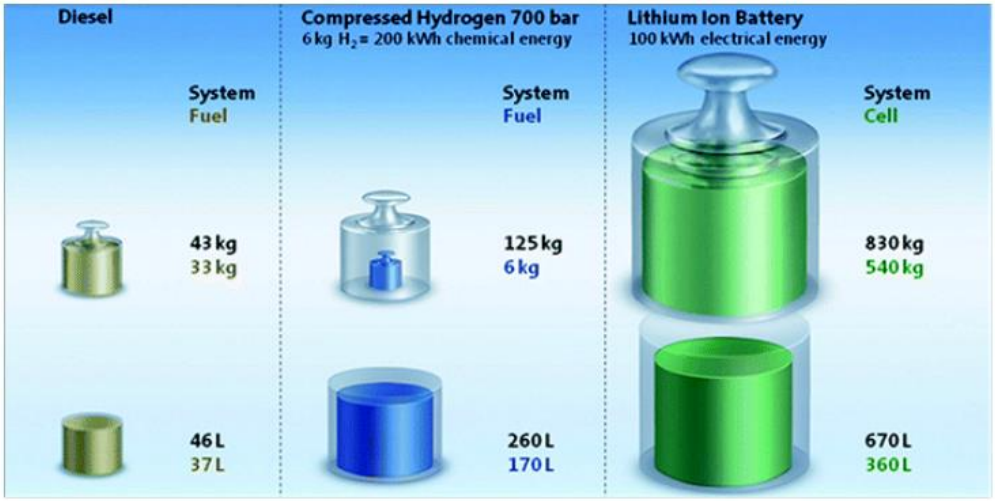

Figure 1.3: The diagram illustrates the difference in energy densities of different energy storage medium in vehicles. Image taken from ref[4].

Having a heavy battery restricts the total distance a car can be driven before recharging. Due to weight of a lithium-ion battery, the size of the battery that can be put in a car is limited, so the resulting car mileage does not exceed one with an internal combustion engine. Energy density matters, to a lesser extent, in portable electronics[5]. Mobile devices are being designed smaller in form, and more power hungry than ever, demanding batteries with high energy densities.

Looking at energy storage from a environmental angle, the ideal for a method of storing energy is one which consumes far less energy to manufacture than it can store over its lifetime. It was shown that the cost of manufacturing a 1 kWh lithium-ion battery releases 13 kg CO_2[6]. A Nissan leaf with an energy density of 67 kWh would therefore have 871 kg CO_2 associated with its production. This car has a rated distance of 168 miles on a single charge, releasing 93.2g of CO_2/mile assuming a grid CO_2 emission of 233 g/kWh[7]. An internal combustion engine (ICEV) vehicle releases 195 g CO_2/mile[8]. The difference in CO_2 emitted per mile travelled is therefore 102 g less for an EV compared to an ICEV. To offset the 871 kg of CO_2 emitted in the production of the battery, the EV has to have travelled 8540 miles or be charged 50 times. A lithium-ion battery is capable of many more charges than this, which makes LIBs a suitable, low or zero carbon alternative to internal combustion engines. Looking at the breakdown of the energy consumption, it was shown that the greatest proportion of energy consumed in the production of a battery was taken by materials production (Figure 1.4)[9]. Therefore,

it is crucial that improvements are made to the materials production part of a battery manufacturing process.

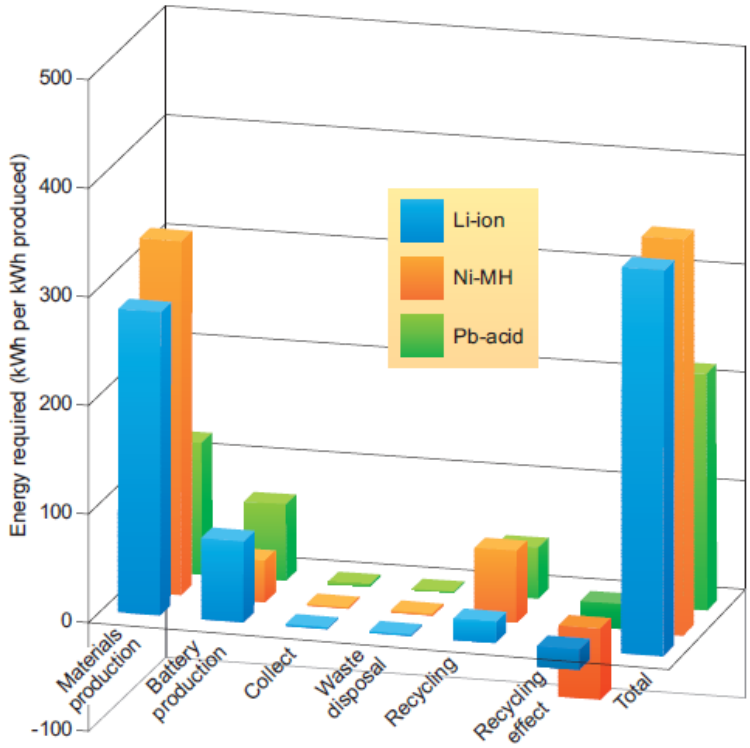

Figure 1.4: The energy consumption of different sectors in the production of a lithium-ion battery. Image taken from ref[5].

Lithium-ion batteries should not be solely merited based on energy storage metrics such as energy density and CO_2 offset and cost per energy stored. By these quantifications, it is difficult to see why lithium-ion batteries should be considered over other technologies, for example pumped hydro and compressed air energy storage[10]. Despite the disadvantages that come with lithium-ion batteries, there are reasons which point to the need for lithium-ion batteries and for its advancement. For portable electronic applications, it is clear that batteries are the answer, and under the umbrella of batteries, lithium-ions are best suited for the power- and energy-hungry electronic devices of the modern day[11]. In the transportation sector a shift from carbon-based fuels to low-carbon or zero-carbon fuels is crucial for cutting CO_2 emissions and combatting climate change, and batteries will play a major role amongst the fuel cell and plug-in hybrid technologies that will be used in different modes of transportation[12]. Lithium-ion batteries are therefore important as a means for storing energy

across various sectors, however they still suffer from high manufacturing costs and large physical size, which sparks the need for research in this field.

This section of the report introduces key components (charge carriers, electrode, electrolyte) of a lithium-ion cell and the relevant parameters (voltage, specific capacity, specific energy) used to measure the performance of these components, which will form a basis for the selection of appropriate materials to use in lithium-ion batteries.

1.1. Battery fundamentals

1.1.1. Capacity of a cell

In a lithium-ion cell, lithium ions move from the anode to the cathode when energy is being drawn from the cell[13]. The lithium ions travel in the opposite direction when the cell is being charged by applying a voltage from an external source. The materials used in the negative electrode (anode) and the positive electrode (cathode) determine the capacity of the cell, measured in units of milliamp-hours (mAh)[14]. A cell with a capacity of 1 mAh is able to supply a current of 1 milliamp for 1 hour. This unit can be rewritten in units of coulombs (C):

$$1mA * h = 1\frac{mC}{s} * 3600\ s = 3600\ mC \tag{1.1}$$

Therefore, mAh fundamentally indicates the amount of charge. To predict the theoretical maximum capacity of an electrode material, whether it is the anode or the cathode, the appropriate chemical equation for the half-reaction occurring at the given electrode is required. For example, the following half-reaction occurs in graphite, a commonly used anode material in lithium-ion batteries:

$$Li^+ + 6C + e^- \rightarrow LiC_6 \tag{1.2}$$

Each lithium ion reacts with 6 carbon atoms – that is, 6 carbon atoms are required to store 1 lithium ion. The amount of lithium ions in moles, n_{Li}, that a given mass of carbon, m_c can theoretically react with (and therefore store) is[15]:

$$n_{Li} = \frac{m_C}{6 * M_{rC}} \quad (1.3)$$

where M_{rC} is the molar mass of carbon, which is 12 g/mol. The charge on each lithium ion is +1, so associated with the movement of each lithium ion is the movement of 1 electron. The amount of charge (Q_{Li}) in coulombs associated with n_{Li} moles of lithium ions is given by:

$$Q_{Li} = z * n_{Li} * N_0 * e_c \quad (1.4)$$

Where z is the charge number of a lithium ion, in this case, 1, N_0 is Avogadro's constant, 6.022 x 10^{23}, and e_c is the elementary charge of an electron, 1.602 x 10^{-19} C. Using equation 1.1, Q_{Li} can be converted from units of coulombs to amp-hours (Ah) by dividing by 3600, then mAh by multiplying by 1000. Table 1.1 gives the values for each of the parameters calculated using equations 1.3 and 1.4, by taking a basis of 1 g of carbon (graphite).

Table 1.1: The amount of lithium, charge and capacity 1 g of graphite can store is shown, calculated using equations 1.3 and 1.4. Capacity was calculated by dividing charge by 3.6.

Parameter	**Value**	**Units**
Amount of lithium	0.01389	moles
Charge	1338	coulombs
Capacity	371.7	milliamp-hours

The units for capacity normalised to 1 gram (called specific capacity) of material so that different materials can be compared on a normalised scale (mAh/g).

For a given electrochemical reaction between an electrode material and lithium, the reaction half-equation can be written in the form:

$$xA + yLi^+ + ye^- \rightarrow A_xLi_y \quad (1.5)$$

Combining equations (1.3) and (1.4) gives, and generalising for any active material, *A*, which can undergo a reversible reaction with Li as given in equation 1.5, equation 1.6 can be written as:

$$Q_{Li} = \frac{z \times m_A \times N_0 \times e_c \times y}{x \times M_{rA}} \quad (1.6)$$

where x and y are known stoichiometries from equation 1.5. N_0 multiplied by e_c gives the Faraday constant (*F*), which takes the value of approximately 96500 C/mol. *z* is always 1 in the case of lithium, and the specific capacity of a material is given in units of mAh/g, therefore m_A takes the value of 1. Equation 1.6 can then be simplified to equation 1.7:

$$Q_{Li} = \frac{F \times y}{x \times M_{rA}} \quad (1.7)$$

Multiplying Q_{Li} by 1000 and dividing by 3600 converts C to mAh, so the overall equation for calculating the theoretical maximum specific capacity (C_g) in mAh, of a material storing lithium is given by[16]:

$$C_g = \frac{y * F}{3.6 * x * M_{rA}} \quad (1.8)$$

Unsurprisingly, the equation indicates that materials with a lower molecular weight result in higher specific capacities. The implications of this will be discussed in the materials selection section of this report (section 2.1).

The steps listed above can be applied for cathode materials. The lithium ions in a cell can only be in one electrode at a time, and only one electrode can be saturated with lithium ions at any given time. When a cell is fully charged, the anode is saturated with lithium ions, and when all the energy in a cell has been spent, the cathode is saturated with lithium ions. To release energy, they have to move from anode to cathode. If both electrodes were saturated with lithium ions, then movement of ions from the anode to the cathode would be impossible, so energy cannot be released. When two electrodes are put together as would occur in a cell, the overall capacity of the cell is equal to the lowest of the two electrode capacities. If one electrode stored significantly more lithium ions than the other, then lithium

ions would move from the former to the latter only until the latter has been saturated with lithium ions; movement of lithium ions would therefore halt since there is no more physical space or chemically available electrode material to accept more lithium ions. The limiting factor in the overall electrochemical reaction is the lower capacity electrode. For this reason, electrodes with similar capacities are used in cells.

It is important to remember that although lithium ions are described here as moving from one electrode to another spatially, redox reactions are occurring between the lithium ions and the electrodes. The electrode is oxidised when a lithium ion 'leaves' it, the electrode is reduced, when a lithium ion 'enters' it.

1.1.2. Electrode potential, cell voltage and energy

Electric current arises from the movement of electrons across a medium. The length of time for which a given current can be sustained by a battery can be calculated as shown in the previous section. While the capacity of the cell tells you how many electrons can be moved to produce a current, to enable the flow of electrons or negative charge, an electric potential is required, the units for which is joules per coulomb (J/C) or, more conveniently, volts (V). The potential of an electrode can be measured with respect to a reference electrode[17]. Conventionally, the standard hydrogen electrode is used, so the hydrogen electrode has an electrode potential of 0.00 V by definition. This, along with the more practical silver/silver chloride electrode are used for measurements of aqueous electrochemical systems. Lithium-ion cells operate at voltages exceeding the thermodynamic breakdown potential of water (1.23 V), and will react violently with water, hence measuring potentials of lithium-ion cell electrodes in an aqueous environment is inappropriate. Lithium metal is used as the reference electrode as it satisfies the criteria for reference electrode selection[18]; it is stable in the electrolytes that are commonly used in lithium ion cells, and the electrode potential stays practically constant throughout electrochemical measurement. Electrode potential is dependent upon the concentration of its active material (Li in this case) according to the Nernst equation[19], and the

concentration of lithium in the lithium reference electrode is considered to be in excess compared to the working electrode.

When two electrodes of different potentials are placed together in the same body of electrolyte and connected externally through an electronic circuit, a spontaneous redox reaction can occur. Electrons are transferred through the external circuit from the anode to the cathode. An oxidation reaction occurs at the anode, and a reduction reaction occurs at the cathode, and it is the coupling of these reactions that causes the flow of electrons. The direction of flow of electrons, therefore, is from the more reducing electrode to the more oxidising electrode. The overall chemical reaction that occurs will have associated with it a change in Gibbs free energy (ΔG), and from this, the voltage of the cell (ΔE) can be calculated by[14].

$$\Delta E = \frac{-\Delta G}{nF} \tag{1.9}$$

where n is the oxidation state of the active ion and F is the Faraday constant equivalent to the charge of one mole of electrons. It is important to note that the anode is defined as the electrode where oxidation spontaneously occurs and the cathode the electrode where reduction spontaneously occurs[20].

When two electrodes with different electrode potentials are coupled, then the open circuit voltage (V_{OC}) of the resulting cell, that is the voltage measured using a high impedance voltmeter, is simply the difference in potential between the two electrodes. This is given by[16]:

$$V_{OC} = E_{anode} - E_{cathode} \tag{2.0}$$

where E_{anode} is the electrode potential of the anode and $E_{cathode}$ is the electrode potential of the cathode. The total energy in joules that can be delivered by a cell is the product of the cell's voltage and capacity:

$$Energy\ density = V_{Op} * C_g \tag{2.1}$$

In the same way that specific capacity is used for comparison, specific energy (J/g) of a material is used for meaningful comparison.

1.1.3. Electrolyte

The function of the electrolyte is to conduct lithium ions from the anode to the cathode and vice versa[18]. The electrolyte also has to limit electronic conduction so that electrons are forced to flow through an external circuit instead of short-circuiting through the electrolyte. Short circuiting can occur through dendrite formation whereby the dendrites that form on a lithium metal electrode grows across the electrolyte and makes electrical contact with the other electrode[21]. The use of a solid electrolyte curbs this problem however this type of electrolyte suffers from low ionic conductivities. Polymer electrolytes of various types have been developed with beneficial properties such as higher ionic conductivities than solid electrolytes and improved electrode-electrolyte contact which allows for more efficient transfer of lithium ions [22]. Liquid electrolytes possess the highest ionic conductivities of all the electrolytes due to better electrolyte-electrode contact and low ionic diffusion resistance[23].

The maximum energy that can be delivered by a cell increases with the maximum voltage and therefore ΔG of a reaction. Hence, it seems almost obvious that one will find the best material combination for a high energy lithium-ion battery by coupling lithium redox reactions which give the highest ΔG. However the maximum voltage that can be maintained between the anode and the cathode in a reusable battery is limited by the electrolyte used in the battery[24]. There is a voltage window, the limits of which were associated with the highest occupied molecular orbital (HOMO) and lowest unoccupied molecular orbital (LUMO) of the electrolyte compound. This voltage window is linked to the stability of an electrolyte in contact with an electrode. If an anode with energies higher than the LUMO or a cathode with lower energies than the HOMO of the electrolyte, reduction or oxidation of the electrolyte would be facilitated by the anode or the cathode respectively[24]. It was reasoned that because HOMO-LUMO energies are based on electronic structure theory which does not take into account the change in energies due to the presence of an electrode, using HOMO-LUMO energies of an electrolyte offers an inaccurate and only approximate window of stability[25]. It follows

that although it is a good approximation, it does not coincide with the true window of stability, which is defined by the reduction and oxidation potentials of the electrolyte when in contact with an electrode (Figure 1.5).

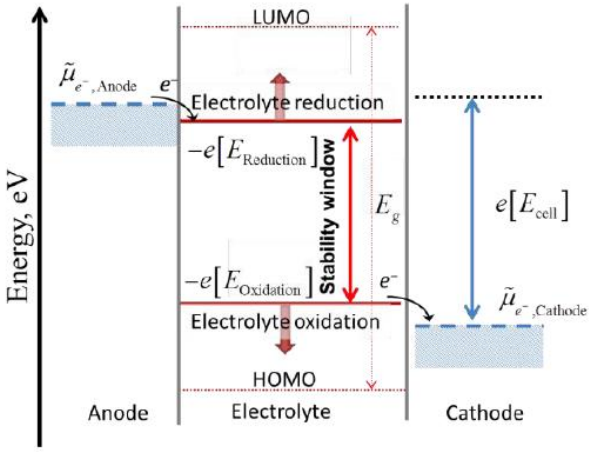

Figure 1.5: Diagram showing the difference between the HOMO-LUMO energies and the actual window of stability of an electrolyte image taken from ref[21].

The processes by which a cell stores and releases energy, and the parameters that describe the amount of energy that can be stored have been briefly explained here. The amount of lithium ions stored in a cell directly relates to its capacity. Oxidation and reduction reactions occur at the anode and cathode respectively but are coupled to facilitate the flow of lithium ions through an electrolyte and electrons through an external circuit. The reduction and oxidation reactions have associated with them Gibbs free energies, which translate into electrode potentials, and the difference in the potentials gives rise to the voltage of the cell. A higher voltage results in more energy stored, however it is important that the voltage does not exceed the window of stability of the electrolyte so that the electrolyte does not become reduced or oxidised by the electrodes.

1.2. Selection of active materials

It was shown in the previous section that the voltage of the cell is the difference between the potentials of the redox reactions occurring at each electrode. Based on equation 1.8, lighter materials are favoured for high specific capacities. Additionally, the greater the amount of lithium ions (y) to amount

of active material (x), the more electrons stored and the higher the specific capacities. The former point results in the exclusion of heavier elements from consideration when choosing suitable electrode materials and the latter point indicates that transition metals are favoured because they possess multiple oxidation states[24]. Figure 1.6 shows the elements that are eliminated based on these selection criteria[24].

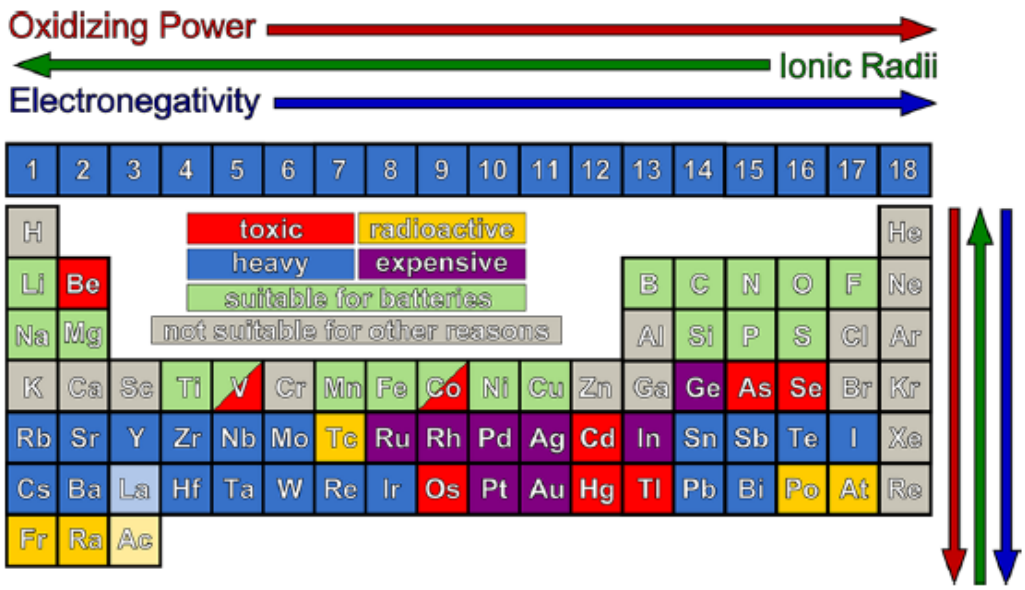

Figure 1.6: Candidate elements for electrode materials in lithium-ion batteries are identified by eliminating elements that are too heavy or too expensive, or unsuitable due to physical state. Black lines mark the boundaries between elements, while vertical red, green and blue arrows indicate oxidising power, ionic radii and electronegativity respectively. Image taken from ref[20].

The selection elements are for the fabrication of active materials for lithium-ion batteries. This means that although elements such as H and Zn are used in other battery chemistries (lead acid and NiMH for H and Zn-air battery for Zn), they are deemed unsuitable for LIB chemistries.

1.3. Cathode materials

The characteristics of chemical bonds are determined by electronegativity. The more similar the electronegativities of two elements in a bond, the more covalent the bond. Conversely, the bigger the difference in electronegativities, the more ionic[19]. Ionic bonds result in a more densely packed material compared to covalently bonded materials, increasing volumetric capacity. The atomic radii of transition metals decrease with atomic number in the same period. Outer electrons are more strongly

attracted to the nuclei so its binding energy increases. This results in a trend of increasing electric potential going across period 4 of transition metals, as shown in Figure 1.7[20]. Since cobalt has a higher number of electrons in its outer shell compared to iron and manganese, lithium cobalt oxide, $LiCoO_2$, has a higher voltage compared to other transition metal oxides.

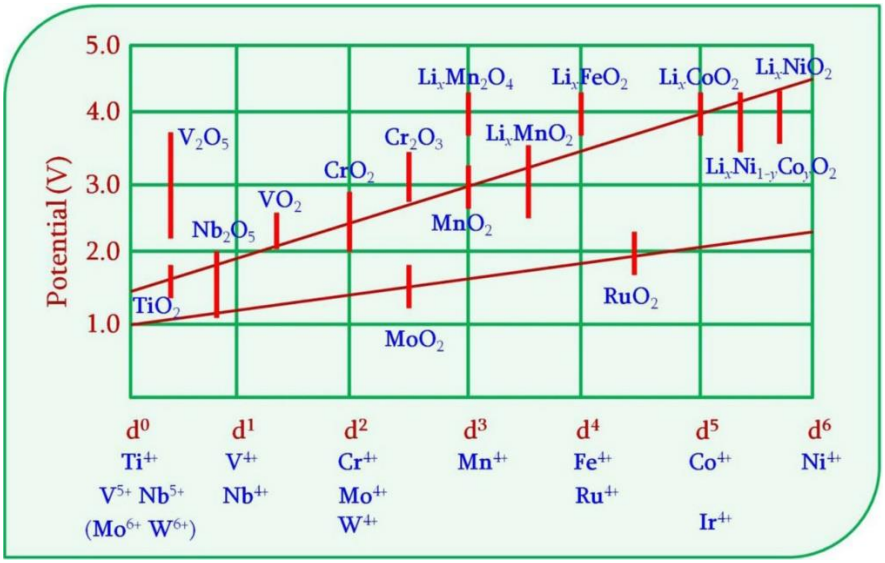

Figure 1.7: Potential of candidate transition metal oxides in period 4. The potential increases with element number. Image taken from ref[16].

The bond of transition metal oxides can be tuned to increase ionic character. Replacing the oxygen anion in Li_xFeO_2 for a phosphate polyanion, PO_4^{2-}, causes the electrons in the Fe-O bond to be pulled towards the covalent P-O bonds, resulting in a higher electrochemical potential of the iron, and a higher voltage seen in the phosphate compared to the oxide[26]. A trend can also be seen in electronegativity of polyanions and electrode potential (Figure 1.8)[16].

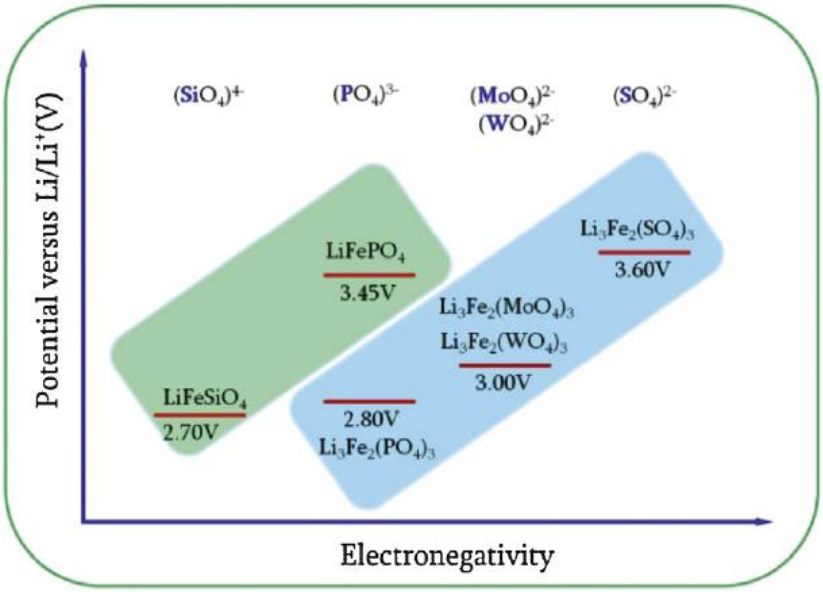

Figure 1.8: The increasing electronegativity of different polyanions leads to an increase in the potential of the electrode. Image taken from ref[12].

A more electronegative polyanion results in a highly ionic bond between the polyanion and the transition metal. The electrons are pulled away from the transition metal, so its redox potential versus lithium increases[27].

Another important property of the cathode materials used is the crystal structure. Crystal lattices take the form of layered, olivine or spinel structures, with spaces in the lattice which allow the insertion of lithium during discharge[28]. For example, the crystal structure can affect the cell's discharge characteristics (Figure 1.9)[29].

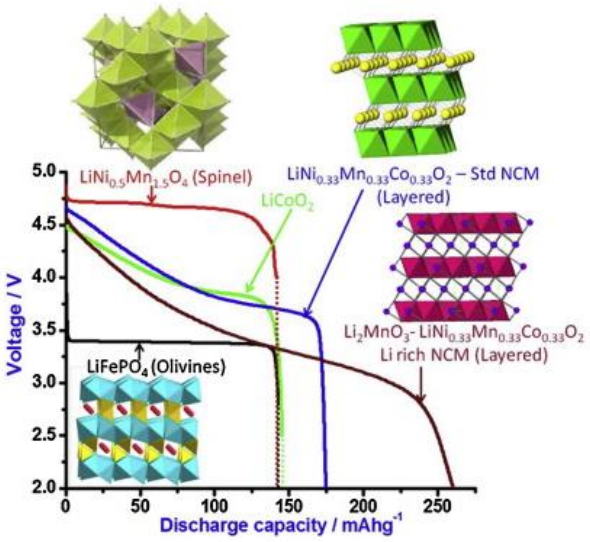

Figure 1.9: Olivine, spinel and layered structures used in cathode materials and their discharge characteristics. Image taken from ref[25].

A steep voltage drop upon discharge of a layered structured cathode material is due to the 'breathing' of the layers to accommodate the lithium ions. This distortion in structure consumes some energy, which translates to an early drop in voltage, followed by a final sharp drop at the limit of the cell's capacity[29]. Conversely in more rigid spinel and olivine structures, the voltage stays constant throughout discharge followed by a sharp drop at the limit of the cell's capacity.

1.4. Anode materials

In secondary, or rechargeable LIBs, lithium metal was originally used as the anode since it has the most negative electrode potential on the standard hydrogen scale. Being a light metal it has a high specific capacity of 3860 mAh/g[30]. Lithium metal forms dendrites over multiple cycles which grows into the electrolyte towards the cathode and creates an electronic short circuit, leading to thermal runaway[21]. Due to this safety issue, lithium anodes have been replaced with graphite, which is at present, is the most commonly used anode material in lithium-ion batteries. Lithium ions intercalate in between the layers of graphene during charge and for each lithium ion, 6 carbon atoms are required, as shown in Equation 1.2, rewritten below for convenience.

$$Li^+ + 6C + e^- \rightarrow LiC_6 \quad (1.2)$$

Anodes and cathodes can be categorised by lithiation mechanism. Intercalation materials, such as graphite and lithium cobalt oxides have crystal structures which lithium ions can move into or out of during charge or discharge. Conversion type materials undergo a change in crystal structure during lithiation/delithiation, and these undergo reactions of the form shown in Equation 1.5 of this thesis[31]. Metals which can alloy with lithium are examples of conversion anodes. Figure 1.10[31] compares the capacities and relative potentials of groups of electrodes.

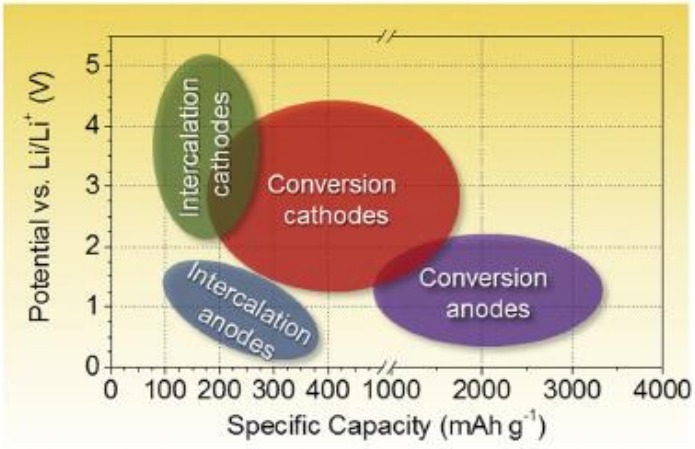

Figure 1.10: Anodes and cathodes are grouped according to lithiation mechanism, which are plotted to compare capacities and relative potentials. Image taken from:[27].

The lower the relative potential, the more reducing the material. It is important to note here that electrodes potentials are relative to a standard electrode – in this case lithium – hence the term *relative* potential, measured in volts. From here on, relative potential will simply be referred to as potential, using the reduction potential of Li^+ to Li as the 0 V standard.

In an electrochemical cell operating in galvanic mode (i.e. the cell is being discharged and current is being drawn), the more reductive electrode material will spontaneously become oxidised, and release electrons which flow to the more oxidative electrode. *By definition, the anode is the electrode which spontaneously becomes oxidised when a cell is operating in galvanic mode*[20] so it is the anodes that have lower potentials (close to 0 V). Cathodes with higher potentials are desirable, as with anodes

possessing lower potentials, since it is the difference in the potentials that gives rise to the cell voltage. From Figure 1.10 it can be seen that conversion anodes are the best candidates for improving the specific capacity of lithium-ion cells – their potentials are around 1 V, comparable to intercalation anodes, however they possess almost ten times the specific capacities.

In Figure 1.11 [32], it can be seen that graphite, the most commonly used anode material at present has one of the lowest potentials, which makes them well suited for their application but it also has one of the lowest capacities. Lithium metal is one of the highest capacity anodes, but as mentioned, suffers from poor cyclability due to formation of dendrites, resulting in thermal runaway.

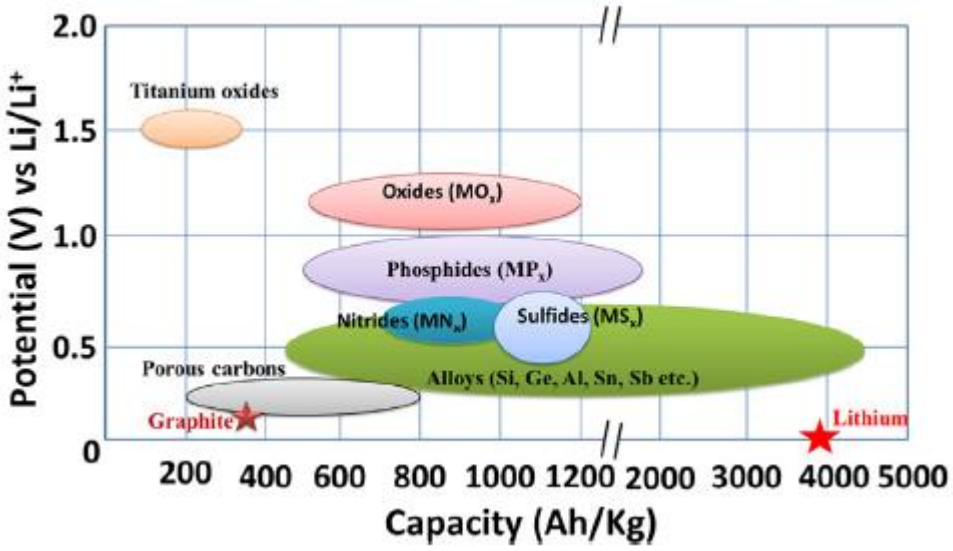

Figure 1.11: The potentials (against a reference Li electrode) of various anode materials. The units of capacity are equivalent to mAh/g. Image taken from:[28].

Under the umbrella of conversion anodes are metals which are able to form alloys with lithium. During lithiation/delithiation, the alloy composition changes according to their respective binary phase diagrams. Metals grouped in this category are represented by the green ellipse in Figure 1.11 [32]. These materials have the highest specific capacities and one of the lowest potentials, making them excellent candidates for use in lithium-ion cells. Another notable material is titanium oxide, which, although has an undesirably high potential for an anode, is useful for high power applications due to its ability to deliver a larger current than other anode materials, with minimal damage to its structure[33].

It was first found that lithium was able to undergo spontaneous electrochemical alloying (SEA) with certain metals by Dey in 1971[34]. Alloying electrode materials exhibit high storage capacity for lithium, much higher than intercalation materials, however, they incur a large volume expansion during lithiation[35]. Various metals which are capable of forming alloys with lithium have been identified as potential electrode materials[36], however as a consequence of the large volume expansion, the lithiation of these materials are largely irreversible. This is due mechanical stress experienced by the material when it expands during lithiation. As a result, the material cracks and loses electronic conductivity and therefore can no longer participate in electrochemical reactions[36]. It is however, possible to mitigate the destructive effects of the physical expansion by incorporating nano-scaled features into the structure of the material[37]. A list of some of the metals that can alloy with lithium along with their theoretical specific capacities are shown in Figure 1.12[38].

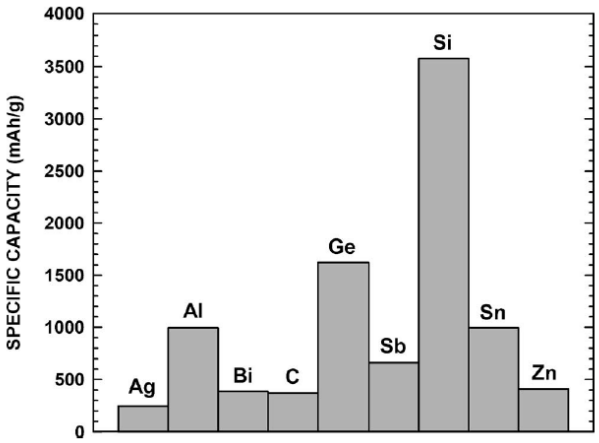

Figure 1.12: Specific capacities of some materials capable undergoing SEA with lithium are shown. Graphitic carbon is included for comparison. Image taken from:[34].

Certain metals, however, have additional disadvantages which eliminates them from the shortlist of promising anode materials. Germanium and silver are expensive metals[31] and tin, antimony, and bismuth, have hindered specific capacities due to their relatively large molecular weight. Of the remaining candidates, silicon possesses by far the highest specific capacity, and is a non-toxic, cheap and abundant element.

1.5. Choice of electrode development

In a lithium-ion cell, the electrochemical potential of the cathode vs. a lithium reference is higher than that of the anode, as shown in Figure 1.9[31]. This difference in potential gives rise to the operational voltage window and the total energy of the cell. Increasing the total energy density of the cell at the cell-chemistry level can be done by increasing the cell voltage window or increasing the amount of lithium-ions that can be stored per unit electrode active material. Of course, there are other components that are required for a cell to be useful in real-life applications. The electrode active materials have to be mixed with conductive and binding additives that create a complete electron conducting pathway. The cells are then packaged in a suitable container containing an ionically conductive electrolyte. These cells are often combined with more identical cells to build a battery pack. This means the final energy density of the cell is the energy arising from its chemistry, divided by the total weight of all the components in the battery pack. It follows that there are plenty of improvements that could be made to the lithium-ion cell at every level from the molecular level to the battery pack level which would indirectly translate to higher energy density.

In full-cell configuration, the cathode and anode capacities have to be matched closely, with the anode's capacity exceeding that of the cathode's for battery safety[39]. This is called the N/P ratio (negative to positive electrode) and if either exceeds the other greatly (N/P > 1.5), this will have implications in the degradation of the cell and the formation of lithium metal which raises safety concerns[13]. Therefore, developments in both the anode and the cathode are needed to increase the energy stored at the cell-level. It has been shown, however, just replacing graphite with a high capacity anode such as Si, a higher energy density can be achieved in a full-cell[40]. Though there are still challenges with using silicon as a pure anode material, silicon can be added in small amounts (5-10 wt%) to graphite anodes to improve the overall energy density. A study has shown that in a full-cell containing $LiCoO_2$ as the cathode and graphite as the anode, adding silicon has the potential to increase the energy density at the cell level by 15%[41].

In brief, it is important that specific capacities of both cathode and anode are improved proportionally to see the maximum gains in energy density at the cell-level. At present, incremental improvements can be still made to the energy of the cell by using a high-capacity anode such as silicon.

1.6. Silicon production

Silicon is an abundant element on earth, however, does not naturally occur in the elemental form. Silica from broad natural resources such as sand and rock is reduced into silicon via the carbothermal reduction process. This process occurs at 2000°C and produces high purity silicon which can be further purified by zone refining for electronic applications. Silicon melts at 1414°C so this process is unsuitable for producing silicon anodes as the product is non-porous. The pure silicon is electrochemically etched in an electrolyte solution, to leave behind a porous material. To achieve porous silicon (p-Si) from a silica raw feedstock, multiple energy-intensive steps are required.

The magnesiothermic reduction process (MgTR) process can reduce silica to silicon in a single step at 650°C. This is a bulk process whereby the silica is mixed with magnesium and heated in a furnace under inert atmosphere. This process is suitable for producing p-Si since the operating temperature is far below the melting point of silicon. At present there are limitations to the reaction chemistry as well as the process economics which inhibits its scale up.

1.7. Thesis structure

This thesis has been prepared in ‘by publication’ format. The first result chapter has been published in a peer review journal, and the second two results chapters have been prepared in a format suitable for publication in relevant peer review journals and will be submitted after the submission of this thesis. The chapters have been ordered in this way to create a thesis with a coherent structure. This subsection is written for the purpose of providing each chapter with context under the narrative of the whole thesis.

A review of the literature is laid out in Chapter 2, where the limitations in the magnesiothermic reduction are identified and the aims of the work in this thesis are laid out.

The experimental and modelling methods used in to achieve these aims are given in Chapter 3. The working principles of each method and the procedures ware described.

In Chapter 4, the dependence of reduction temperature on the particle size of SiO_2 is demonstrated using monodisperse silica nanospheres. This work has been published in the journal RSC Advances, titled '*Exploiting nanoscale effects enables ultra-low temperature to produce porous silicon'*. In this publication fumed silica around 7 nm are shown to undergo the MgTR at 380°C giving a yield of 54 mol% p-Si. It is well known that as the reduction temperature is decreased, so does the resulting yield of silicon and at 450°C the yield of silicon becomes negligible. The significance of the work in this chapter is that the conditions required for the ultra-low temperature MgTR reaction are now known.

Chapter 5 sees the application of the concept presented in the previous chapter, where particles that are unable to undergo the reduction below 500°C can be triggered to reduce at temperatures as low as 380°C by addition of a minority amount of 7 nm fumed silica. In this study, yields of silicon as high as 80 mol% was achieved. While Chapter 4 breaks the lower boundary of the temperature requirement, the concept was proven possible only for silica smaller than 75 nm in diameter. The significance of the work presented in this chapter was that it removes the limitation on types of silica that can be reduced at ultra-low temperatures. Commercial and bio-inspired silica was reduced at 380°C, giving high yields of silicon which exhibit favourable electrochemical performance in a lithium-ion cell.

In Chapter 6, the process economics will be evaluated by building an economic model of the process using experimental data presented in the previous chapters and found in the literature. The aim is to calculate the operational cost of producing p-Si via the MgTR process under lab-tested conditions. This is then compared with the price of silicon produced via the current commercial state-of-the-art. Experimental data collected in chapters 4 and 5 is fed into the model to calculate the decrease in cost compared to the reduction at 650°C. The model is also used to calculate the decrease in operational

cost under hypothetical, optimised scenarios. This highlights the limiting steps in the process, in terms of operational cost or product throughput, which can be used to inform future experiments in the field.

1.8. References

1 J. B. Goodenough and K. S. Park, *J Am Chem Soc*, 2013, **135**, 1167–1176.

2 B. Scrosati, *Journal of Solid State Electrochemistry*, 2011, **15**, 1623–1630.

3 X. Luo, J. Wang, M. Dooner and J. Clarke, *Applied Energy*, 2015, **137**, 511–536.

4 U. Eberle and R. von Helmolt, *Energy and Environmental Science*, 2010, **3**, 689–699.

5 M. Armand and J. M. Tarascon, *Nature*, 2008, **451**, 652–657.

6 P. Moon, A. Burnham and M. Wang, *SAE Technical Paper*, 2006, 1–375.

7 E. and I. S. Department for Business, Grennhouse gas reporting: conversion factors 2020, https://www.gov.uk/government/publications/greenhouse-gas-reporting-conversion-factors-2020, (accessed July 28, 2022).

8 Department for Transport, New car carbon dioxide emissions, https://www.gov.uk/government/publications/new-car-carbon-dioxide-emissions#:~:text=The%20average%20carbon%20dioxide%20emissions,of%20carbon%20dioxide%20per%20kilometre., (accessed July 29, 2022).

9 D. Larcher and J. M. Tarascon, *Nature Chemistry*, 2015, **7**, 19–29.

10 H. Kim, D. A. Boysen, J. M. Newhouse, B. L. Spatocco, B. Chung, P. J. Burke, D. J. Bradwell, K. Jiang, A. A. Tomaszowska, K. Wang, W. Wei, L. A. Ortiz, S. A. Barriga, S. M. Poizeau and D. R. Sadoway, *Chemical Reviews*, 2013, **113**, 2075–2099.

11 J. M. Tarascon and M. Armand, *Nature*, 2001, **414**, 359–367.

12 M. Contestabile, G. J. Offer, R. Slade, F. Jaeger and M. Thoennes, *Energy and Environmental Science*, 2011, **4**, 3754–3772.

13 J. K. Park, *Principles and Applications of Lithium Secondary Batteries*, Wiley-VCH, Weinheim, Germany, 2012.

14 K. B. Oldham, J. C. Myland and A. M. Bond, *Electrochemical Science and Technology: Fundamentals and Applications*, John Wiley & Sons Ltd, Chichester, 2011.

15 D. Deng, *Energy Science and Engineering*, 2015, **3**, 385–418.

16 C. Liu, Z. G. Neale and G. Cao, *Materials Today*, 2016, **19**, 109–123.

17 G. Inzelt, *Electrode potentials*, Oxford University Press Oxford, 2013.

18 D. Linden and T. B. Reddy, *Handbook of Batteries*, McGraw-Hill, Inc, New York, Third Edit., 2002.

19 P. Atkins and J. de Paula, *Elements of Physical Chemistry*, Oxford University Press Oxford, Fifth Edit., 2009.

20 I. Mills, T. Cvitas, K. Homann, N. Kallay and K. Kuchitsu, *International Union of Pure and Applied Chemistry: Quantities, Units and Symbols in Physical Chemistry*, Blackwell Science Ltd, Oxford, Second Edi., 1993.

21 W. Xu, J. Wang, F. Ding, X. Chen, E. Nasybulin, Y. Zhang and J. G. Zhang, *Energy and Environmental Science*, 2014, **7**, 513–537.

22 A. Arya and A. L. Sharma, *Ionics (Kiel)*, 2017, **23**, 497–540.

23 Q. Wang, L. Jiang, Y. Yu and J. Sun, *Nano Energy*, 2019, **55**, 93–114.

24 B. C. Melot and J. M. Tarascon, *Accounts of Chemical Research*, 2013, **46**, 1226–1238.

25 P. Peljo and H. H. Girault, *Energy and Environmental Science*, 2018, **11**, 2306–2309.

26 A. K. Padhi, *Journal of The Electrochemical Society*, 1997, **144**, 1188.

27 C. Masquelier and L. Croguennec, *Chemical Reviews*, 2013, **113**, 6552–6591.

28 Y. Mekonnen, A. Sundararajan and A. I. Sarwat, in *Conference Proceedings - IEEE SOUTHEASTCON*, 2016, vol. 2016- July.

29 H. D. Yoo, E. Markevich, G. Salitra, D. Sharon and D. Aurbach, *Materials Today*, 2014, **17**, 110–121.

30 M. S. Whittingham, in *Proceedings of the IEEE*, 2012, vol. 100, pp. 1518–1534.

31 N. Nitta, F. Wu, J. T. Lee and G. Yushin, *Materials Today*, 2015, **18**, 252–264.

32 S. Goriparti, E. Miele, F. De Angelis, E. Di Fabrizio, R. Proietti Zaccaria and C. Capiglia, *Journal of Power Sources*, 2014, 257, 421–443.

33 X. L. Yao, S. Xie, C. H. Chen, Q. S. Wang, J. H. Sun, Y. L. Li and S. X. Lu, *Electrochimica Acta*, 2005, **50**, 4076–4081.

34 A. N. Dey, *Journal of The Electrochemical Society*, 1971, **118**, 1547.

35 C. M. Park, J. H. Kim, H. Kim and H. J. Sohn, *Chemical Society Reviews*, 2010, **39**, 3115–3141.

36 R. A. Huggins, *Journal of Power Sources*, 1999, **81–82**, 13–19.

37 J. R. Szczech and S. Jin, *Energy and Environmental Science*, 2011, **4**, 56–72.

38 M. N. Obrovac, L. Christensen, D. B. Le and J. R. Dahn, *Journal of The Electrochemical Society*, 2007, **154**, A849.

39 S. Krueger, R. Kloepsch, J. Li, S. Nowak, S. Passerini and M. Winter, *Journal of The Electrochemical Society*, 2013, **160**, A542–A548.

40 D. Andre, S. J. Kim, P. Lamp, S. F. Lux, F. Maglia, O. Paschos and B. Stiaszny, *Journal of Materials Chemistry A*, 2015, **3**, 6709–6732.

41 M. Ko, S. Chae, J. Ma, N. Kim, H. W. Lee, Y. Cui and J. Cho, *Nature Energy*, 2016, **1**, 1–8.

2. Literature review

2.1. Silicon anode

Silicon is one of the most promising materials being explored as an anode for lithium-ion batteries. Si undergoes spontaneous electrochemical alloying with lithium, so as it becomes lithiated, it undergoes phase changes according to the Li-Si binary phase diagram (Figure 2.1)[1], moving from the right to the left ordinate.

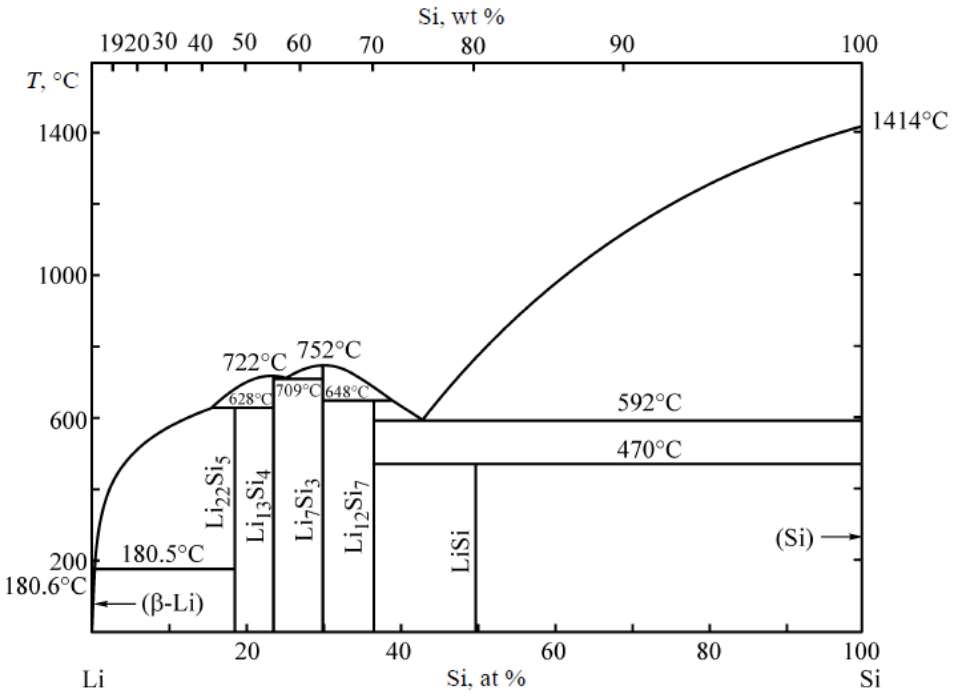

Figure 2.1: Li-Si binary phase diagram. The temperature range of importance for the scope of work is below 200°C, so the $Li_{22}Si_4$ phase does not exist within the lithium-ion cell's operating temperature range. Image taken from ref[38].

At low atomic percentages (at%) of Si, it can be seen in Figure 2.1 that two Li-Si phases exist. Above 180°C, fully lithiated silicon is present as the $Li_{22}Si_5$ phase[2], however at temperatures that lithium-ion cells are operated, the $Li_{15}Si_4$ phase exists[3]. This alloy of lithium and silicon has a theoretical capacity of 3579 mAh/g[4] at room temperature which can be calculated using Equation 1.8 in Section 1 of this thesis. This value is calculated using the stoichiometry for the reaction of lithium to silicon to give fully lithiated silicon:

$$15Li^+ + 4Si + 15e^- \rightarrow Li_{15}Si_4 \quad (2.1)$$

Crystalline silicon will lithiate and become an amorphous alloy. As it moves across the phase diagram (Figure 2.1) from right to left, the mole ratio of Li to Si increases from a minimum to a maximum, hence, the value of y in Eqn. 1.8, increases, thereby increasing its specific gravimetric capacity. During lithiation it undergoes volumetric expansion of up to 280% to accommodate the lithium[5]. During this expansion, individual particles of silicon crack and exfoliate due to the associated mechanical stress[6]. The exfoliated particles become electrically isolated and so do not participate in the redox reactions that store and release energy. This expansion is therefore detrimental to its structure and its ability to store lithium, resulting in a rapid decline in its capacity over multiple charge cycles[7].

2.1.1. Lithiation and delithiation

Understanding how the process of lithiation and delithiation occurs is crucial in the design of better anodes with high specific energy density as well as durability. Lithiation occurs when lithium ions approach the surface of a body of crystalline silicon (c-Si). An amorphous-crystalline layer forms at the surface of the silicon particle, moving as an amorphous-crystalline interface (ACI) reaction front toward the centre of the particle as the silicon becomes lithiated (Figure 2.2)[8]. The thickness of the ACI does not change as it moves towards the centre of the particle and the crystalline structure is not reformed during lithiation. In that study it was found that due to kinetic favourability, lithium atoms penetrated the crystalline silicon lattice only in the <110> and <112> directions, but in the <111> direction, a ledge peeling mechanism was observed.

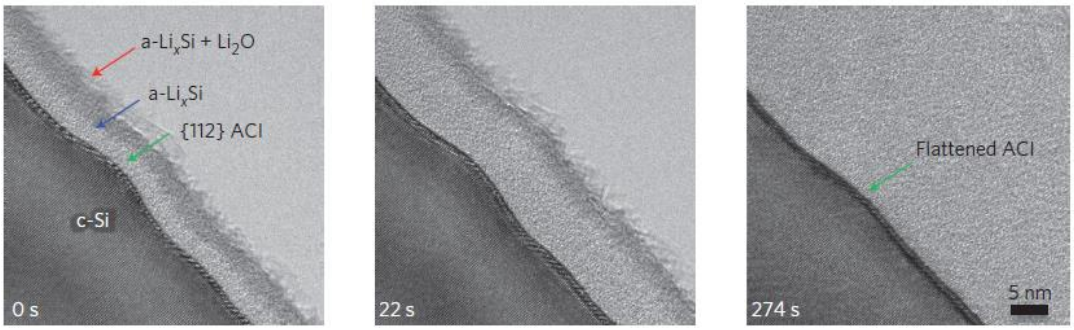

Figure 2.2: Movement of the amorphous-crystalline interface into the crystalline silicon phase during lithiation. Image taken from ref[44].

During lithiation of amorphous silicon, a shrinking core mechanism is observed similar to the lithiation of crystalline silicon, however the core shrinks isotropically (Figure 2.3)[9] so mechanical stress is not concentrated in a certain region in the particle.

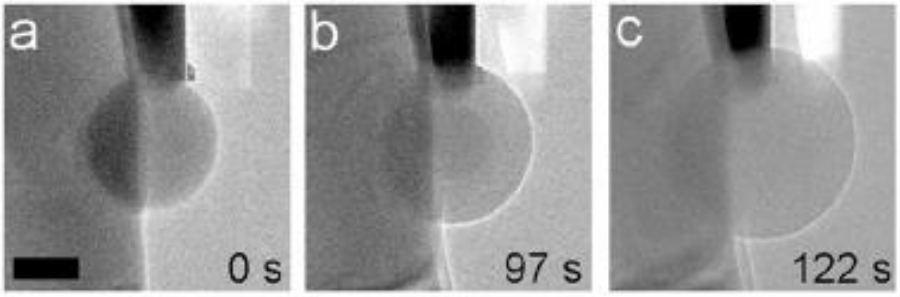

Figure 2.3: (a) Amorphous silicon sphere exhibits two-phase shrinking core behaviour during lithiation. This structure is observed in (b). Further reaction results in the formation of an amorphous particle of lithiated silicon,shown in (c). Image source: [45]

The fully lithiated silicon is an amorphous alloy, unless cycled below 50 mV in which case the silicon spontaneously crystallises to the $Li_{15}Si_4$ phase[10]. Regardless of whether the silicon used was crystalline or amorphous, upon lithiation, an amorphous phase forms, which then delithiates as a single phase without a visible reaction front, and subsequent lithiation and delithiation will also proceed in a single phase (Figure 2.4)[9].

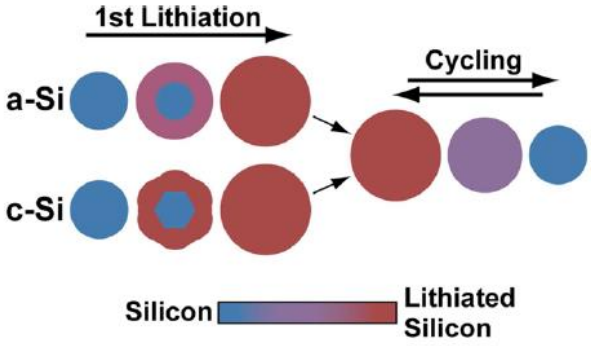

Figure 2.4: Schematic showing the lithiation and delithiation behaviours of amorphous silicon (a-Si) and crystalline silicon (c-Si). Image source: [45].

The difference in lithiation and delithiation mechanisms are linked to the way stress is concentrated in silicon particles during lithiation. Crystalline silicon cracks at 150 nm due to anisotropic lithiation – the mechanical stresses are focussed on the crystal faces of the particles. Amorphous silicon lithiate isotropically so the stress is distributed throughout the particle, cracking only occurs when particles are larger than 870 nm [11].

2.1.2. Mitigation of expansion associated damage

Various strategies have been demonstrated to be effective at mitigating the structural damage and subsequent capacity fade of silicon anodes. One of the challenges facing micro- and nanoparticles of silicon is ensuring electrical connection between particles and the current collector. To enable this, the silicon can be made into films, by vacuum deposition as demonstrated in one study by Ohara *et al.*[12] The benefits of this method are that the thickness of the film can be easily controlled and that a conductive connection can be ensured between the silicon at the top of the layer (furthest from the current collector) and the current collector. In that study, a film thickness of 50 nm had a lower capacity fade, maintaining a capacity of 3500 mAh/g after 200 cycles at 2 C rate compared to a thicker film of 150 nm with a capacity of only 2200 mAh/g after the same number of cycles. This is a surface manufacturing method, which is difficult to scale or integrate into existing bulk-process techniques used in the manufacture of electrodes.

Silicon can also be made in nanowire form attached on one end to a substrate current collector, which ensures that all the silicon is electronically connected and can participate in energy storing reactions[13]. The nanowires can be spaced apart on the substrate, allowing room for expansion, and being connected to the current collector eliminates the need for conductive additive and binder. They are capable of expanding and contracting during lithiation and delithiation, filling the void space and avoiding collision induced mechanical damage, achieving a stable capacity of ~3500 mAh/g after 10 cycles. With the aim of avoiding fracture of the anode material, similar structures have been made in other work such as silicon pillars of 1 μm diameter on a silicon substrate[14], achieving ~2800 mAh/g after 23 cycles. Silicon nanotube arrays 150 nm in diameter have also been synthesised in a study by Song *et al.*[15] maintaining a capacity of ~2300 mAh/g after 40 cycles. While nanowires are effective at mitigating structural damage, proven by their high, stable capacities, the method of synthesis, like in films, are surface-based techniques which are slow, costly, and unscalable. In order to meet the demand for Si in LIB, in particular, for transport applications, a bulk method of synthesis is required. The demand of SI in transport applications, and ways to meet this demand will be discussed in Chapter 6 of this Thesis.

Wang *et al*. have shown that hydrogen-bond-directed self-healing binders (SHP) can be used to reverse the effects of mechanical damage that occurs during the lithiation and delithiation of silicon[16]. In that study silicon microparticles 3-8 μm in size were mixed with SHP and conductive carbon then put in a cell and it was found that cells were able retain a high capacity of 2000 mAh/g after 100 cycles. In comparison, the capacities of cells with alginate, CMC and PVDF as binders dropped to 1000, 600 and 400 mAh/g respectively after just 30 cycles. The enhanced cyclability of cells made with SHP was due to the ability of the SHP to stretch, and to reform using the randomly branched hydrogen bonds. While nanotube structures were able to mitigate fracture and exfoliation of active material, this work using SHP takes a different approach, demonstrating that the exfoliation can, to a certain extent, be reversed. This concept supports the use of bulk silicon particles which are easier to synthesise than surface grown nanotubes.

Rather than repairing or minimising the mechanical damage caused by electrochemical cycling, the damage can be avoided altogether by limiting the volumetric expansion. One of the problems associated with the expansion of silicon material over multiple charge and discharge cycles is based on the formation of the solid electrolyte interface (SEI). When an electrode surface comes into contact with an electrolytic solution, a SEI forms where the electrolyte and the electrode meet, which consumes lithium ions and prevents further formation of SEI[17]. In silicon anodes, the repeated outward expansion and contraction expose more anode to the electrolyte, which encourages the growth of SEI, and consumes lithium ions, leading to a steady decrease in the overall capacity[18]. Double-walled silicon nanotubes have benefit of mechanical clamping of outer tube, limiting the outward expansion of silicon and therefore preventing material fracture and growth of SEI. Wu *et al.* have demonstrated that hollow silicon nanotubes surrounded on the outer surfaces by SiO_x as a mechanical clamp were able to retain a capacity of 600 mAh/g after 6000 cycles[19]. The rigid SiO_x outer layer prevented the outward expansion of silicon. Instead, the silicon expanded into the hollow centre. After 6000 cycles the coulombic efficiency of the cell was 99.938%, indicating that degradation rate of the cell was still very low. The motive behind this strategy was to prevent the growth of SEI as a result of repeated exposure of fresh silicon to the electrolyte which occurs during volumetric expansion. Limiting the expansion of the silicon meant that higher volume phases which store the maximum amount of lithium per silicon atom ($Li_{15}Si_4$) were prevented from forming, so there was a clear trade-off – the cyclability was drastically improved at the cost of specific capacity.

Various nanostructures effective at mitigating, preventing or repairing damage from mechanical stress of expansion have been discussed. To reduce the loss of conductivity, wires, pillars or films were used to ensure good electrical connections between the active material and current collector. To limit the extreme volumetric expansion, silicon could be grown as wires and mechanically clamped with a rigid outer layer, forcing the silicon to expand inward into its own hollow space. To make these structures, surface techniques or complex, energy intensive methods are required which hinders their sustainability and viability for scale-up. p-Si nanoparticles can be made using simpler, bulk

manufacturing techniques rather than surface techniques. The benefits of using this type of silicon will be the focus of discussion in the next section.

2.1.3. Porous silicon nanoparticles

The lithiation of pure silicon results in a volume expansion of 280%, however the accepted swelling limit for anodes is 5% to allow for the inevitable evolution of gases released from electrolyte breakdown[20]. By incorporating porous volume in the anode, theoretically the swelling can occur within the pores so that the overall outward swelling limit of 5% is not exceeded when the cell is lithiated. By expanding into the pores, not only is the outward expansion avoided, but the mechanical stress between particles is also reduced which minimises damage caused by electrochemical cycling. As a result of this, p-Si shows improved cyclability over non-porous silicon (Figure 2.5)[21].

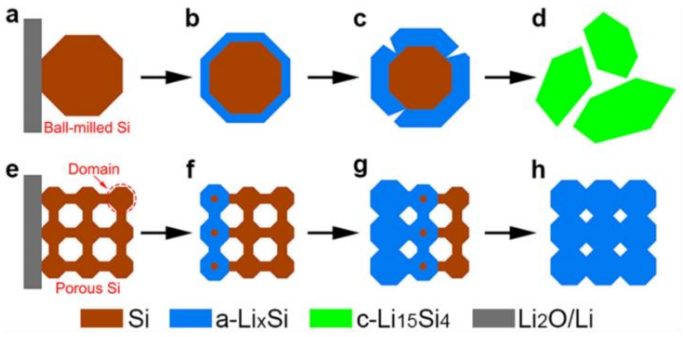

Figure 2.5: Schematic depicting the lithiation behaviour of non-porous (a-d) and porous (e-h) silicon. Image source:[57].

Particles can consist of internal pores (pores within each distinct particle) or external pores (space between small particles). Void space means lower specific capacities and energy densities however since the specific capacity of silicon is very high in comparison to the cell's capacity (Figure 2.6), this compromise can be made in the interest of cyclability[22].

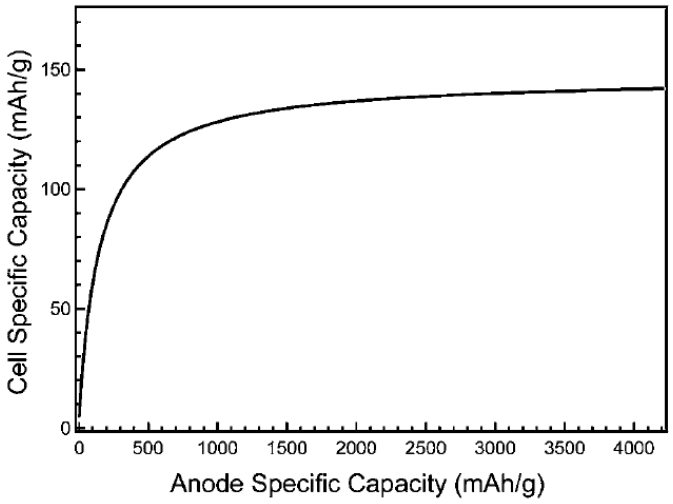

Figure 2.6: Full-cell specific capacity (with $LiCoO_2$ as cathode) is shown relative to the anode specific capacity, considering only the masses of active materials used and not cell construction materials. Image source:[33].

The maximum theoretical specific capacity of silicon is 3579 mAh/g, however the cell capacity starts to plateau at much lower anode capacities (1000 mAh/g, Figure 2.6)[22]. Should a silicon-based anode material be developed such that the theoretical maximum is achieved, then in a full cell the mass of silicon required to achieve the maximum cell capacity will be less.

Silicon nanoparticles can be added as a minority component to another anode material with lower capacity (such as graphite) which does not suffer from such drastic volume changes. By replacing a small amount of the lower capacity material with silicon, the overall capacity of the cell is increased[23].

The particle size of silicon determines the performance of a lithium-ion battery. When an anode material comes into contact with an electrolyte, a SEI layer forms at the interface between the two. Smaller particles generally have higher external specific surface area (SSA), which means a larger SEI layer forms compared to bigger particles which tend to have less SSA. However, smaller particles have shown to be beneficial in terms of mitigating stress and shrinking to original size rather than cracking and forming new SEI layers[24]. In that study, silicon nanoparticles of sizes 5 nm, 10 nm and 20 nm were synthesised and their electrochemical performances were compared. 20 nm particles had the lowest SSA and showed the highest initial coulombic efficiency of 85%. The 10 nm particles, with their increased SSA, showed a lower coulombic efficiency of 80%, whereas the 5 nm particles

showed a coulombic efficiency of 60%. After 40 cycles, the 10 nm particles and 20 nm particles showed the highest and lowest capacity retention of 81% (2750 mAh/g) and 67% (2300 mAh/g), respectively. The 10 nm particles were able to shrink back to their initial particle size after cycling, rather than fracture into smaller particles or grow in size over multiple cycles due to continuous formation of SEI. Furthermore, the initial coulombic efficiency and capacity retention after 40 cycles were improved to 89% and 96% (3393 mAh/g) respectively when the 10 nm particles were coated in a layer of conductive carbon. This improvement in performance was due to the effect of carbon stabilising the SEI layer, by preventing further growth from repeated electrochemical cycling[24,25]. In another study by Liu *et al.*, it was found that the critical size for fracture of a single particle of crystalline silicon was 150 nm[11]. As a single particle of c-Si was lithiated, a two-phase, core-shell structure was formed whereby the outer lithiated layer, surrounded the c-Si core. As the c-Si became lithiated it experienced the large volume expansion and the reaction front moved toward the core. The difference in the volume between the surface layer and core led to the development of hoop tensile stress experienced by the lithiated surface layer. This hoop stress was dissipated anisotropically in the lithiated phase which then led to propagation of cracks from flaws on the surface. This size-dependent fracture was not seen in amorphous silicon in particles even as large as 870 nm, due to the isotropic propagation of the hoop stress[9]. It is important to note that while nanoparticles are porous, each particle is not necessarily porous so the pores and SSA are external (interparticle pores), rather than internal pores. The definition of p-Si here refers to particles which may not be nano-sized, however possess pores in the nano regime.

p-Si show great promise as an anode material for lithium-ion batteries. Being a bulk material, they can be added to anode materials with low capacity and low volumetric expansion to incrementally increase the overall capacity of the cell. Their porous structure allowed the particles to expand volumetrically without degrading. Their electrochemical performance is dictated by their structural properties, which needs to be controlled and in the next section, the methods for doing this by tailoring synthesis parameters will be described. In particular, the magnesiothermic reduction will be discussed

as a method for making porous silicon which will highlight further advantages of choosing p-Si nanoparticles over other structures of silicon for lithium-ion batteries.

2.2. Silicon synthesis

Elemental silicon is most widely used for making alloys (metallurgical grade) for various purposes such as electric motors[26], engine blocks[27], and semiconductors (transistor grade) for electronic devices, the latter requires the highest purity silicon[28].

Silicon can be found naturally in sand as quartz, a crystalline form of silicon dioxide. The silicon is extracted via a reduction process using carbon as the reducing agent (Eqn 2.2). This process is called carbothermal reduction and occurs at 2200ºC [29].

$$SiO_2 + 2C \rightarrow Si + 2CO \qquad (2.2)$$

From this, metallurgical grade silicon is made which is between 95-97 mol% pure[29]. This can be further refined by firstly converting into silane, trichlorosilane, or tetrachlorosilane via hydrogenation or chlorination, then transistor grade silicon via thermal decomposition[30]. To produce a boule of monocrystalline silicon, the pure silicon is first melted in a crucible. A pulling rod is dipped into the silicon and drawn from the crucible while rotating, forming a boule of monocrystalline silicon. This is the Czochralski pulling process[31] used to make silicon wafers for the transistor industry.

2.2.1. Electrochemical etching of silicon wafer

Porous silicon was first discovered by Uhlir in 1956 in Bell Laboratories in a study which aimed to produce smooth silicon wafers for electronic circuits using an electrochemical etching method[32] . Silicon is etched away from the wafer by the HF, as given in Eqn 2.3:

$$SiO_2 + 6HF \rightarrow SiF_6^{2-} + 2H^+ + 2H_2O \qquad (2.3)$$

This method involved the use of a hydrofluoric acid (HF) electrolyte and a platinum electrode. During the study it was found that rather than producing a smooth surface on the silicon wafer, the surface of the silicon wafer was etched unevenly, resulting in a rough and porous structure. This method is a top-down approach whereby external voltage is applied to the silicon and platinum, causing the dissolution of silicon on the surface and leaving behind a porous wafer (Figure 2.7)[33].

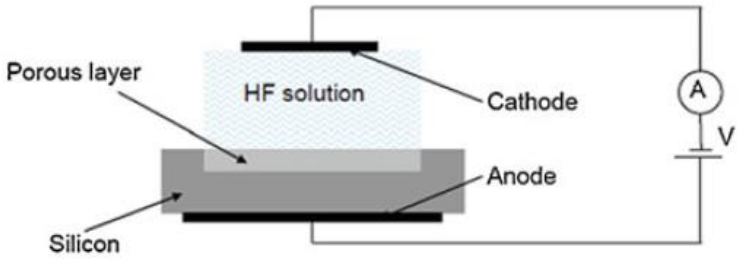

Figure 2.7: Schematic depicting the key components required for the electrochemical etching of silicon. Image source:[70].

In this process, the operating parameters can be changed in order to give different pore morphologies. These parameters are etching current density, HF concentration, and wafer doping. The etching process begins when an anodic potential is applied to the cell and the surface of the silicon begins to dissolve unevenly. Pore formation occurs at all current densities below a critical current density, above which, pore formation ceases to occur, and instead, electropolishing dominates, creating a smooth rather than a porous morphology on the surface of the silicon. Up to the critical limit, as current density increases, more material is etched and so porosity increases. The current density changes with HF concentration – higher concentrations favour high current densities. Higher concentrations of HF also results in smaller pore sizes formed on the surface of the silicon. N-type doping in the porous silicon leads to the formation of macro- and mesopores, while p-type doping results in micropores.

While this method has its merits including low temperature requirement, high purity of the final product and good control of product properties, it is not without its drawbacks. The first and most important drawback of this method is the requirement of the extremely hazardous chemical, HF which raises issues primarily with process safety but also with sustainability and scalability. Aside from the safety aspects, high-purity silicon is also required as the feedstock which is produced via the carbothermal

reduction method. A second drawback relates to the suitability of the silicon produced for the application of lithium-ion batteries. This is a surface technique and wafers are made with pores etched into one of the surfaces. The active material in an electrode of a lithium-ion battery is in the form of a powder spread on a current collector rather than a single solid material with an etched surface, so silicon wafers made by electrochemical etching would be difficult to integrate into existing cell configurations[34] and manufacturing infrastructure[35].

From a cell performance viewpoint, porous silicon powder is more suitable for the application over porous wafers. It was found in a study that particles of silicon smaller than a critical diameter (150 nm) exhibit greatly improved cycling capabilities in a lithium-ion cell compared to particles larger than this diameter due to better management of mechanical stress[11]. Porous silicon made via electrochemical etching does not give individual nanoparticles, but a single, continuous wafer of silicon with pores throughout.

In short, the drawbacks of this method of producing porous silicon are the need for hazardous chemicals and high purity feedstock, the incompatibility of the silicon product with lithium-ion cell architecture and unsuitable morphology. Clearly, to manufacture silicon for use as anodes in lithium-ion batteries, a more suitable process is required. The details of a more appropriate process are discussed in the following section. This is the MgTR process, which is a bulk synthesis method that produces powdered porous silicon from a wide variety of silica feedstock without the requirement of extremely hazardous chemicals.

2.3. Magnesiothermic reduction of silica

One method of producing porous silicon that has a huge potential for scaling up is the magnesiothermic reduction reaction (MgTR). Unlike electrochemical etching, this is a bulk method whereby a stoichiometric amount (Eqn. 2.4) of silica is mixed with solid magnesium and heated in an inert atmosphere. The products include silicon, magnesium oxide, magnesium silicide as well as unreacted magnesium and silica. The silica used for this reaction is dry and usually in powder form

to promote mixing with magnesium, however silica sources such as sand[36] and crushed glass[37], which are coarse in comparison have also been used.

$$2Mg_{(s)} + SiO_{2(s)} \rightarrow 2MgO_{(s)} + Si_{(s)}, \qquad \Delta H = -291.62\ \text{kJ mol}^{-1} \tag{2.4}$$

$$2Mg_{(s)} + Si_{(s)} \rightarrow Mg_2Si_{(s)}, \qquad \Delta H = -77.8\ \text{kJ mol}^{-1} \tag{2.5}$$

$$Mg_2Si_{(s)} + O_{2(g)} \rightarrow 2MgO_{(s)} + Si_{(s)}, \qquad \Delta H = -1125.67\ \text{kJ mol}^{-1} \tag{2.6}$$

$$Mg_2Si_{(s)} + SiO_{2(s)} \rightarrow 2MgO_{(s)} + 2Si_{(s)}, \qquad \Delta H = -215.67\ \text{kJ mol}^{-1} \tag{2.7}$$

The same reaction can also occur between gaseous Mg and solid SiO_2, with a higher reaction enthalpy of 546.42 kJ mol^{-1}. The feasibility of a coupled redox reaction can be determined from the Ellingham diagram, shown in Figure 2.8[38]. Oxidation reactions of metals are shown, with their corresponding reaction Gibbs free energy (ΔG°) at different temperatures. The oxidation of magnesium at any given temperature has a lower Gibbs free energy than the oxidation of silicon, hence, at all temperatures the MgTR can proceed, and the reduction of magnesium oxide by silicon cannot. Additionally, the oxidation of C to CO has a ΔG° which decreases with temperature, meeting with the line corresponding to the oxidation of silicon at around 1800 K. Above this temperature the ΔG° of the latter reaction is greater than that of the former, and carbon is able to reduce silica. This is why the carbothermal reduction of silica requires high temperatures to proceed, however, the MgTR does not. Si can be further reduced by Mg to form the intermediate product Mg_2Si. This intermediate can then be oxidised, forming Si and MgO. In a furnace at temperatures above 450°C and under flowing Ar, reactions 2.4, 2.5 and 2.7 can occur. Reaction 2.6, which is the oxidation of Mg_2Si by O_2 cannot proceed in a properly sealed furnace but can proceed at 500°C if O_2 is fed into the furnace[39].

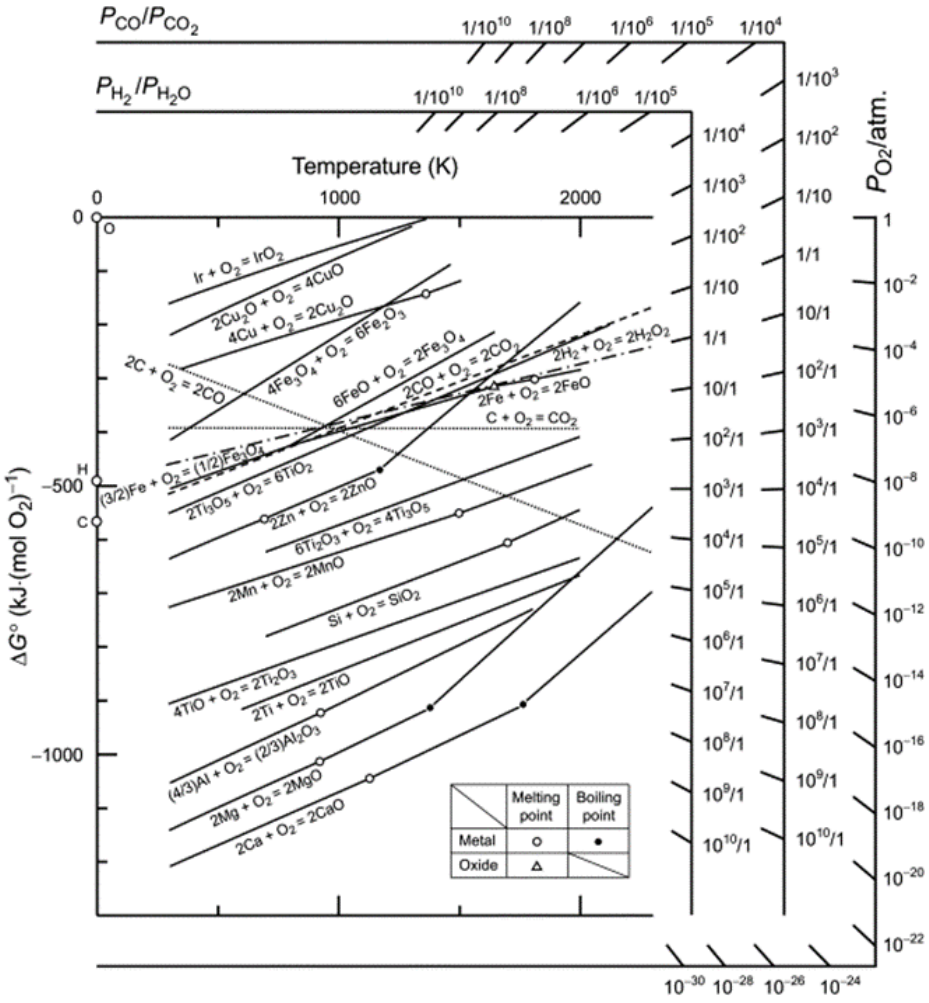

Figure 2.8: Ellingham diagram showing the change in Gibbs free energy of oxidation of metals with temperature. Image source:[40].

2.3.1. Reaction parameters

Typically, the mixture is heated in a furnace ≥650°C (the melting point of magnesium) for 1-6 hours under flowing argon. It has been shown that reaction times as short as 30 minutes at 650°C is enough to produce porous silicon however the yield was not reported in that study[41]. Reaction times between 1 and 10 hours are most common and it has been shown that the reaction reaches completion within 2 hours and does not increase with longer reaction times[42]. The temperatures used for the MgTR are far below the melting point of silicon (1414°C) so a porous structure can form without collapsing. At 650°C, the solid, liquid and vapour forms of magnesium are present, and each of these phases will react with silica. Magnesium begins to form a significant vapour pressure at 400°C, with a vapour

pressure of 1 Pa at 428°C. Due to its volatility, when silica and magnesium are placed in a sealed reactor without being in contact with each other, the magnesium vapour, is able to migrate towards the silica and chemically reduce it, forming MgO and porous Si[43]. After the heating stage, the mixture is allowed to cool naturally, then removed from the furnace and etched in 1M HCl in order to remove the MgO by-product and unreacted Mg by dissolution. What remains is a powder, which is separated by filtration and dried. This powder contains silicon and silica, and separating the two requires the use of HF to dissolve the latter. This step is the most hazardous and unsustainable part of the whole process and elucidates the need to achieve high yields of silicon especially in the context of process economics and scalability. Increasing the ratio of Mg to SiO_2 used favours a parasitic side reaction which generates the undesired by-product magnesium silicide (Mg_2Si)[44], however this can be converted into silicon through an additional oxidation step. A silicide oxidation route takes advantage of this reaction route, producing Mg_2Si at 500°C then oxidising at 600°C to produce mesoporous silicon with a yield of 90%[39]. This method is not economical as the amount of Mg required is in large excess. The impact of Mg on the cost of production will be discussed further in Chapter 6.

2.3.2. Thermal control

Although silicon does not completely melt at the low temperatures of the MgTR reaction, sintering still occurs due to its exothermic nature[45]. This is undesirable as sintering also leads to pore collapse in the silicon product. Thermal control needs to be implemented in this process, in order to produce silicon with favourable pore properties and limit the amount of sintering which occurs during the reaction. To do this, the effects of certain basic parameters such as furnace temperature and ramp rate on the pore properties and yield of the silicon product need to be understood.

As the maximum furnace temperature used for the reduction increases, sintering is promoted, resulting in larger average pore diameters, loss of pore volume and a decrease in the specific surface area (SSA). This was shown in a study where bio-inspired silica was mixed with a stoichiometric amount of Mg and reduced at temperatures between 550 and 850°C [42]. The reduction carried out at 550°C resulted in a product with an average pore diameter of 4 nm and a SSA of 402 $m^2 g^{-1}$, however

when carried out at 850°C, the product had an average pore diameter of 34 nm, and a SSA of 110 m^2 g^{-1}. It was shown that in contrast to the pore properties, the yield of silicon is favoured at higher temperatures, whereby at 550°C the wt% yield of silicon by weight, measured by oxidation methods, was 29 wt%, increasing to 87 wt% for a reduction carried out at 850°C. At temperatures between 750 and 950°C, higher temperatures have been shown to decrease the formation of Mg_2Si [46]. This intermediate product reacts with SiO_2 to form Si and MgO, and the kinetics of this reaction is favoured at higher temperatures, hence, improving the yield of Si. From an economic perspective an improvement in the yield is beneficial however such high temperatures make this process highly unsustainable, so in selecting the correct temperature, one aspect (economics or environmental impact) will be favoured at the cost of the other.

With regards to the rate of increase in furnace temperature, higher ramp rates add large amounts of heat to an already hot reaction mixture. This leads to excessive heat build-up which can melt the silicon and encapsulate the MgO by-product, making it difficult to be removed from the acid etching step. In one study, it was reported that when a ramp rate of 5°C/min was used, the resulting mesoporous silicon had a SSA of 240 m^2 g^{-1} whereas when the rate was increased to 40°C/min, macroporous silicon was produced with a SSA of 54 m^2 g^{-1} [36]. In short, to limit sintering of the porous silicon product, it is important to avoid excess heat build-up in the mixture, so lower furnace temperatures and ramp rates should be used for the MgTR reaction. If a higher yield is desired then the furnace temperature should be increased at low ramp rates.

In addition to controlling the basic parameters, the protocol for the MgTR process can be modified to add another layer of thermal control. Various methods for dampening the large amount of heat released by the reduction have been successfully employed to produce porous silicon with improved structure and pore properties. Salts can be used as heat sinks which absorb excess heat either as sensible heat or latent heat (melting), thereby limiting sintering. It was first demonstrated by Luo *et al.* that when NaCl was added to a reduction mixture the resulting silicon had inherited the morphology of the feedstock silica with superior pore properties[47]. A mixture with NaCl produced silicon with a SSA of 295.5 m^2 g^{-1} at 650°C with a dwell time of 2.5 hours whereas a mixture without NaCl under the

same conditions produced non-porous silicon with a SSA of 5 m^2 g^{-1}. In a systematic study of various heat sink salts, it was shown that salts with higher heat capacities serve as better thermal moderators for the purpose of producing porous silicon[48]. In this study, when silica was reduced in the presence of calcium chloride at 650°C, the SSA of the silicon produced was highest (465 m^2 g^{-1}) compared to when other salts were used. Through Scherrer analysis it was found that the crystallite size of this silicon sample was the smallest (9.4 nm), indicating that the available heat for crystal growth was the lowest. The particle size of the magnesium powder was shown to have an effect on the thermal characteristics of the reduction reaction[49]. When larger particles of magnesium were used, the rate of reaction proceeded at a slower rate, hence the exothermic release of heat from the reaction is limited. Silicon formed from reduction by larger magnesium particles (4 mm) had pore diameters centred around 10 nm, with a SSA of 228.3 m^2 g^{-1} and when smaller particles (4 μm) were used, the silicon consisted of macropores centred around 80 nm, with a SSA of 56.8 m^2 g^{-1}. Thermal moderation can also be achieved by varying the temperature of the furnace during reduction. Martell *et al*. demonstrated that once activated, the MgTR reaction produces enough heat so that further reactions can continue with minimal addition of heat[50]. When the reaction mixture was firstly heated to 650°C for 30 minutes then cooled to 300°C for the remainder of the duration, excessive sintering was not seen in the sample, resulting in porous silicon with a surface area of 542 m^2 g^{-1}.

One reported method for producing porous silicon via MgTR below 650°C requires the use of a eutectic mixture of magnesium and aluminium[51]. It was shown that because the eutectic mixture could melt at 450°C the reduction of SiO_2 could proceed at this temperature. As a result the spherical structure of the Stöber silica used in the study was preserved during the reduction and inherited by the silicon product proving to be an effective method of reducing silica at low temperatures. The drawback, however, is that in order to form a eutectic mixture from a physical mixture of magnesium and aluminium, both of the metals have to first be allowed to mix as a liquid, which requires heating to 660°C (the melting point of Al).

The methods that have thus been reported requires in one way or another that heat is supplied at 650°C. From scalability and sustainability point of views, being able to lower this temperature without

sacrificing yield would have positive implications to this process. A wide range of silica has been used as feedstocks in the MgTR to produce porous silicon with no systematic study. In order to minimise the cost of production, the cheapest, most abundant feedstock should be used, however choosing a cheaper feedstock over a more costly one should not involve a compromise to the quality or yield of the silicon. It is clear that a quantitative comparison of various types of silica is needed in order to determine how different properties affect the MgTR reaction and change the silicon product. From this, the most desirable properties, and therefore the type of silica possessing these properties can be identified.

2.3.3. Techno-economic analysis of the MgTR

An economic analysis of the MgTR process is not available in the literature. It would, however, be crucial in determining the scalability using experimental results. In the interest of transferring research output to the industrial setting, the overarching objective of this project is to study the key parameters which govern the MgTR process by use the results to make technical improvements in favour of economic feasibility. This study is common in a design process, whereby an economic analysis is carried out on chosen designs to create a basis for optimisation[52].

In terms of functional material produced, both quality and quantity matter – assuming a fixed yield of silicon, large amounts (quantity) of non-porous (quality) silicon will not be equal to the same amount of porous silicon. Since the application of this silicon is in energy storage it would be meaningful to calculate the cost of manufacture in terms of $/kg of silicon. From this, the cost of energy stored, in terms of $/mAh can be calculated by taking into consideration the amount of energy each kg of silicon can store, kg/mAh. The MgTR modelled as a scaled-up process will have to be evaluated based on the cost of making silicon and this will have to be compared with its current market value[53].

Although the literature specifically on the economics and scale-up of the MgTR process is lacking, the process can be split into common processes such as, mixing, heating, cooling and drying. In this way, the MgTR process can be modelled from fundamentals as a powder handling process[54]. There are existing industrial processes which are analogous to the MgTR, such as silicothermic reduction

process (Pidgeon process)[55,56]. In this process, Mg is produced from magnesium oxide, using silicon as the reductant. This process was invented in the 1940s and modern variations of this process have been developed, which are the Magnetherm[57] and Mintek[58]. These processes are well studied, so where appropriate, data from these processes will be combined with fundamental design principles when building the model of the MgTR for the techno-economic analysis part of this project.

2.4. Silica types, properties and preparation

Silica is abundant in the earth's crust, mainly in the form of crystalline silicates such as quartz, cristobalite and tridymite[28]. The chemical composition and crystal structures vary, depending on the geological source of silicate. There are different requirements for processing quartz to make suitable for different applications, with the overall aim of separating out impurities. The raw material is washed with water, crushed, then friction washed to remove any strongly adhering impurities. The quartz is then screened/sized, then treated with various acids depending on the grade required to remove any impurities incorporated into its crystal structure. Further purification can be achieved by treating the quartz with Cl_2 at high temperatures (1200°C). This process is called hot chlorination in which mineral impurities are drawn to the surface of the quartz to form chloride salts which can then be removed. An additional step to remove any metal oxide contaminants is magnetic and electrostatic separation.

Purified quartz is then converted into various types of silica (Figure 2.9). The carbothermal reduction is carried out at high temperatures to produce metallurgical grade silicon and silicon carbide as a by-product. These products can be treated with chlorine gas to produce the volatile silicon tetrachloride, which is then burned in a hydrogen flame to produce fumed silica. These are made up primary particles between 5 and 40 nm, possessing SSAs around 300 m^2/g for the smallest particles and 50 m^2/g for the largest [59]. For the semiconductor industry, the metallurgical grade silicon is purified and zone refined before going through the Czochralski process, where monocrystalline silicon boules are grown.

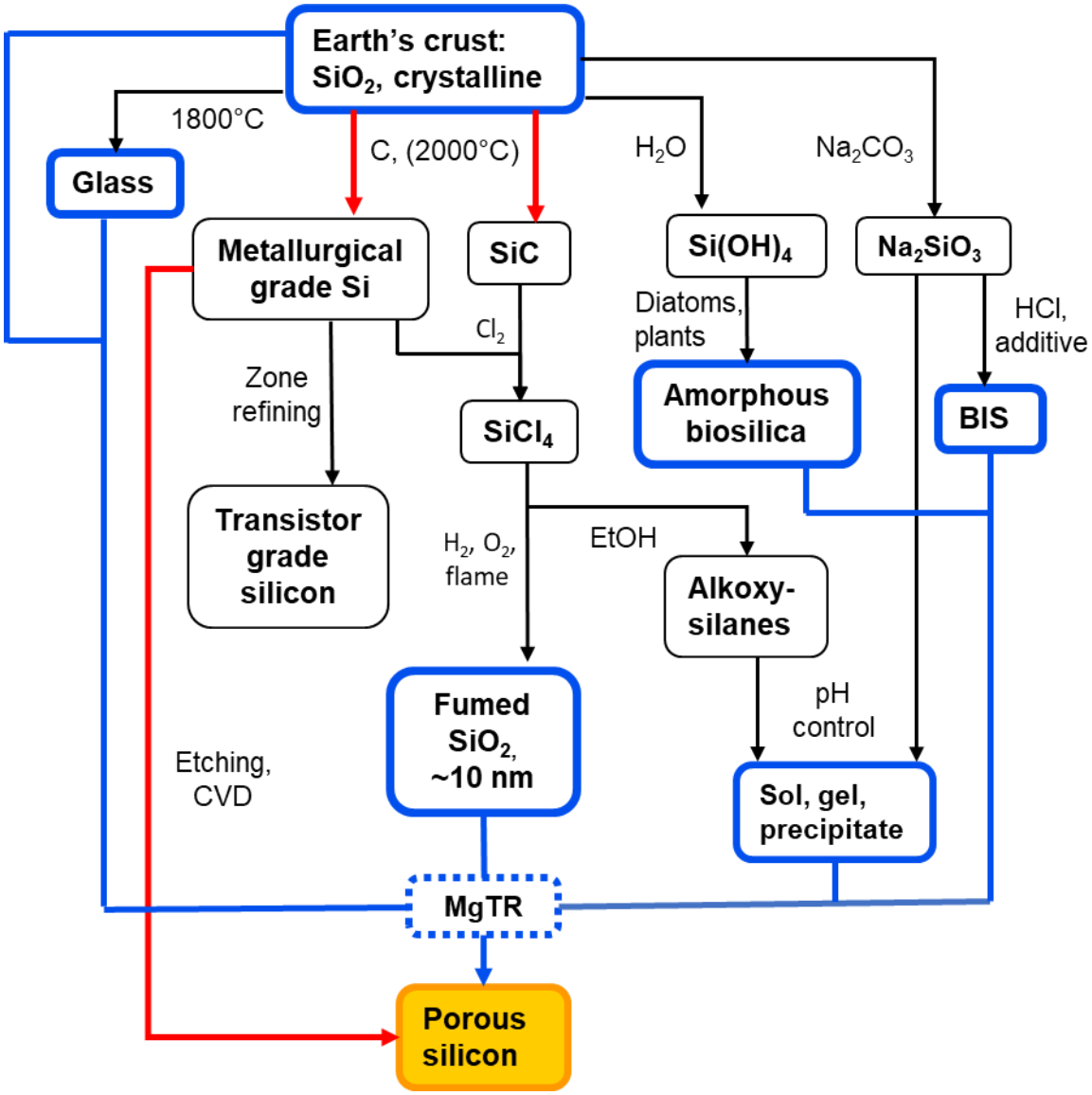

Figure 2.9: This schematic was constructed from information gathered from [65, 94, 95]. Red arrows show the current route taken to produce porous silicon, while blue arrows show the possible silica types that can be used to produce porous silicon via MgTR.

2.4.1. Silica sol, gel

Industrially, sodium silicate (Na_2SiO_3), formed by reacting silica quartz with sodium carbonate (Na_2CO_3), is the silica source used to form colloidal silica (silica sol). A sol is a liquid containing a stable suspension of silica particles which are small (<800 nm), and do not settle over time by gravity[60]. Na_2SiO_3 is dissolved in water to form silicic acid ($Si(OH)_4$), which undergoes a condensation-polymerisation reaction to form silica particles. At high pH (>9), the surfaces of silica particles in a sol are charged, repelling other particles and hence aggregation is suppressed[60]. Particles in this environment grow individually to a stable size according to the pH of the solution. Smaller silica particles are more soluble than larger ones at high pH, so in highly basic environments newly formed silica particles dissolve and re-deposit themselves onto larger particles. This process is called Ostwald ripening, and gives rise to larger particles at high pH. If colloidal silica is formed in acidic conditions (pH <7), the silica particles are uncharged, and so aggregate during growth. Unlike particles formed in basic conditions, these particles are not dispersed or uniformly sized, since growth and aggregation happens simultaneously. This results in the formation of a gel.

The IUPAC definition of a gel is a non-fluid polymer network that is expanded throughout its whole volume by a fluid[61]. Two interconnected phases exist within a gel - in a silica gel the polymer network is formed of $Si(OH)_4$ monomers and the fluid is usually water, an alcohol, or a gas such as air. The method of removal of the fluid from the gel affects the final structure of the gel. When there is water or alcohol trapped within the gel network, the gel is known as a hydrogel or alcogel. Removal of the trapped solvent by evaporation leads to the collapse of pores by capillary action. This network of silica with collapsed pores is called a xerogel. The structure of the pores can be preserved if the solvent is supercritically dried, resulting in an aerogel, resulting in greater specific surface areas.

Silicon tetrachloride can be reacted with alcohols to form alkoxysilanes such as tetraethyl orthosilicate (TEOS), which is used to make silica via solution synthesis[60]. TEOS dissolves in ethanol and is hydrolysed by water to form $Si(OH)_4$. In the presence of a basic catalyst, such as ammonium hydroxide a condensation-polymerisation reaction occurs to form non-porous spherical particles of silica. This method of making silica is called the Stöber method and results in uniformly sized particles

within the range of 10 nm and 800 nm[62]. Their uniformity and ease of synthesis at the gram scale is the reason why Stöber particles have been widely used in the MgTR process[63,64]. Using SEM, it is easy to track changes in the spherical structure under different conditions (temperature, ramp rate, dwell time). Wu *et al*. have shown that the reduction of Stöber silica at 700°C produces p-Si capable of storing a capacity of 1100 mAh/g after 100 cycles [63]. This was due to the sintering of the silicon, creating an interconnected structure that was created as a result of etching away MgO and unreacted SiO_2. The SSA was not reported in this study. Wang *et al.* have shown that by addition of NaCl at the reduction stage, the excess heat can be absorbed, allowing the structure of the silica to be preserved during the reduction[64]. Even though this reduction was carried out at 700°C the p-Si formed inherited the spherical structure, rather than forming a sintered interconnected structure. The silicon possessed a SSA of 214 m^2/g and was able to store a capacity of 1500 mAh after 100 cycles.

Ordered structures of silica can be formed through a micelle templating method[65]. Quarternary alkyl-ammonium surfactants form a micellar template, around which silicates can condense to form silica. By changing the length of the alkyl chain, micelles of different sizes could be formed, in this way, the pore diameters can be uniformly controlled. The surfactants can be removed by calcination. This is the basis of the formation of MCM-41, which is an ordered porous silica. The ordered structure results in a high SSA of ≥1000 m^2/g, however, through the MgTR at 650°C, a lot of the surface area is lost, and the silicon product only possesses a SSA of ~150 m^2/g, as demonstrated in a study by Shivaraju *et al.*[66] In another study, MCM-41 was reduced at 800°C, achieving p-Si with a SSA of 370 m^2/g[67]. It is important to note that the discrepancy could be due to the difference in reduction conditions but also that the preparation of p-Si in the work described in[66] used HF, while the work in[67] did not.

Stöber silica is considered non-porous, as each spherical particle does not possess pores while in contrast MCM-41 is highly porous due to the ordered, hollow structure. Using Stöber and MCM-41 as opposite extremes for comparison, it is clear that porous Si can be formed from either porous or non-porous SiO_2 via the MgTR.

2.4.2. Precipitated silica

Metal silicates are soluble in water and can be used to form silica particles upon the addition of acid. Initially a sol is formed, however if the final pH of the sol is low, then a gel is formed. At higher pH, due to the presence of metal ions, the surface charge of the particles are neutralised, eliminating repulsive forces and so a precipitate is formed, where the silica particles aggregate to form individual clusters throughout the sol, which can be separated by centrifugation. In the industrial setting, formation of precipitated silica tends to be on the order of hours and requires temperatures of around 60-80°C [68].

2.4.3. Bioinspired silica

A promising new method of synthesising silica draws inspiration from nature. Diatoms assimilate silica in the form of a hard exoskeleton, and through the study of the biological processes occurring within this organism, silica can be synthetically made in the lab at room temperature and neutral pH with reaction times in the order of minutes using sodium silicate[69]. Silica made via this synthetic route is referred to as bioinspired silica. These “green” reaction conditions are made possible through the use of additives which catalyse and direct the formation of silica, increasing the rate of silica condensation and forming various morphologies mimicking biological organisms. The mild conditions (ambient temperature and pressure, neutral pH) required for the bioinspired synthesis allows enzymes and bacterial cells to be immobilised during the synthesis step without being denatured or destroyed, an advantage the method has over the traditional precipitated silica synthesis method. Although this method has many merits, the main caveat with the bioinspired synthesis route is the requirement of biological or synthetic additives to which a large proportion of the costs of scale up is attributed to[70]. Should this type of silica be chosen as a feedstock for the MgTR then large quantities would be required, and cheaper additives would need to be found.

2.4.4. Natural and waste sources of silica

While synthetic silicas are commonly used as feedstock for the MgTR, it is important to consider natural as well as waste sources because of their low cost. This would not only benefit the economics of the process but would also help maintain feedstock flexibility of the MgTR (further discussion in Chapter 6 of this thesis). It was shown that quartz sand could be reduced into p-Si, giving a stable capacity of 1500 mAh/g after 100 cycles. The quartz sand was non-porous however, the p-Si after etching in HCl and HF had a SSA of 323 m^2/g. Quartz has been shown to have a higher activation energy for the MgTR reaction than amorphous silicon due to its more stable crystalline structure[71]. While the successful reduction of sand into p-Si is promising, more work is needed in order to improve the conversion of this low-cost material into p-Si. Crushed glass bottles have been reduced to p-Si at 700°C by Li *et al*.[37], showing a high specific capacity of ~2500 mAh/g after 60 cycles. Rice husks have been reduced at 650°C, showing a high specific capacity of 1500 mAh/g after 300 cycles.

The use of the various forms of silica including low value, non-porous silica highlights the feedstock flexibility of the MgTR. High performance silicon can be made, capable of achieving capacities above 1000 mAh/g. With comparably lower temperature requirements the MgTR is a promising alternative to the carbothermal reduction (~650°C vs ~2000°C), however there are issues which need to be resolved in order for the process to be commercially viable. Firstly, the temperature requirement of ≥650°C still makes the process economically unfeasible (Chapter 6 of this thesis), however using a lower temperature is not straightforward as the yield decreases with temperature. Secondly, in the studies cited above, most, if not all of the work involve the use of HF to remove unreacted SiO_2. HF etching is highly hazardous and seriously impedes the scalability of any process. Therefore, it is important that while the temperature requirement is lowered, the yield is not hindered, so that the requirement of HF can be eliminated. To tackle these issues is the aim of the work presented in this thesis. It is also important that while improvements are being made to the process, the impact on the economics is evaluated.

2.5. Aims

The application for p-Si in lithium-ion batteries have been shown to be successful in the last two decades. To summarise, silicon forms an alloy with lithium and can achieve a maximum theoretical capacity of 3579 mAh/g when it undergoes this alloying reaction, however mechanical stresses associated the volumetric expansion of 280% causes rapid failure of the electrode. Multiple solutions have been successfully demonstrated to limit overcome this issue, and have been discussed in the literature review of this thesis:

1. Ordered silicon nanotubes grown on a substrate, improving conductivity and creating void space to allow for expansion
2. Elastic, self-healing binders capable of reversing mechanical fracture
3. Decreasing the size of Si to the nano regime, below the critical fracture size of 150 nm
4. Using amorphous Si as it expands isotropically, spreading mechanical stress over a larger area.

These solutions indicate that issues relating to the degradation of silicon anode have in principle been tackled however, other barriers still need to be removed so that the widespread use of Si in lithium-ion batteries can be realised.

Firstly, solution 1 above is difficult to implement at large scale because the fabrication of ordered nanotubes involves a surface technique, which is slow and costly. For silicon to be adopted in the market, not only does the performance need to be high, but a crucial factor that as to be accounted for is the economics. The material has to be cost-competitive, and a discussion of the techno-economics of the synthesis of Si is presented in Chapter 6 of this thesis. Solution 2 enables the use of larger (≥150 nm) silicon particles that are commercially available but fracture upon multiple charge-discharge cycles in a cell. This can be considered in future work whereby silicon with optimised morphologies can be mixed with elastic binders to help prevent mechanical fracture and further prolong lifetime. Solution 3 identifies a particle size limit below which fracture would not occur. The synthesis of silicon in bulk is a challenge, and surface techniques which are common and effective at the lab scale are not suitable for scale up. Therefore, this solution supports the need to for a bulk

process for manufacturing nano-sized silicon. Solution 4, like solution 1, and in some respects, solution 3, is also challenging to implement at large scales, due to the surface nature of their synthesis procedures.

The work in this thesis takes a process-level approach, using commercially available silicas such as Syloid and fumed silica, and therefore has large focus on the economics of the process. Stöber silica, though not commercially available in bulk, is used for proof of concept, and further investigations into the transferability of the concept uses Syloid and fumed silica.

p-Si can be made in bulk via a few existing processes however, these processes have not been developed beyond lab-scale. The primary objective driving every large-scale chemical process is economics. If the choice of silica were to be based on economics alone, as long as the quality and the value of the product remains the same, the cheaper feedstock will be chosen over a more expensive one. The quality of p-Si is based on its yield and properties, which in turn, are based on the effect of the chosen conditions on the kinetics and thermodynamics of the reaction. The MgTR, as with all solid-state reactions, is diffusion limited due to lack of mobility of SiO_2. It is well known in solid-state reactions that by decreasing reactant particle size, mass-transfer limitations can be minimised [72]. Changing the rate of mass transfer will affect local concentrations of reactants which in turn will affect the rates of competing reactions. At present, little is known about the way in which particle size of silica affects the MgTR reaction. A wide range of silica sources of different particle sizes have been used in the MgTR process to produce Si however, a systematic study of how silica particle size affects the reaction does not exist. An understanding of the effect of particle size on the reaction would better inform researchers in the field on the selection of feedstock based on their properties, or how to change the conditions to achieve desirable properties in the product silicon. Once the silica particle size has been investigated, the next step would be to carry out an economic analysis on the MgTR so that the impact of hypothetical improvements to the process can be quantified by energy and cost savings. The aims of this thesis can therefore be summarised:

1. Determine the effect of silica particle size on the process conditions and the properties of the product.
2. Apply the understanding from Aim 1 to come up with a novel, economically efficient method for reducing commercial silica into p-Si with high electrochemical performance
3. Assess the economics of method found in Aim 2 and compare with the baseline method and identify ways to make improvements to the process in favour of economics.

As part of the first aim, the extent to which particle size of SiO_2 affects the temperature requirement of the process will be determined. This will be carried out using spherical, monodisperse, non-porous silica, described in Chapter 4. The concepts found in Chapter 4 will be applied to modify the process so that commercially available silica can be converted into porous silicon at temperatures below 650°C, achieving the second aim. This study is laid out in Chapter 5, where electrochemical performance of the silicon produced is presented. The economics of the baseline, and low temperature process will be evaluated in a techno-economic analysis (TEA) of the process laid out in Chapter 6. TEA is to quantify the different operating costs of the process and to identify the most expensive steps, which will guide future research. In the final section of this thesis, “Conclusion and outlook”, suggestion will be made on ways to further improve the economics of the process, beyond what is described in this thesis.

2.6. References

1 A. G. Morachevskii and A. I. Demidov, Russian Journal of Applied Chemistry, 2015, 88, 547–566.

2 M. T. McDowell, S. W. Lee, W. D. Nix and Y. Cui, Advanced Materials, 2013, 25, 4966–4985.

3 J. Li and J. R. Dahn, Journal of The Electrochemical Society, 2007, 154, A156.

4 M. N. Obrovac, L. Christensen, D. B. Le and J. R. Dahn, Journal of The Electrochemical Society, 2007, 154, A849.

5 L. Y. Beaulieu, K. W. Eberman, R. L. Turner, L. J. Krause and J. R. Dahna, Electrochemical and Solid-State Letters, 2001, 4, A137–A140.

6 R. A. Huggins and W. D. Nix, Ionics (Kiel), 2000, 6, 57–63.

7 M. T. McDowell, I. Ryu, S. W. Lee, C. Wang, W. D. Nix and Y. Cui, Advanced Materials, 2012, 24, 6034–6041.

8 X. H. Liu, J. W. Wang, S. Huang, F. Fan, X. Huang, Y. Liu, S. Krylyuk, J. Yoo, S. A. Dayeh, A. V. Davydov, S. X. Mao, S. T. Picraux, S. Zhang, J. Li, T. Zhu and J. Y. Huang, Nature Nanotechnology, 2012, 7, 749–756.

9 M. T. McDowell, S. W. Lee, J. T. Harris, B. A. Korgel, C. Wang, W. D. Nix and Y. Cui, Nano Letters, 2013, 13, 758–764.

10 M. N. Obrovac and L. Christensen, Electrochemical and Solid-State Letters, 2004, 7, A93.

11 X. H. Liu, L. Zhong, S. Huang, S. X. Mao, T. Zhu and J. Y. Huang, ACS Nano, 2012, 6, 1522–1531.

12 S. Ohara, J. Suzuki, K. Sekine and T. Takamura, Journal of Power Sources, 2004, 136, 303–306.

13 C. K. Chan, H. Peng, G. Liu, K. McIlwrath, X. F. Zhang, R. A. Huggins and Y. Cui, Nature Nanotechnology, 2008, 3, 31–35.

14 M. Green, E. Fielder, B. Scrosati, M. Wachtler and J. Serra Moreno, Electrochemical and Solid-State Letters, 2003, 6, A75–A79.

15 T. Song, J. Xia, J. H. Lee, D. H. Lee, M. S. Kwon, J. M. Choi, J. Wu, S. K. Doo, H. Chang, W. Il Park, D. S. Zang, H. Kim, Y. Huang, K. C. Hwang, J. A. Rogers and U. Paik, Nano Letters, 2010, 10, 1710–1716.

16 C. Wang, H. Wu, Z. Chen, M. T. Mcdowell, Y. Cui and Z. Bao, Nature Chemistry, 2013, 5, 1042–1048.

17 W. Wang and S. Yang, Journal of Alloys and Compounds, 2017, 695, 3249–3255.

18 J. Guo, A. Sun, X. Chen, C. Wang and A. Manivannan, Electrochimica Acta, 2011, 56, 3981–3987.

19 H. Wu, G. Chan, J. W. Choi, I. Ryu, Y. Yao, M. T. Mcdowell, S. W. Lee, A. Jackson, Y. Yang, L. Hu and Y. Cui, Nature Nanotechnology, 2012, 7, 310–315.

20 J. H. Lee, H. M. Lee and S. Ahn, in Journal of Power Sources, 2003, vol. 119–121, pp. 833–837.

21 C. Shen, M. Ge, L. Luo, X. Fang, Y. Liu, A. Zhang, J. Rong, C. Wang and C. Zhou, Scientific Reports, 2016, 6, 1–11.

22 J. R. Szczech and S. Jin, Energy and Environmental Science, 2011, 4, 56–72.

23 C. H. Yim, F. M. Courtel and Y. Abu-Lebdeh, Journal of Materials Chemistry A, 2013, 1, 8234–8243.

24 H. Kim, M. Seo, M. H. Park and J. Cho, Angewandte Chemie - International Edition, 2010, 49, 2146–2149.

25 J. Song, S. Chen, M. Zhou, T. Xu, D. Lv, M. L. Gordin, T. Long, M. Melnyk and D. Wang, Journal of Materials Chemistry A, 2014, 2, 1257–1262.

26 S. M. Lu, Renewable and Sustainable Energy Reviews, 2016, 59, 1–12.

27 M. Javidani and D. Larouche, International Materials Reviews, 2014, 59, 132–158.

28 N. N. Greenwood and A. Earnshaw, Chemistry of the Elements, Butterworth-Heinemann, Oxford, 2012.

29 N. V. Nemchinova, V. A. Bychinskii, S. S. Bel'skii and V. E. Klets, Russian Journal of Non-Ferrous Metals, 2008, 49, 269–276.

30 C. H. Lewis, H. C. Kelly, M. B. Giusto and S. Johnson, Journal of The Electrochemical Society, 1961, 108, 1114.

31 G. Fisher, M. R. Seacrist and R. W. Standley, in Proceedings of the IEEE, 2012, vol. 100, pp. 1454–1474.

32 M. J. Sailor, Porous Silicon in Practice: Preparation, Characterization and Applications, Wiley-VCH, Weinheim, Germany, 2012.

33 K. Urmann, E. Tenenbaum, J. G. Walter and E. Segal, Springer Series in Materials Science, 2015, 220, 93–116.

34 J. W. Choi and D. Aurbach, Nature Reviews Materials, 2016, 1, 1–16.

35 C. Yuan, Y. Deng, T. Li and F. Yang, CIRP Annals - Manufacturing Technology, 2017, 66, 53–56.

36 N. Liu, K. Huo, M. T. McDowell, J. Zhao and Y. Cui, Scientific Reports, 2013, 3, 1–7.

37 C. Li, C. Liu, W. Wang, Z. Mutlu, J. Bell, K. Ahmed, R. Ye, M. Ozkan and C. S. Ozkan, Scientific Reports, 2017, 7, 1–11.

38 M. Hasegawa, in Treatise on Process Metallurgy, 2013, vol. 1, pp. 507–516.

39 J. Liang, X. Li, Z. Hou, W. Zhang, Y. Zhu and Y. Qian, ACS Nano, 2016, 10, 2295–2304.

40 N. Birks, G. H. Meier and F. S. Pettit, Introduction to the High Temperature Oxidation of Metals, Second Edition, 2006, 9780521480420, 1–338.

41 D. Cho, M. Kim, J. Hwang, J. H. Park, Y. L. Joo and Y. Jeong, Nanoscale Research Letters, 2015, 10, 1–8.

42 J. E. Entwistle, G. Beaucage and S. v. Patwardhan, Journal of Materials Chemistry A, 2020, 8, 4938–4949.

43 Z. Bao, M. R. Weatherspoon, S. Shian, Y. Cai, P. D. Graham, S. M. Allan, G. Ahmad, M. B. Dickerson, B. C. Church, Z. Kang, H. W. Abernathy, C. J. Summers, M. Liu and K. H. Sandhage, Nature, 2007, 446, 172–175.

44 W. Chen, Z. Fan, A. Dhanabalan, C. Chen and C. Wang, Journal of The Electrochemical Society, 2011, 158, A1055.

45 J. Ryu, T. Bok, S. Kim and S. Park, ChemNanoMat, 2018, 4, 319–337.

46 K. K. Larbi, M. Barati and A. McLean, Canadian Metallurgical Quarterly, 2011, 50, 341–349.

47 W. Luo, X. Wang, C. Meyers, N. Wannenmacher, W. Sirisaksoontorn, M. M. Lerner and X. Ji, Scientific Reports, 2013, 3, 2222.

48 L. Khanna, Y. Lai and M. Dasog, Canadian Journal of Chemistry, 2018, 96, 965–968.

49 Z. Yang, Y. Du, G. Hou, Y. Ouyang, F. Ding and F. Yuan, Electrochimica Acta, 2020, 329, 135141.

50 S. A. Martell, Y. Lai, E. Traver, J. MacInnis, D. D. Richards, S. MacQuarrie and M. Dasog, ACS Applied Nano Materials, 2019, 2, 5713–5719.

51 Y. Lai, J. R. Thompson and M. Dasog, Chemistry - A European Journal, 2018, 24, 7913–7920.

52 R. K. Sinnott and G. Towler, Chemical Engineering Design, Elsevier Ltd, Oxford, Fifth Edit., 2009.

53 N. Lebedeva, F. Di Persio and L. Boon-Brett, Lithium ion battery value chain and related opportunities for Europe, 2016, vol. EUR 28534.

54 J. B. Butt, Chemical Engineering Science, 1960, 13, 93.

55 I. M. Morsi, K. A. El Barawy, M. B. Morsi and S. R. Abdel-Gawad, Canadian Metallurgical Quarterly, 2012, 41, 15–28.

56 S. N. Mathaudhu, A. A. Luo, N. R. Neelameggham, E. A. Nyberg and W. H. Sillekens, Essential Readings in Magnesium Technology, John Wiley & Sons Ltd, New Jersey, 2014.

57 C. Faure and J. Marchal, Jom, 1964, 16, 721–723.

58 M. Abdellatif, J South Afr Inst Min Metall, 2011, 111, 393–399.

59 O. W. Florke, H. A. Graetsch, F. Brunk, L. Benda, S. Paschen, H. E. Bergna, W. O. Roberts, W. A. Welsh, C. Libanati, M. Ettlinger, D. Kerner, M. Maier, W. Meon, R. Schmoll, H. Gies and D. Schiffmann, Ullmann's Encyclopedia of Industrial Chemistry, Wiley-VCH, Weinheim, Germany, 2012, vol. 32.

60 H.-P. Boehm, Angewandte Chemie, 1980, 92, 328–328.

61 J. Alemán, A. V. Chadwick, J. He, M. Hess, K. Horie, R. G. Jones, P. Kratochvíl, I. Meisel, I. Mita, G. Moad, S. Penczek and R. F. T. Stepto, Pure and Applied Chemistry, 2007, 79, 1801–1829.

62 W. Stöber, A. Fink and E. Bohn, Journal of Colloid And Interface Science, 1968, 26, 62–69.

63 H. Wu, N. Du, X. Shi and D. Yang, Journal of Power Sources, 2016, 331, 76–81.

64 W. Wang, Z. Favors, R. Ionescu, R. Ye, H. H. Bay, M. Ozkan and C. S. Ozkan, Sci Rep, 2015, 5, 1–6.

65 C. T. Kresge, M. E. Leonowicz, W. J. Roth, J. C. Vartuli and J. S. Beck, Nature 1992 359:6397, 1992, 359, 710–712.

66 G. C. Shivaraju, C. Sudakar and A. S. Prakash, Electrochimica Acta, 2019, 294, 357–364.

67 H. Sun, J. Chen, S. Liu, D. K. Agrawal, Y. Zhao, D. Wang and Z. Mao, International Journal of Hydrogen Energy, 2019, 44, 7216–7221.

68 S. V. Patwardhan, J. R. H. Manning and M. Chiacchia, Current Opinion in Green and Sustainable Chemistry, 2018, 12, 110–116.

69 S. V. Patwardhan, Chemical Communications, 2011, 47, 7567–7582.

70 C. Drummond, R. McCann and S. V. Patwardhan, Chemical Engineering Journal, 2014, 244, 483–492.

71 I. Gutman, L. Klinger, I. Gotman and M. Shapiro, Scripta Materialia, 2001, 45, 363–367.

72 S. E. Dann, Reactions and Characterization of Solids, Royal Society of Chemistry, Cambridge, 2000.

3. Materials and methods

3.1. Synthesis

3.1.1. Stöber synthesis

Silica nanospheres of various sizes were made via the Stöber method[1]. Ethanol (Absolute, VWR) and TEOS (Sigma-Aldrich, ≥99.0%) were added to volumetric flask and mixed with a Teflon coated magnetic stirring bar. After 10 minutes of mixing, de-ionised water was added, and following 10 more minutes of mixing, ammonium hydroxide solution (VWR, 29%) was added dropwise to the solution. The amounts of ethanol and ammonium hydroxide were varied to achieve the desired concentration of ammonium hydroxide. The solution was stirred for a further 24 hours at 20°C, followed by centrifugation at 5000 rpm for 15 minutes to separate the particles from the solution. The particles were rinsed with deionised water (to remove excess ethanol, ammonium hydroxide and TEOS, then centrifuged once more at 5000 rpm for 15 minutes, before being dried overnight at 80°C. Smaller particles (≤20 nm) were separated using a dialysis membrane with a 14 kDA molecular weight cut-off, immersed in a de-ionised water bath. The conductivity (inverse resistance) of the water bath was measured at 4-hourly intervals using a multimeter on 2 MΩ resistance setting, and when two consecutive readings were the same, the water in the bath was removed and replenished with fresh de-ionised water to introduce a new diffusion gradient. This was repeated several times until the conductivity was unchanging, then the particles within the dialysis membrane were separated by drying on an evaporating dish.

3.1.2. Bio-inspired silica synthesis

31.82 g of sodium metasilicate (Sigma Aldrich) was dissolved in 4650 mL of de-ionised water at 25°C in a 5L agitated Radley Reactor. 5.81 g of pentaethylene hexamine (PEHA) (Sigma Aldrich) was then added to the reactor and allowed to dissolve completely. At this point, the pH was recorded, and then continuously monitored. 350 mL of 1M HCl (Sigma Aldrich) was added to the reactor, then additional HCl was added using a micropipette to bring the solution down to pH 7±0.05 within 5 minutes. The

silica precipitate was then promptly filtered using a cellulose filter paper. The filter cake was rinsed multiple times with de-ionised water, then collected and dried in a drying oven at 80°C. The dried silica was crushed into a powder using a mortar and pestle then calcined in a furnace at 500°C for 5 hours to remove the PEHA.

3.1.3. Magnesiothermic reduction

The general procedure for carrying out the magnesiothermic reduction is described in this section. Modifications made to the procedure are further described in relevant sections of this thesis. Silica powders were ground with magnesium powder in an agate mortar and pestle at various weight ratios then placed in a stainless steel or alumina crucible and covered with a loose lid (Figure 3.1). The crucible was placed in a tube furnace at room temperature, then the furnace was hermetically sealed. Argon gas flowing through the tube furnace was set to a flow rate of 125 mL/min throughout the time the sample remained in the furnace. The furnace was held at room temperature before heating to purge oxygen from within the furnace. Typically, 0.5 g of Mg (Alfa Aesar, 99.8%) would be grinded with 0.5 g of silica powder. This mixture has a molar excess of magnesium (2.5:1 mole ratio). The basic heat treatment programme included ramping the furnace temperature at a rate of 1°C/min to 650°C, then dwelling at this temperature for 6 hours. The furnace and its contents were allowed to cool naturally to room temperature, still under flowing argon. Once the crucible was removed from the furnace, the reaction mixture was then added to 1M aqueous HCl and stirred with a magnetic stirrer at 200 rpm, at room temperature for 24 hours to dissolve Mg, Mg_2Si and MgO. Following this, the solution was filtered using cellulose filter paper and a Büchner flask under an active vacuum to separate the undissolved solids – a mixture of Si and unreacted SiO_2. The wet cake was dried in a drying oven at 80°C, then stored in a vacuum oven at 120°C.

Figure 3.1: A) Magnesium and silica powders in an agate mortar. Stainless steel crucible containing B) magnesium and silica before heating, and C) after heat treatment. D) Sample in 1M HCl after heat treatment.

3.2. Analytical techniques

3.2.1. Scanning electron microscopy (SEM)

3.2.1.1. Theory

Scanning electron microscopy (SEM) is used to gain information about the physical structure of a material. SEM can achieve magnifications up to 100,000x, and provide a 3D topographical image of a sample due to its depth of focus. In an electron microscope, electrons are accelerated by an electron gun at a target sample at accelerating voltages between 5-50 keV. The electron beam is focused by passing through magnetic condenser lenses, before colliding with the sample. Upon collision, the electrons are scattered by the sample elastically or inelastically. In inelastic scattering, the sample absorbs most of the energy from the incident electron and emits a secondary electron, along with radiation. In elastic scattering, electrons retain most of its incident energy and its scattered trajectory is different from its initial trajectory, becoming back scattered electrons. The secondary and back-scattered electrons then hit a detector which consists of semiconductors. These semiconductors generate currents when excited by electrons, which are then converted into an image. The electron beams typically have a penetration depth of 1 μm, so this technique relies on the reflection of electrons from the surface, therefore information only of the surface of a sample can be obtained. This is in contrast to transmission electron microscopy, where electrons are transmitted through a sample, and

deeper morphological information can be obtained. Length scales around 20 nm can be distinguished using SEM. Figure 3.2 shows the working principle of a scanning electron microscope.

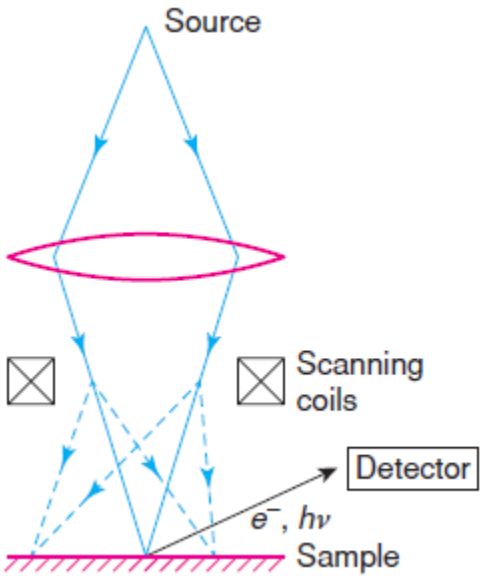

Figure 3.2: Diagrammatic representation of the working principle of a scanning electron microscope. Image source:[2].

3.2.1.2. Procedure

Dry powder samples are dispersed in absolute ethanol and sonicated for 10 minutes before being drop casted onto carbon coated aluminium stickers. Samples were coated in gold using a sputter coater. Scanning electron microscopy (SEM) images were taken at different magnifications using a FEI Inspect F scanning electron microscope with an accelerating voltage of 5 keV. Image J software was used for image analysis. SEM images of silica and reduced silica will be taken to determine its morphological structure, particle size, and degree of sintering. This will be particularly useful for Chapters 4 and 5 where the effect of particle size of silica on the conditions of the reduction reaction is investigated.

3.2.2. Transmission electron microscopy (TEM)

3.2.2.1. Theory

In transmission electron microscopy (TEM) an image is created by electrons which transmit through a sample, as oppose to reflecting off a sample. Similarly to SEM, a beam of electrons is focussed onto a target sample and scattered by the sample. Electrons which transmit through the sample are magnified through projector lenses and focussed onto a fluorescent screen. When electrons hit the fluorescent screen, light is generated creating an image of the sample. TEM provides morphological information about the sample bulk as opposed to just the surface. TEM can be used to resolve length scales smaller than the limits of SEM due to the higher accelerating voltage of the electrons. TEM is used to image particles too small to be resolved by SEM (≤20 nm), and to confirm the presence of internal porosity in reduced Stöber silicas in Chapter 4 and 5.

3.2.2.2. Procedure

Samples were dispersed in ethanol by ultrasonication then drop-casted onto 400 mesh copper TEM grids coated with lacey carbon films (Agar Scientific). TEM images were analysed using Image J software. All TEM images presented in this work were collected by Dr. Colm O'Regan using a Jeol R005 80-300kV transmission electron microscope.

3.2.3. Powder X-ray diffraction (XRD)

3.2.3.1. Theory

X-rays are a type of electromagnetic radiation with wavelengths on the order of 1-10 angstroms. X-rays are therefore able to interact with matter at the atomic scale, providing useful information on crystal structures and arrangements[3]. When electrons are rapidly decelerated by a magnetic field or by collision with a metal elcetrode, X-rays of varying wavelengths and intensities are produced. The wavelength of each photon of X-ray depends on the energy lost by the electron during deceleration to produce it. Since electrons can lose energy in either a single collision or multiple collisions, the X-rays produced form a continuous spectrum between short and long wavelengths. If the accelerating voltage exceeds a certain cut-off voltage whereby the electrons collide with the target material with enough energy to eject its K-shell electrons, a vacancy is created in the K-shell. An electron jumps from an outer shell to fill the vacancy in the inner K-shell, producing high intensity X-rays with characteristic wavelengths corresponding to the energy released from this jump. These characteristic wavelengths are specific to the target material. It is far more likely that an electron from an L-shell will jump to fill the K-shell vacancy, and the X-rays released from this jump are called the K_α radiation. A less probable event can occur where an outer M-shell electron will jump to the K-shell, and the produced X-rays with this characteristic wavelength are called K_β radiation. As a result, the intensity of K_α radiation is around 10 times higher than K_β radiation. The K_α peak is made up of doublet peaks, with the $K_{\alpha1}$ peak having an intensity twice that of the $K_{\alpha2}$ peak. The weighted average of the peaks is used since the wavelengths of the two are very close. For the purpose of X-ray diffraction, a monochromatic beam of X-rays is required, and the K_α peak is used since it is the most intense. A filter is used to absorb K_β radiation, so majority of the X-rays produced have wavelengths corresponding to K_α radiation, with very small amounts of K_β radiation. The resulting filtered beam of X-rays are then collimated and directed at a sample for X-ray diffraction.

An X-ray diffraction laboratory setup consists of an evacuated tube to which a large negative potential (~30kV) is applied, with respect to the anode. Electrons are accelerated from the cathode to the

anode. From equation [1], the higher the atomic number (Z), and the voltage (V), the greater the intensity of X-rays produced:

$$I = AiZV^m \qquad \text{Equation 1}$$

I is the total intensity of the X-rays produced, *A* is a proportionality constant, and *i* is the tube current. Hence, atomic number and voltage provides two of the criteria for choice of metal to use as an anode target in diffraction work.

X-rays are scattered when they collide with atoms in their path of propagation. When multiple rays propagating parallel to each other collide with a plane regularly spaced atoms in a crystal, the diffracted rays can interfere destructively or constructively depending on whether their relative phase. If they are in phase, or out of phase by whole integers of their wavelengths, they interfere constructively, and their amplitudes add. The criteria for constructive interference to occur is dependent on the spacing between the atoms in the crystal (d), the angle at which the rays collide with the plane atoms (θ), and the wavelength of the X-rays (λ), as given by the Bragg equation[4]

$$n\lambda = 2dsin(\theta)$$

n is an integer which is referred to as the order of reflection of the planes and gives the limitation that constructive interference can only occur between rays with path lengths differing by whole wavelengths. This is demonstrated in Figure 3.3, whereby the diffracted beams 1’ and 2’ are in phase due to the spacing between atoms P and Q being a whole wavelength apart.

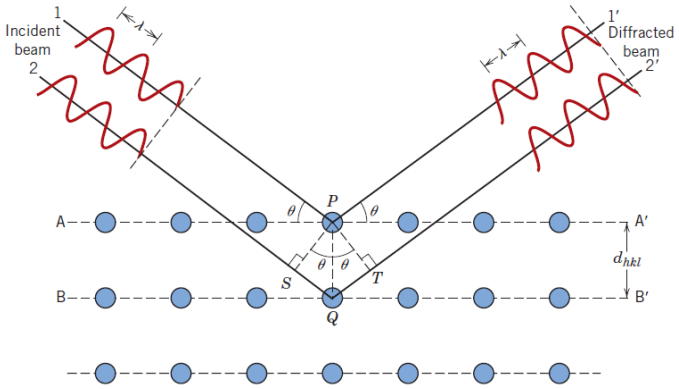

Figure 3.3: Schematic showing constructive interference between two rays 1' and 2', being diffracted from crystal planes spaced whole wavelengths apart. Image source:[5].

Given that crystal planes are spaced on the order of 3Å, and that sin(θ) has a magnitude no greater than 1, λ cannot be greater than 6Å, which sets another criterion for the choice of anode target for diffraction work. K_α radiation cannot be greater than 6Å, or too small (<1Å), which makes diffraction angles difficult to measure. A few common transition metals, chromium, cobalt, molybdenum, and silver are therefore used in laboratory diffractometers with the most commonly used being copper, with a $K_{\alpha 1}$ wavelength of 1.5406 Å. Using X-ray diffraction (XRD), information about a crystalline sample's d-spacing can be obtained, which can be used to identify or confirm the presence of the material.

3.2.3.2. Procedure

The work reported in this thesis was centred upon synthesising crystalline silicon (c-Si), hence XRD was be used to confirm the presence of c-Si in heat treated and acid etched samples. This was done by matching peaks obtained from XRD to peaks from a known standard of c-Si. The specific technique used was powder X-ray diffraction (pXRD). After being dried in a vacuum oven at 80°C for at least 24 hours, samples were ground into a fine powder using an agate mortar and pestle. PXRD was performed using the Stoe Stadi P (CuIP) diffractometer. 5 diffractograms were collected for each sample within the 2θ range of 1 and 120°, each taking 6 minutes. The diffractograms were combined using the WinXPow software to produce a single, averaged diffractogram for each sample.

3.2.4. Thermal gravimetric analysis (TGA)

3.2.4.1. Theory

The weight of a sample changes when heated, due to various processes such as moisture loss, decomposition or oxidation. Thermal gravimetric analysis (TGA) is a technique used to measure this change in weight as a function of temperature and time. A sample of known mass is placed in a crucible, with a perforated lid to allow movement of vapour and gases. The change of mass of the sample is determined and recorded using a microbalance. The thermal gravimetric analyser contains a microbalance, onto which the crucible is placed. The analyser heats the sample according to a pre-programmed heating profile and records the mass at set time intervals. An inert or oxidising atmosphere can be used. The change in mass can then be used to determine various properties of the sample. If a metal powder is heated under an oxidising atmosphere, the mass of the sample will increase as it oxidises. The total mass gained at the end of the heating profile can be used to determine the purity of the original metal powder, and it is this principle that will be used for the measurement of yield in this work.

3.2.4.2. Procedure

Samples were first dried in a vacuum oven at 120°C for at least 24 hours before placing thermal gravimetric analysis. Automated TGA was performed using a Perkin Elmer TGA 4000. Manual TGA was also performed, and the results were compared with automatic TGA to confirm the validity of the manual method. The manual method is as follows. A clean crucible with a perforated lid was weighed on a microbalance. A small amount (5-10 mg) of sample to be analysed was placed in the crucible. The crucible, now filled with the sample was weighed in order to determine the mass of the sample. The crucible was then placed in a furnace which heats the sample according to a programmed heating profile. The temperature was ramped up to 1000°C at a rate of 10°C/min. The sample was held at this temperature for 16 hours to ensure complete oxidation of the elemental Si present before being cooled naturally to room temperature. The crucible was then weighed using a microbalance and the

difference in mass before and after heating was calculated. The procedure described was the same for automated TGA, without the need of manually recording the sample.

TGA was performed on samples which were acid etched and dried at in a vacuum oven at 120°C for at least 24 hours. At this point, only silicon and silicon dioxide remained. TGA was used to determine the amount of Si as a percentage of the total moles of Si, elemental and oxidised in the sample. This was the yield of the sample, and was calculated from the mass change using the following equations

$$mass\ of\ O_2\ gained\ \ (g) = oxidised\ mass(g) - preoxidised\ mass(g)$$

$$moles\ of\ O_2\ gained\ = \frac{mass\ of\ O_2}{molar\ mass\ of\ O_2}$$

Given that Si reacts with O_2 at a 1:1 ratio, the number of moles of Si is equal to the moles of O_2 gained. From this the mass of elemental Si that was present in the sample before oxidation was calculated by:

$$mass\ of\ Si = moles\ of\ Si\ \times molar\ mass\ of\ Si$$

The mass of SiO_2 was then found by subtracting the mass of Si originally in the sample by the pre-oxidised mass. Dividing by the molar mass of SiO_2 gave the number of moles of SiO_2 in the pre-oxidised sample. Finally, the yield was calculated by:

$$yield\ (mol\%) = \frac{moles\ of\ Si \times 100}{moles\ of\ Si + moles\ of\ SiO_2}$$

3.2.5. Surface area and pore analysis

3.2.5.1. Theory

Surface area and pore size of a material is important as it relates to the material's performance in an application. The surface area of a material can be measured in a laboratory using the gas physisorption phenomenon. Gases can interact with a solid surface by adsorbing onto it through a condensation process. The amount of gas that is adsorbed onto a surface is a function of the pressure of the non-adsorbed (adsorbent) gas above the surface, and the exposed area of the surface. If the amount of gas adsorbed is known, through accurate and sensitive pressure measurements, along with the cross-sectional area of each gas molecule, then the surface area can be calculated. This is the basis of vacuum volumetric measurements[6]. The major assumption here is that when gases adsorb onto a solid surface, the surface will be covered with only a monolayer of gas. In reality, multilayer adsorption will occur before completion of the first monolayer and therefore there is no pressure or pressure range whereby only a single complete monolayer exists.

High energy (adsorption potential) sites on a solid surface will exist in many materials, such as within micropores (<2 nm) and adsorption will preferentially occur at these sites. As the inner walls of mesopores achieve monolayer coverage, the empty, unfilled space in the pore is now narrower, and becomes a high energy site, so adsorbents will also preferentially adsorb at these sites over open, flat sites. This behaviour of gases adsorbing onto solid surfaces gives rise to common isotherms which are defined by IUPAC[7] and shown in Figure 3.4 below.

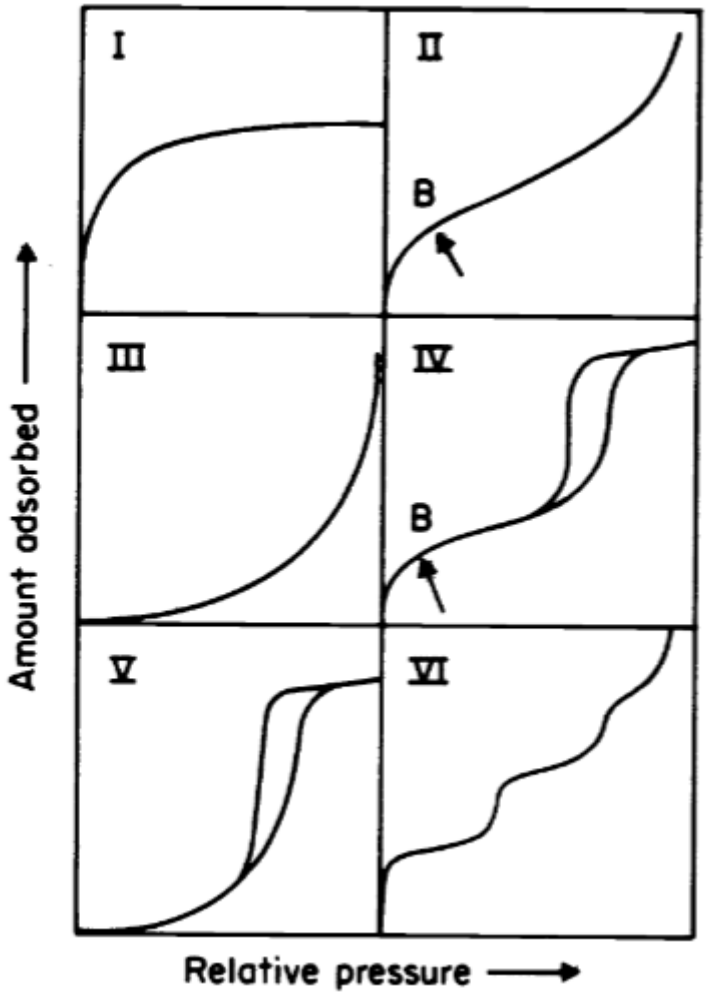

Figure 3.4: Characteristic adsorption isotherms assigned Types 1 – 4 by IUPAC. Image taken from:[7].

Type 1 isotherms indicate the presence of micropores and very little external surface areas. Micropores are filled first, hence a large amount of gas can be adsorbed at very low pressures. Once the micropores have been filled, the amount of gas that can be adsorbed is asymptotic at higher pressures due to limited external surface areas.

Type 2 isotherms indicate a non-porous or macroporous material. The point at which monolayer coverage is achieved is indicated by the inflexion at point B although it is accepted that multi-layer adsorption occurs before this.

Type 3 isotherms are characteristic of non-porous materials. Pore-filling does not occur, hence no inflexion point is seen in the isotherm.

Mesoporous materials exhibit Type 4 isotherms in gas adsorption measurements. At low relative pressures, Type 4 isotherms have the same trend as type 2 isotherms whereby the completion of a monolayer is indicated by a point of inflexion. However, at higher pressures, adsorbent molecules condense within the pores due to pore narrowing from the monolayer of gas. This is indicated by a sharp increase in amount of gas adsorbed. A hysteresis is seen on the desorption branch, and this is due to the difference in the pore filling and emptying behaviour (Figure 3.5)[6].

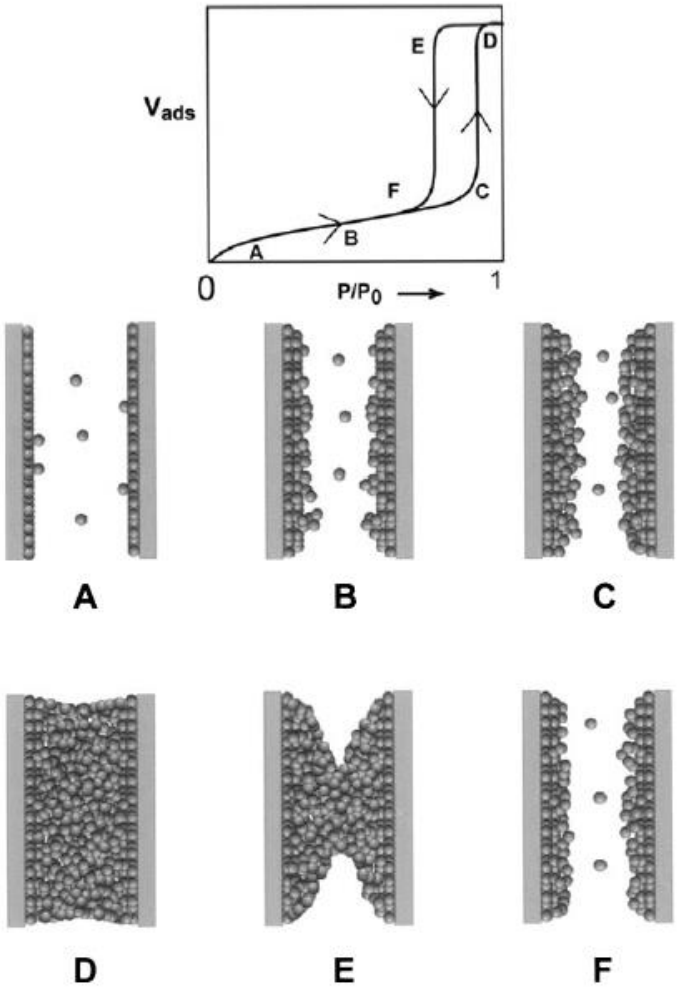

Figure 3.5: Mesopore filling and emptying during adsorption (A – C) and desorption (D – F) respectively, giving rise to isotherm hysteresis. Image source: [6].

Type 5 isotherms initially follow type 3 isotherms at low pressures, indicating weak interactions between adsorbent and adsorbate, and hence, lack of a pronounced inflexion point. At higher pressures, hysteresis is seen due to the pore condensation as described in Figure 3.5.

Type 6 isotherms are seen in uniform, spherical non-porous surfaces, where steps in the isotherm indicate multi-layer adsorption.

From the isotherms, information on the surface area can be gained using the relation between the amount of gas adsorbed at different partial pressures, originally described by Brunauer, Emmett and Teller (BET). The BET equation is as follows:

$$\frac{1}{W\left(\frac{P}{P_0}-1\right)} = \frac{1}{W_m C} + \frac{C-1}{W_m C}\left(\frac{P}{P_0}\right)$$

Where *C* is a factor which takes into account the energy of adsorption, the vibrational frequency of the adsorbate and a condensation coefficient. *W* is the weight of gas adsorbed, W_m the weight of gas adsorbed in the monolayer. *P* is the pressure at which the measurement is being taken, and P_0 is the saturation pressure, making P/P_0 the relative pressure.

Plotting the BET equation as a straight line allows for *C* and W_m to be determined from the slope and intercept respectively. Information about the pore size can be determined from gas adsorption measurements and using the Barrett-Joyner-Halenda method (BJH). The BJH method for pore analysis has its roots in the Modified Kelvin Equation:

$$\ln\left(\frac{P}{P_0}\right) = \frac{-2\gamma V}{rRT}$$

V represents the molar volume of the adsorbed liquid, γ the surface tension of the adsorbate, *r* the radius of the pore and *R* and *T* are the gas constant and temperatures respectively.

3.2.5.2. Procedure

Gas adsorption is carried out at the boiling point of the adsorbed gas. Nitrogen gas is accepted as the arbitrary adsorptive standard due to its small molecular cross-sectional area of 16.2 Å, which allows it to penetrate micropores, and wide availability of liquid nitrogen. Samples were in the form of a powder and are first dried in a degasser at 120°C under vacuum for a minimum of 24 hours. Gas adsorption was carried out using a Micromeritics Tristar 3000. The samples were then placed in a

sample tube which was immersed into a dewar containing liquid nitrogen. The programme was set to measure void space of the tube was measured using helium prior to adsorption measurements. Measurements were carried out between the P/P_0 range of 0.01 and 0.99.

3.2.6. Electrochemical testing

An electrochemical cell consists primarily of an anode, a cathode, electrolyte and a separator. Additionally, for a lithium-ion cell, a hermetically sealed casing is required to prevent exposure of cell contents to oxygen and moisture. Various cell architectures (cylindrical, prismatic, and pouch) are available for real world applications (Figure 3.6)[8].

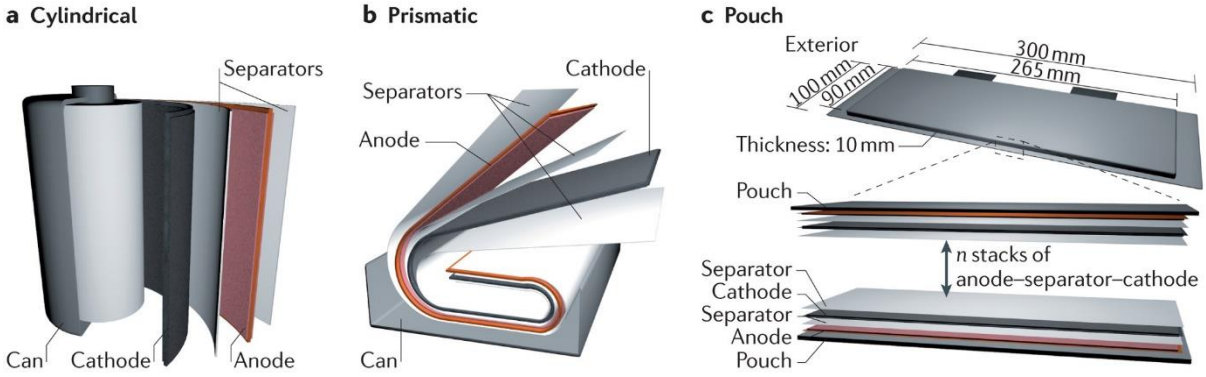

Figure 3.6: Cylindrical, prismatic and pouch cell architectures are designed for different real-world applications. These cells can be combined to form battery packs with higher voltage and current capabilities. Image source:[8]

These involve sophisticated assembly equipment and processes and require large amounts of active material (~10 – 100g) and electrolyte to achieve capacities that are suitable for their assigned application. For laboratory experiments, small amounts (~100 mg) of active material are synthesised and tested at a time, hence cylindrical, prismatic and pouch cells are not suitable for lab-scale material testing. Additionally, given that the performance of new materials synthesised in the lab can be unpredictable or fail completely, testing a large number of materials in these cell architectures is wasteful and costly. Instead, a more suitable architecture, the coin cell, is used. In this type of cell, less than 10 mg of active material is required for electrochemical testing. Coin cells are simple to assemble, and assembly can be done with a high success rate in a laboratory equipped for electrode

material research. The most common types of coin cells are 2016, and 2032, where the diameter of the cells are both 20mm, and the thicknesses of the cells are 1.6 or 3.2 mm respectively.

The components that make up a 2016 coin cell is shown in Figure 3.7. The coin cell consists of a stainless-steel (SS) casing, which, when crimped, acts as a sturdy and robust housing, preventing the movement of material in and out of the cell during electrochemical testing. For this work, copper foil was used as the current collector due to the voltage window (0.001 – 1.2V) within which materials were tested. The active material is coated on the copper foil, on the side facing the separator. Lithium foil is commonly used in laboratory cell testing, to provide an excess amount of lithium. Depending on the thickness of the electrode coating and the lithium foil, a SS spacer is used to ensure good physical contact between the electrodes and the casing.

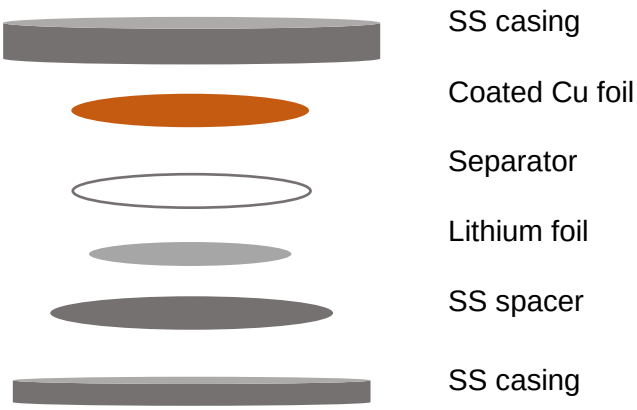

Figure 3.7: Schematic of a lithium-ion coin cell assembly.

3.2.6.1. Procedure

The electrode material synthesised in this work was in powder form. In order to make good contact with a current collector (copper foil), a water-based slurry was prepared, consisting of a binder and conductive carbon. To prepare the slurry, 0.05 g of CMC was first added to 2 mL of water in a PTFE container, then mixed in a Thinky ARE-250 mixer for 30 minutes to create a viscous, homogeneous mixture. Then, 0.05 g of C65 carbon was added to the mixture and mixed for a further 10 minutes. Finally, 0.15 g of synthesised silicon was added and mixed for a further 10 minutes. The slurry was

drop-casted onto a 10 μm thick copper foil using a doctor blade set to 300 μm. The coated foil was left to dry for 30 minutes under ambient conditions, then stored in a vacuum oven at 80°C overnight. 10 mm diameter electrodes were punched from the coated foil and each was weighed using a microbalance. The electrodes were then assembled into a coin cell in a glovebox as depicted in Figure 3.7 above, using a cell crimper. The separator used was Whatman GF/A glass fibre. The SS spacers were 5 mm thick, and the lithium foil was 9 mm in diameter and 38 μm thick.

Cells were put through an open circuit 'rest' step for 8 hours before constant current cycling. Galvanostatic cycling was performed on the cells between 0.01 and 1.2 V vs. Li at a C-rate of 0.1C for 100 charge and discharge cycles. The capacity was calculated based on the weight of active material, which was then used to set the current to match a C-rate of 0.1C.

3.3. References

1 W. Stöber, A. Fink and E. Bohn, *Journal of Colloid And Interface Science*, 1968, **26**, 62–69.

2 A. West, *WILEY*, 2014, 584.

3 B. D. Cullity, *Elements of X-ray DIffraction*, Addison-Wesley, 2nd Edition., 1957.

4 C. G. Pope, *J Chem Educ*, 1997, **74**, 129.

5 W. D. Callister and D. G. Rethwisch, *Fundamentals of Materials Science and Engineering: SI version*, John Wiley & Sons, 9th Edition., 2014.

6 S. Lowell, J. E. Shields, Martin. A. Thomas and M. Thommes, *Characterization of Porous Solids and Powders: Surface Area, Pore Size and Density*, Springer, 2004.

7 M. Thommes, K. Kaneko, A. v. Neimark, J. P. Olivier, F. Rodriguez-Reinoso, J. Rouquerol and K. S. W. Sing, *Pure and Applied Chemistry*, 2015, **87**, 1051–1069.

8 J. W. Choi and D. Aurbach, *Nature Reviews Materials*, 2016, **1**, 1–16.

4. Exploiting nanoscale effects enables ultra-low temperature to produce porous silicon

Royal Society of Chemistry Advances
Volume 11, Issue 56
October 2021
Doi: 10.1039/d1ra07212a

*Maximilian Yan and Siddharth V. Patwardhan**

Department of Chemical and Biological Engineering, Green Nanomaterials Research Group, The University of Sheffield, Mappin Street, Sheffield S1 3JD, UK. *s.patwardhan@sheffield.ac.uk

Received: 27th September 2021
Accepted: 21st October 2021
Published: 1st November 2021

4.1. Contribution

I performed the majority of the experimental work in this paper. TEM was performed by Dr. Colm O'Regan, of the Sorby Centre for Electron Microscopy. I also prepared the manuscript draft. SVP contributed to the project supervision, experimental design and editing of the manuscript.

Exploiting nanoscale effects enables ultra-low temperature to produce porous silicon

*Maximilian Yan and Siddharth V. Patwardhan**

Department of Chemical and Biological Engineering, Green Nanomaterials Research Group, The University of Sheffield, Mappin Street, Sheffield S1 3JD, UK. *s.patwardhan@sheffield.ac.uk

4.2. Graphical Abstract

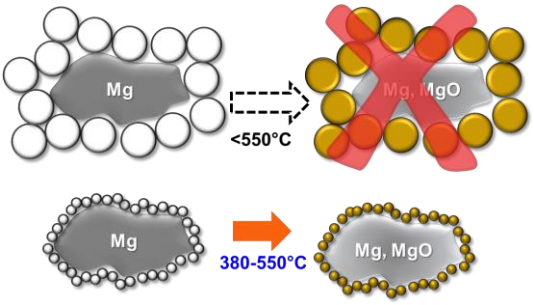

We show the first evidence of reduction of silica occurring at temperatures as low as 380°C to produce porous silicon without sacrificing the porosity and yield, thus paving the way for sustainable manufacturing.

4.3. Abstract

The magnesiothermic reduction (MgTR) of silica has been recently shown to produce porous silicon which can be used in applications such as photocatalysis and energy storage. MgTR typically requires ≥650°C to achieve meaningful conversions. However high temperatures are detrimental to the highly desired porosity of silicon, while also raising doubts over the sustainability of the process. In this work we show for the first time that the onset temperature of the MgTR is dependent on particle size of the feedstock silica. Using both in-house synthesised and commercial silica, we have shown that only particles ≤20 nm are able to trigger the reaction at temperature as low as 380°C, well below a cut-off temperature of 500°C, producing porous, crystalline silicon. The decrease in temperature requirement from ≥650°C to 380°C achieved with little modification to the overall process, without any additional

downstream processing, represents significant implications for sustainable and economical manufacturing of porous silicon.

Porous silicon is a material which is heavily studied due to its structural and electronic properties, which lends itself well to applications such as photocatalytic water splitting,[1] photoluminescence,[2] and energy storage.[3] However, for this material to become commercially accessible, a method of sustainably producing high quality silicon on a large scale is needed. It has recently been shown that the magnesiothermic reduction (MgTR) as a bulk method of producing porous silicon has a great potential for scaling up, especially when compared to the carbothermal[4] and electrochemical etching methods.[5] The MgTR is a reaction in which powdered Mg, the reducing agent, is mixed with powdered silica and heated in a furnace under argon atmosphere. The reaction mixture is typically heated to 650°C, and proceeds as shown in Equation 1:

$$2Mg_{(s)} + SiO_{2(s)} \rightarrow 2MgO_{(s)} + Si_{(s)}, \qquad \Delta\mathrm{H} = -291.62\ \mathrm{kJ\ mol^{-1}}$$

The mixture, once removed from the furnace, is then immersed in HCl to remove any magnesium species. It was shown that higher reduction temperatures (≥650°C) favour reaction completion,[6] however higher temperatures are detrimental for the desired porosity caused by sintering of nanocrystals. Below 650°C, the yield begins to drop, until a cut-off temperature of 500°C is reached, below which the reaction cannot proceed. Eutectic mixtures containing magnesium and Al have been shown to trigger the MgTR as low as 450°C to produce a yield of silicon of 64 mol%.[7] The drawback is that to form the eutectic, the metals have to be heated to 660°C initially, which is the melting point of aluminium. Alternatively, a two-step reduction method has been demonstrated whereby the MgTR can progress at 300°C, however this method requires the reactants to be heated initially to 650°C to trigger the reaction.[8]

In addition to the need for carrying out MgTR at lower temperatures to maintain porosity, from scalability and sustainability perspectives, being able to lower the temperature requirement without sacrificing the porosity and most importantly, yield, would have positive implications to this process. Herein, for the first time, we demonstrate a method of achieving the MgTR reaction at low temperatures (<450°C) without the use of eutectics or prior need of heating to 650°C, to produce

porous silicon with yields comparable to silicon made at temperatures above 650°C. Through a systematic study, we demonstrate the importance and the effects of particle size of the silica feedstock on MgTR temperature.

It is well known that nanoparticles exhibit enhanced reactivity compared to their bulk counterparts due to an increase in surface energy from their high surface to volume ratio. It is thus possible to exploit this nanoscale effect by using silica nanoparticles in order to activate the MgTR reaction at low temperatures. However, the effects of silica particle sizes on MgTR have not been investigated yet. In this study, silica nanoparticles of sizes 500, 75 and 20 nm were synthesised using the Stöber method (see S.I.).[9] These samples, referred to as S500, S75 and S20 respectively, were characterised using electron microscopy and N_2 adsorption (Figure 1 and Table S1). As expected, the particles showed well-defined spherical morphology with a tight particle size distribution and they did not possess any internal porosity.

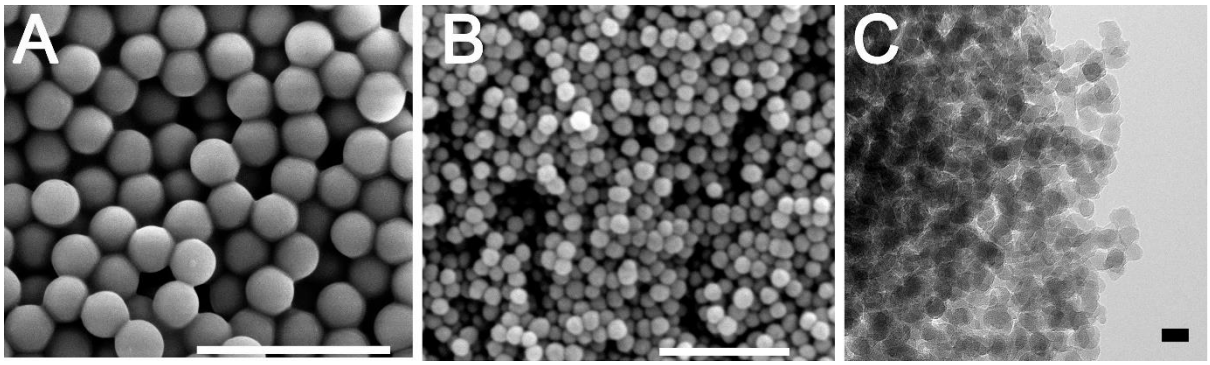

Figure 1: Electron microscopy images of A) S500, B) S75 and C) S20. Scale bars of A, B and C are 2 µm, 500 nm and 20 nm respectively.

The samples of silica were mixed with magnesium and reduced in a furnace at a range of temperatures between 450 and 750°C. The reduction products were then washed with acid to remove Mg-containing species before characterising with SEM to study the morphology and XRD to detect the presence of crystalline silicon. When 500 nm silica (S500) were used, the absence of diffraction peaks for MgTR performed at 450°C indicated that no crystalline product was formed at this temperature, consistent with the literature (Figure 2A). MgTR temperature ≥550°C was required to produce crystalline silicon as evident from peaks at 28, 47, 56, 68 and 76°, corresponding to 111, 220,

311, 400 and 331 crystal planes of Si, which matched the polycrystalline silicon standard. There were no peaks that correspond to MgO or unreacted Mg in any of the samples, thus confirming the effectiveness of the post-reaction acid washing.

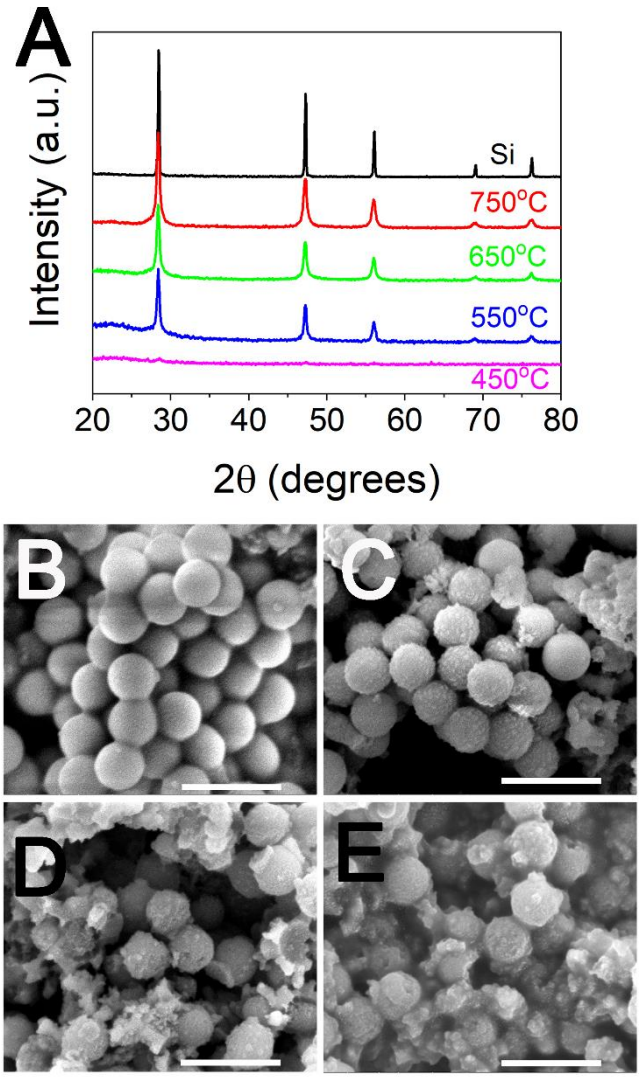

Figure 2: Diffraction patterns of products obtained from reducing S500 at different temperatures, along with a polycrystalline silicon standard (Si, NIST Standard 640d). SEM images of 500 nm silica particles reduced at B) 450°C, C) 550°C D) 650°C, and E) 750°C after washing in HCl are shown. Scale bars for SEM images are 1 µm.

The SEM images of S500 upon MgTR at 450°C showed a lack of any changes in the morphology, confirming that the particles have not undergone reduction. For temperatures of 550°C, specks on the surface of the silica particles can be observed in the SEM images (Figure 2B-D), which are consistent with the formation of silicon crystals reported in the literature.[10] At 650°C and 750°C the spherical morphology was less obvious due to breakage of silica particles from extensive reduction

and from the sintering of the newly formed crystalline silicon nanoparticles, again consistent with the literature.[10] These silicon samples were porous in nature, e.g. S500 reduced at 650^{o}C were mesoporous with some microporosity and had a specific surface area of 179 m^2/g (see Figure S2 and Table 2). MgTR using 75 nm silica particles (S75) followed a similar trend, where crystalline silicon was produced at all reduction temperatures except 450°C as shown in Figure S1.

In contrast to S500 and S75, when the 20 nm silica particles (S20) were used as the silica precursor for MgTR, crystalline silicon was produced at 450°C as verified by characteristic sharp peaks in the XRD shown in Figure 3A. The silicon produced had specific surface area of 184 m^2/g, similar to the silicon obtained from reducing S500 at 650^{o}C. The formation of crystalline silica was further confirmed by TEM analysis shown in Figure 3B. The Lattice planes are shown by arrows in Figure 3B to highlight the crystallites. In order to determine whether the larger silica samples had produced amorphous Si, we quantified the yields by oxidising the MgTR products and any associated change in weight was measured using thermal gravimetric analysis (TGA). This method allows for quantification of both crystalline and amorphous silicon present in the bulk sample and hence it is preferred over surface analysis using techniques such as XPS.[10]

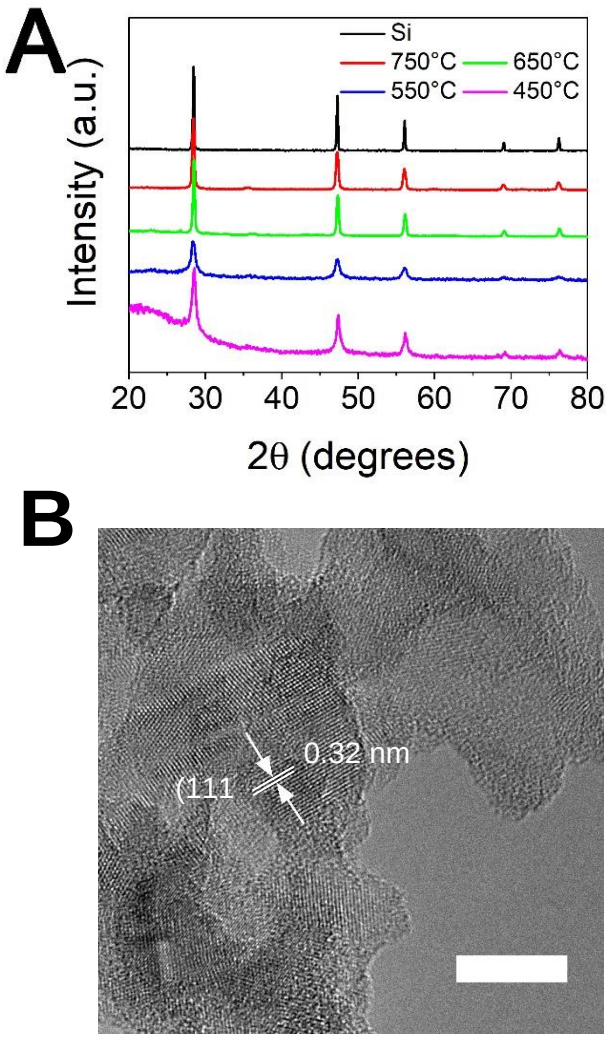

Figure 3: (A) Diffractograms of the reduction products of 20 nm silica particles. (B) TEM image of MgTR products obtained from S20 at 450°C (scale bar is 10 nm). Arrows indicate the crystallites formed.

When the MgTR was carried out at temperatures ≥550°C, the yields of silicon obtained from different particle sizes were similar irrespective of silica particle size (differences are within the measurement errors, see Figure 4A). However, prominent differences were seen at 450°C and below. 20 nm particles gave a yield of silicon of around 35 and 40 mol% for MgTR temperatures of 400°C and 450°C, while at the same MgTR temperatures (<550°C), S500 and S75 did not produced any detectable silicon. These results are in strong agreement with the results from XRD, where only 20 nm particles produced crystalline silicon at such low temperatures. Further lowering the MgTR temperature to 395°C resulted in no detectable amount of silicon for any of the silica particles used (data not shown). This is the first evidence of MgTR of silica occurring at temperatures as low as

400°C. These results also show for the first time that for MgTR reaction to occur at low temperatures, there is a particle size threshold: only the particles below this threshold will be able to initiate the MgTR reaction at sub-450°C temperatures.

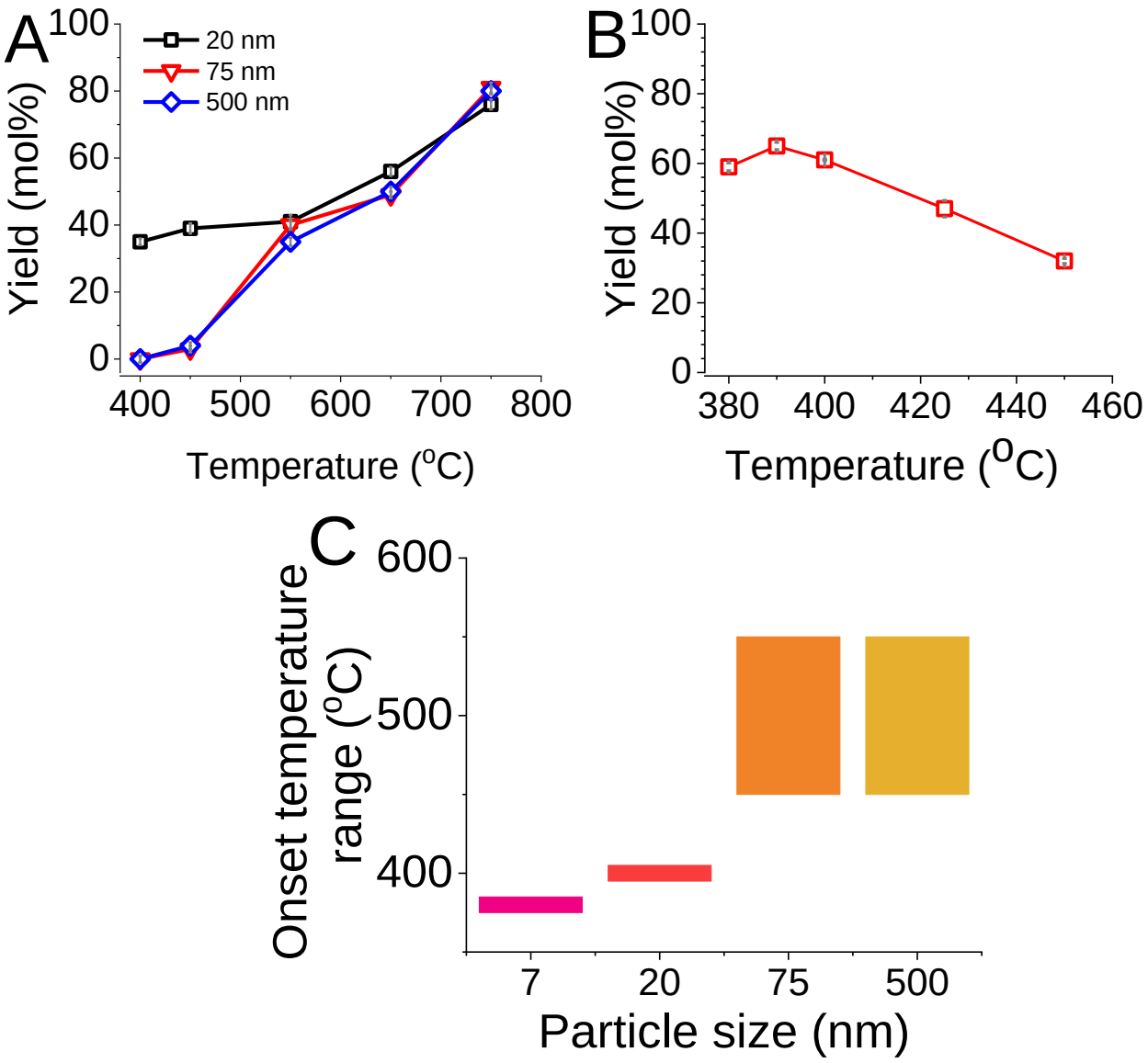

Figure 4: (A) The change in yield with MgTR temperature for different silica particle sizes. (B) Yields as a function of MgTR temperature for 7 nm silica. (C) Temperature brackets for the onset of MgTR with respect to the silica particle sizes.

This particle size threshold for lowering the activation temperature of MgTR is of particular interest. It is likely that using even smaller particles can lower the onset of MgTR further. In order to explore this possibility, 7 nm diameter fumed silica (purchased from Sigma, referred to as F7) was used to probe MgTR at low temperatures.[11] F7 was able to produce silicon at 450°C with a specific surface area of

177 m^2/g (again similar to that found for S500 at 650^{o}C). Interestingly, F7 produced silicon at temperatures as low as 380°C (Figure 4B) as confirmed with XRD (Figure S3). It is also worth noting that using this commercial silica further demonstrates that the activation of MgTR at lower temperatures exploiting the nanoscale effects is not limited to one type or source of silica particles. When MgTR was performed at 375°C, silicon formation was not detected (data not shown). It was also observed that the yield of silicon from F7 at its onset temperature of 380°C (~60 mol%) was far higher than the yield recorded from S20 at its respective onset temperature of 400°C (35 mol%). The yield of silicon from F7 declined from 390°C as the temperature was raised to 450°C (a decrease from 65 mol% to 32mol%). It is likely that side reactions which consume the freshly formed silicon (e.g. the formation of magnesium silicide) are favoured at different temperatures.

These results show that the temperature needed to activate the MgTR reaction is dependent on the particle size of the feedstock silica. The smaller the particles, the lower the onset temperature (Figure 4C). However, above a certain size (≥75 nm), the onset temperature did not reduce. We have therefore shown the first evidence of silica being converted to silicon via the MgTR reaction at a temperature as low as 380°C, using only magnesium as the reducing agent. It is well known that nanoparticles exhibit enhanced reactivity compared to their bulk counterparts arising.[12, 13] This well-known nanoscale effect is likely to reduce the activation barrier for initiating MgTR reaction, and hence the energy input required to initiate the reaction is lower.[14] This explains our findings where only the smaller silica nanoparticles (≤20 nm) react at temperatures ≤450°C.

In conclusion, we have shown for the first time that the particle size of the feedstock silica affects the temperature requirement of MgTR reaction due to the nanoscale phenomenon. The MgTR has an onset temperature which is dependent on particle size. Stöber particles ≥75 nm have a reduction onset temperature of ≥550°C. For particles ≤20 nm, the onset temperature decreases with particle size, where 20 nm particles were able to reduce at 400°C while 7 nm particles are able to reduce at 380°C. This study shows that it is possible to produce silicon at lower temperatures with minimal compromise to yield. Further studies are required to understand and manipulate the mechanisms of this low temperature process. The findings in this paper paves the way for the development of a

sustainable and scalable MgTR reaction strategy to produce porous silicon for photocatalysis, energy storage and other applications.

4.4. Experimental methods

4.4.1. Materials and reagents

Magnesium powder (99.98%) of -325 mesh grade and ethanol (absolute) were purchased from VWR. Ammonium hydroxide solution (28%), tetraethyl orthosilicate (TEOS 99.9%) and hydrochloric acid (HCl) were purchased from Sigma-Aldrich. Fumed silica was also purchased and used as received from Sigma-Aldrich.

4.4.2. Stöber silica synthesis

Silica nanospheres of various sizes were made via the Stöber methodMENDELEY CITATION PLACEHOLDER 0. Ethanol (Absolute, VWR) and TEOS (Sigma-Aldrich) were added to volumetric flask and mixed with a Teflon coated magnetic stirring bar. After 10 minutes of mixing, deionised water was added, and following 10 more minutes of mixing, 28% ammonium hydroxide solution was added dropwise to the solution. The amounts of ethanol and ammonium hydroxide were varied to achieve the desired concentration of ammonium hydroxide. The solution was stirred for a further 24 hours at 20°C, followed by centrifugation at 5000 rpm for 15 minutes to separate the particles from the solution. The particles were rinsed with deionised water to remove excess ethanol, ammonium hydroxide and TEOS, then centrifuged once more at 5000 rpm for 15 minutes, before being dried overnight at 80°C. Smaller particles (≤20 nm) were separated using a dialysis membrane with a 14 kDA molecular weight cut-off, immersed in a deionised water bath. The conductivity (inverse resistance) of the water bath was measured at 4-hour intervals using a multimeter on 2 MΩ resistance setting, and when two consecutive readings were the same, the water in the bath was removed and replenished with fresh de-ionised water to introduce a new diffusion gradient. This was repeated several times until the conductivity was unchanging, then the particles within the dialysis membrane were separated by drying on an evaporating dish.

4.4.3. Silicon synthesis

The preparation of the precursors for MgTR was according to our previously reported methodMENDELEY CITATION PLACEHOLDER 1 using magnesium powder (325 mesh, 99.8%, Alfa Aesar) and the synthesised Stöber silica nanospheres a weight ratio of 1:1, giving the stoichiometric mole ratio of 2.5:1. In every reduction, 0.5 g of magnesium and 0.5 g of silica were used. In mixed size silica precursors, the total mass of silica used in each reaction remained the same. A ramp rate of 1°C/min was used for all reductions. Samples were heated at maximum temperatures for a duration of 6 hours then cooled naturally to room temperature.

4.4.4. Analytical techniques

Scanning electron microscopy (SEM) images of the as synthesised and reduced Stöber particles were taken using FEI Inspect F electron microscope. Samples were prepared by dispersing dry silica powder in ethanol and drop casted onto carbon coated aluminium sheets, then gold coated using a sputter coater. **Transmission electron microscopy (TEM) imaging** was performed on a Jeol R005 80-300kV transmission electron microscope. Samples were dispersed in ethanol by ultrasonication then drop-casted onto 400 mesh copper TEM grids coated with lacey carbon films (Agar Scientific). TEM images were analysed using Image J software. **Powder X-ray diffraction (XRD)** technique was performed using the Stoe Stadi P (CuIP) diffractometer, with copper $K_{\alpha 1}$ radiation of wavelength 1.5406 Å. 5 diffractograms were collected for each sample within the 2θ range of 1 and 120°, each taking 6 minutes. The diffractograms were combined to reduce background noise, then analysed using WinXPow software. **Thermal gravimetric analysis** was performed using a Perkin Elmer TGA 4000, under continuous flow of oxygen. To ensure complete oxidation of the silicon present, samples were heated from 20ºC to 950ºC at a rate of 40ºC/min, holding at maximum temperature for 24 hours, before cooling at 40ºC/min to room temperature. **Surface area and pore size measurements** were performed using a Micromeritics Tristar 3000. Samples were degassed under vacuum at 120°C for 24 hours, then their weights were recorded. Warm and cold free space measurements were taken using He before and after immersing in liquid nitrogen, respectively. Adsorption and desorption

isotherms were then collected within the range of 0.001 and 0.999 P/P_0 using N_2 as the adsorbent whilst samples were immersed in a liquid nitrogen-filled dewar. Specific surface area was deduced from the isotherms by fitting with the BET model. Pore volumes and average pore diameters were deduced using the BJH model on the desorption branch.

4.5. Acknowledgements

The authors thank EPSRC for funding this research (EP/L016818/1, EP/P006892/1 and EP/R025983/1). Dr. Jake Entwistle (University of Sheffield) and Professor Marc Knecht (University of Miami) are thanked for helpful discussions.

4.6. References

1. I. S. Curtis, R. J. Wills and M. Dasog, *Nanoscale*, 2021, **13.4**, 2685-2692.
2. A. G. Cullis, L. T. Canham and P. D. J. Calcott, *Journal of Applied Physics*, 1997, **82**, 909-965.
3. M. N. Obrovac, L. Christensen, D. B. Le and J. R. Dahn, *Journal of The Electrochemical Society*, 2007.
4. N. V. Nemchinova, V. A. Bychinskii, S. S. Bel'skii and V. E. Klets, *Russian Journal of Non-Ferrous Metals*, 2008, **49**, 269-276.
5. Z. Bao, M. R. Weatherspoon, S. Shian, Y. Cai, P. D. Graham, S. M. Allan, G. Ahmad, M. B. Dickerson, B. C. Church, Z. Kang, H. W. Abernathy, C. J. Summers, M. Liu and K. H. Sandhage, *Nature*, 2007, **446**, 172-175.
6. J. E. Entwistle, G. Beaucage and S. V. Patwardhan, *Journal of Materials Chemistry A*, 2020, **8**, 4938-4949.
7. Y. Lai, J. R. Thompson and M. Dasog, *Chemistry - A European Journal*, 2018, **24**, 7913-7920.
8. S. A. Martell, Y. Lai, E. Traver, J. MacInnis, D. D. Richards, S. MacQuarrie and M. Dasog, *ACS Applied Nano Materials*, 2019, **2**, 5713-5719.
9. W. Stöber, A. Fink and E. Bohn, *Journal of Colloid And Interface Science*, 1968, **26**, 62-69.
10. J. Entwistle, A. Rennie and S. Patwardhan, *Journal of Materials Chemistry A*, 2018, **6**, 18344-18356.
11. These were fumed silica and it was used due to practical difficulties in obtaining meaningful qualities of <20 nm Stöber silicas.
12. Z. Y. Zhou, N. Tian, J. T. Li, I. Broadwell and S. G. Sun, *Chemical Society Reviews*, 2011, **40**, 4167-4185.
13. X. Li, H. Tang, X. Lu, S. Lin, L. Shi and Z. Huang, *Entropy*, 2015, **17**, 5437-5449.
14. Z. Y. Huang, X. X. Li, Z. J. Liu, L. M. He and X. C. Tan, *Journal of Nanomaterials*, 2015, **16**, 388-396.

5. Nanoscale triggering effect unlocks sustainable manufacturing of high-performance porous silicon anodes

*Maximilian Yan and Siddharth V. Patwardhan**

Department of Chemical and Biological Engineering, Green Nanomaterials Research Group, The University of Sheffield, Mappin Street, Sheffield S1 3JD, UK. *s.patwardhan@sheffield.ac.uk

5.1. Contributions

I performed all the reductions, XRD, TGA, gas adsorption experiments and collected all SEM images. I made all the electrodes, constructed the coin cells and performed all electrochemical testing. The TEM images were collected by Dr. Colm O'Regan. I prepared the initial manuscript, and Prof. Siddharth Patwardhan helped with the editing.

Nanoscale triggering effect unlocks sustainable manufacturing of high-performance porous silicon anodes

*Maximilian Yan and Siddharth V. Patwardhan**

Department of Chemical and Biological Engineering, Green Nanomaterials Research Group, The University of Sheffield, Mappin Street, Sheffield S1 3JD, UK. *s.patwardhan@sheffield.ac.uk

5.2. Abstract

Silicon has one of the highest specific capacities of all the potential lithium-ion battery anode materials, being able to store almost 10x more charge than the presently used graphite. Despite its huge volumetric expansion, extensive research in the field have shown that damage caused by this expansion can be limited or avoided by using porous silicon (p-Si). Producing p-Si in bulk can be achieved via the magnesiothermic reduction, however, it requires high temperatures (≥650ºC) to attain meaningful yields which. Performing MgTR at such temperatures causes loss of porosity due to sintering, while also requiring uneconomical amounts of energy. In this work we removed these limits and showed that silica of any particle size, including commercially available cheaper feedstock, can be triggered to react at as low as 380°C by adding a small amount of sub-20 nm silica. The optimum ratio of 25% sub-20 nm silica to 75% ≥20 nm silica achieved the highest yield of silicon of 83 mol%. We have shown that silicon made with a mixture of fumed silica and Syloid reduced at 380°C had the highest initial capacity of 1822 mAh/g, stabilising to 1000 mAh/g after 100 cycles. The electrochemical performance of all mixed silica exceeded that of unmixed silica reduced ≥650°C, strongly suggesting that this triggering strategy achieves high yields of high-performance p-Si anodes at ultra-low temperatures and therefore enables the economic bulk production of silicon. As such, this technique is suitable for any type of silica and does not require any additional pre- or post-processing steps[1]. Further, the principles of nanoscale-triggering are transferrable to a wide range of solid-state reactions[2].

5.3. Introduction

Energy storage is crucial in the modern society due to the need to lower carbon emissions and the widespread increase in electrification. Lithium-ion batteries is the storage method of choice, being used at various scales, from grid storage to electronic mobile devices, however lowering manufacturing costs and increasing energy densities will be required moving forward[3]. Silicon is one of the most promising materials being explored as an anode for lithium-ion batteries, with a theoretical capacity of 3579 mAh/g at room temperature[4]. When silicon is charged, it undergoes a 280% volumetric expansion to accommodate lithium, and in doing so, individual particles of silicon crack and exfoliate due to the mechanical stress associated with this expansion[5]. The exfoliated particles become electrically isolated and cannot participate in the redox reactions that store and release energy. This expansion is therefore detrimental to its structure and its ability to store lithium, resulting in a rapid decline in its capacity[6,7]. Introducing pores or void space within or around the active material minimises mechanical stress within the material structure. Based on this motive, silicon nanowires[8], mesoporous and various other structures[9] have been synthesised that boast improved cycle life.

The current method of producing metallurgical grade silicon involves the reduction of silica at 2000°C using coke as the reducing agent, known as the carbothermal process[10]. This method produces relatively pure silicon (>99%), however it operates well above the melting point of silicon and so is unsuitable for producing porous structures. Additionally, achieving such high temperatures is energy intensive and produces CO_2 as a by-product. Porous silicon used in sensing and optoelectronic applications is predominantly made via electrochemical etching of electronic grade silicon wafers[11,12]. This is a surface technique rather than a bulk, and requires HF as the etchant, therefore its scale-up to bulk manufacturing is uneconomical and unsustainable. One method of producing porous silicon that has a great potential for scaling up is the magnesiothermic reduction reaction (MgTR)[13,14]. Unlike electrochemical etching, this is a bulk method where silica powder is reduced with magnesium at elevated temperatures and in an inert atmosphere (Equation 1). MgTR is suitable for a wide range of silica sources including sand[15], rice husks[16] and even crushed glass.[17]

$$2Mg_{(s)} + SiO_{2(s)} \rightarrow 2MgO_{(s)} + Si_{(s)}, \qquad \Delta H = -291.62\ \mathrm{kJ\ mol^{-1}} \qquad (1)$$

Typically, the mixture is heated between 650°C-800°C in a furnace above the melting point of magnesium (650°C) for 1-6 hours under flowing argon. Porous silica precursors can be reduced in this manner to form porous silicon analogues, since the reaction temperature is far below the melting point of silicon (1414°C). Recently, from a systematic study of MgTR, we developed an understanding of the effects of processing conditions on the properties and performance of porous silicon produced[18]. We showed that regardless of the initial silica and its pore properties, new mesoporous structures of Si can be formed during the MgTR. That study also revealed that there is a tension between porosity and purity of silicon obtained from MgTR – high temperatures (>800°C) were required to achieve high purity (>90%), however, loss of mesoporosity was observed from sintering of product silicon at higher temperatures. The main reason behind this is the large amount of heat generated from the exothermic nature of MgTR ($\Delta H = -291.62\ \mathrm{kJ\ mol^{-1}}$), leading to localised hot-spots, which causes sintering and loss of porosity between silicon crystallites. As such, strategies are needed to obtain high purity silicon at low MgTR temperatures (<500°C) such that mesoporosity can be retained. This can also lead to lower overall energy requirements, thus improving the sustainability and economic viability of the MgTR. The methods that have thus been reported require that heat is supplied at 650°C. It has been widely reported in the literature that with a reaction temperature of ≤650°C, the yield of silicon from MgTR are generally very low [19].

Magnesium has a significant vapour pressure below its melting point[20], which can initiate the MgTR reaction[14], however it is slow and impractical at ≤650°C, thus heavily limiting the yield of silicon that can be achieved. Another way to decrease energy input is to lower the amount of heat supplied to the reaction mixture by controlling the temperature of the furnace during reduction. Martell *et al.* demonstrated that once activated at 650°C for 30 minutes, the MgTR reaction produces enough heat so that further reactions can continue at 300°C for 6 hours[21]. However, heating to 300°C for up to 6 hours is still a drawback in terms of economics and sustainability for large scale manufacturing.

The use of a eutectic mixture of magnesium and aluminium is yet another method for producing porous silicon via MgTR below 650°C[22]. A eutectic mixture of Mg and Al with a melting point of 450°C was used to reduce silica at this temperature producing silicon with a SSA of 132 m^2/g and a yield of 64%. The drawback, however, from an economic and sustainability perspective is that the process still requires heating to 650^{o}C (eutectic formation) and that an additional reagent is now required, which will require removal further downstream.

Lowering the reaction temperature without sacrificing the yield and porosity would have positive implications on the viability of MgTR as a commercial manufacturing method. To this end, the sustainability and economics (and hence the scalability) are particularly sensitive to two key factors – the feedstock silica price and the energy demand for the reduction reaction (which is related to the temperature needed to achieve high yields). While we recently reported that the MgTR temperature is dependent on silica particle size and that silicon can be produced at as low as 380-400°C using ≤20 nm diameter silica particles[23], this adds a new constraint on the particle sizes of silica that can be used. The synthesis of uniform and controlled nano-sized particles is costly and difficult to scale-up compared to their bulk counterparts. This constraint excludes the possibility of using cheap, abundant silica sources at low temperature simply because of the size requirement. Given the sensitivity of the economics on the feedstock price, achieving MgTR at temperatures below 500°C but without the need for costly feedstock is desirable, which is not reported yet.

In order to address this challenge, in this paper we investigate a method of triggering the MgTR reaction of silica powder (not nanoparticles) at low temperatures (<500°C) to produce porous silicon. Specifically, we exploit the nanoscale effects of silica nanoparticles on MgTR, designing a low temperature MgTR process that produces porous silicon with higher yields than silicon made using the conventional 650°C process. We show that the triggering effect is not limited to certain types of silica and can be leveraged to produce porous silicon with high yields from commercially available, bulk silica. Finally, we demonstrate that the silicon produced via the triggered low-temperature reduction method exhibits superior electrochemical performance compared to silicon produced at higher temperatures.

5.4. Experimental methods

5.4.1. Stöber silica synthesis

Silica nanospheres of various sizes were made via the Stöber method[24]. Ethanol (Absolute, VWR) and TEOS (Sigma-Aldrich) were added to a volumetric flask and mixed with a Teflon coated magnetic stirring bar. After 10 minutes of mixing, deionised water was added, and following 10 more minutes of mixing, 28% ammonium hydroxide solution was added dropwise to the solution. The amounts of ethanol and ammonium hydroxide were varied to achieve the desired concentration of ammonium hydroxide, resulting in either 20 nm or 500 nm particles (denoted as S20 and S500 respectively). The solution was stirred for a further 24 hours at 20°C, followed by centrifugation at 5000 rpm for 15 minutes to separate the particles from the solution. The particles were rinsed with deionised water to remove excess ethanol, ammonium hydroxide and TEOS, then centrifuged once more at 5000 rpm for 15 minutes, before being dried overnight at 80°C. Smaller particles (≤20 nm) were separated using a dialysis membrane with a 14 kDA molecular weight cut-off, immersed in a deionised water bath. The conductivity (inverse resistance) of the water bath was measured at 4-hour intervals using a multimeter on 2 MΩ resistance setting, and when two consecutive readings were the same, the water in the bath was removed and replenished with fresh de-ionised water to introduce a new diffusion gradient. This was repeated several times until the conductivity was unchanging, then the particles within the dialysis membrane were separated by drying on an evaporating dish.

5.4.2. Bio-inspired silica synthesis

Sodium metasilicate was dissolved in de-ionised water at 25°C in a 5L agitated Radley Reactor. Pentaethylene hexamine (PEHA) was then added to the reactor and allowed to dissolve completely. At this point, the pH was recorded. 1M HCl was added to the reactor to bring the solution down to pH 7 within 5 minutes. The silica was then promptly filtered using a cellulose filter paper. The filter cake was rinsed multiple times with de-ionised water, then collected and dried in a drying oven at 80°C. The dried silica was crushed into a powder using a mortar and pestle then calcined in a furnace at 500°C for 5 hours to remove the PEHA.

5.4.3. Silicon synthesis

The preparation of the precursors for MgTR was according to our previously reported method[18] using magnesium powder (325 mesh, 99.8%, Alfa Aesar) and silica with a weight ratio of 1:1, giving the stoichiometric mole ratio of 2.5:1. In every reduction, 0.5 g of magnesium and 0.5 g of silica were used. In mixed size silica precursors, the total mass of silica used in each reaction remained the same. Commercial silicas were used as obtained. Syloid AL-1 FP was kindly supplied by Grace Davison. Fumed silica was purchased from Sigma Aldrich. A ramp rate of 1°C/min was used for all reductions. Samples were heated at maximum temperatures for a duration of 6 hours then cooled naturally to room temperature. Reduced samples were added to 1M HCl (Sigma Aldrich) and stirred using a Teflon coated magnetic stirrer for 24 hours. The solution was then filtered using a 450 nm cellulose filter paper, washing with 100 mL de-ionised water to remove NaCl salts. The silicon/silica powder was then dried in a 120°C vacuum oven.

5.4.4. Analytical techniques

Scanning electron microscopy (SEM) images of the as synthesised and reduced samples were taken using FEI Inspect F electron microscope. Samples were prepared by dispersing dry powder in ethanol and drop casted onto carbon coated aluminium sheets, then gold coated using a sputter coater. **Transmission electron microscopy (TEM)** images were taken using a Jeol R005 80-300 kV transmission electron microscope. Images were analysed using Image J software. Samples were first dispersed in ethanol by ultrasonication then drop-casted onto 400 mesh copper TEM grids coated with lacey carbon films (Agar Scientific). **Powder X-ray diffraction (XRD)** technique was performed using the Stoe Stadi P (CuIP) diffractometer, with copper $K_{\alpha 1}$ radiation of wavelength 1.5406 Å. 5 diffractograms were collected for each sample within the 2θ range of 1 and 120°, each taking 6 minutes. The diffractograms were combined to reduce background noise, then analysed using WinXPow software. **Thermal gravimetric analysis** was performed using a Perkin Elmer TGA 4000, under continuous flow of oxygen. To ensure complete oxidation of the silicon present, samples were heated from 20ºC to 950ºC at a rate of 40ºC/min, holding at maximum temperature for 24 hours,

before cooling at 40ºC/min to room temperature. It is important to note that the yield experiments were carried out within 1 week of the drying step, as extensive surface oxidation occurs under ambient conditions which would affect the yield of silicon[25]. **Surface area and pore size measurements** were performed using a Micromeritics Tristar 3000. Samples were degassed under vacuum at 120°C for 24 hours, then their weights were recorded. Warm and cold free space measurements were taken using He before and after immersing in liquid nitrogen, respectively. Adsorption and desorption isotherms were then collected within the range of 0.001 and 0.999 P/P_0 using N_2 as the adsorbent whilst samples were immersed in a liquid nitrogen-filled dewar. Specific surface area was deduced from the isotherms by fitting with the BET model. Pore volumes and average pore diameters were deduced using the BJH model on the desorption branch. **Electrode fabrication** was performed by mixing reduced silica samples with carboxymethyl cellulose (CMC) binder and C65 conductive carbon in water before tape casted onto copper foil. The slurry was left to dry on the copper foil at ambient conditions, then 11 mm diameter electrodes were punched out. The electrodes were dried in a vacuum oven at 80°C overnight, then made into half-cells with lithium foil. The cells were constructed with 2016 type coin cell casing, stainless steel spacer and a glass fibre separator. A 1 M $LiPF_6$ in a 50:50 ethyl carbonate:dimethyl carbonate (EC:DMC) electrolyte was used, with 5% fluorethylene carbonate (FEC) additive. **Galvanostatic testing** was performed on a Maccor electrochemical test system, and cells were placed in a temperature-controlled chamber set to 25.00°C.

5.5. Results and discussion

It is well known that nanoparticles exhibit enhanced reactivity compared to their bulk counterparts due to an increase in surface energy from their high surface area to volume ratio. In previous work the effect of silica particle sizes on MgTR was investigated and it was found that the onset temperature for MgTR is dependent on feedstock silica particle size. Specifically, it was shown that particles ≤20 nm can be reduced at temperatures as low as 380ºC, thus demonstrating that the high surface energy of silica nanoparticles can be exploited.

5.5.1. Triggering the magnesiothermic reduction

The MgTR reaction is highly exothermic, and can produce enough heat to become self-sustaining. It is thus likely that once the reduction has begun, the large release of heat can be absorbed by the surrounding particles which, in turn, undergo reduction themselves. This implies that by mixing small particles that can be reduced at 400°C (≤20 nm) and large particles (>>20 nm), the reduction of the large particles could be triggered at low temperatures by small particles. In order to explore this possibility, silica particles of 20 nm (S20) and (S500), both were mixed together at different ratios, and reduced in the presence of Mg at 450°C. Note that S500 does not undergo any reduction at temperatures less than 500°C[23].

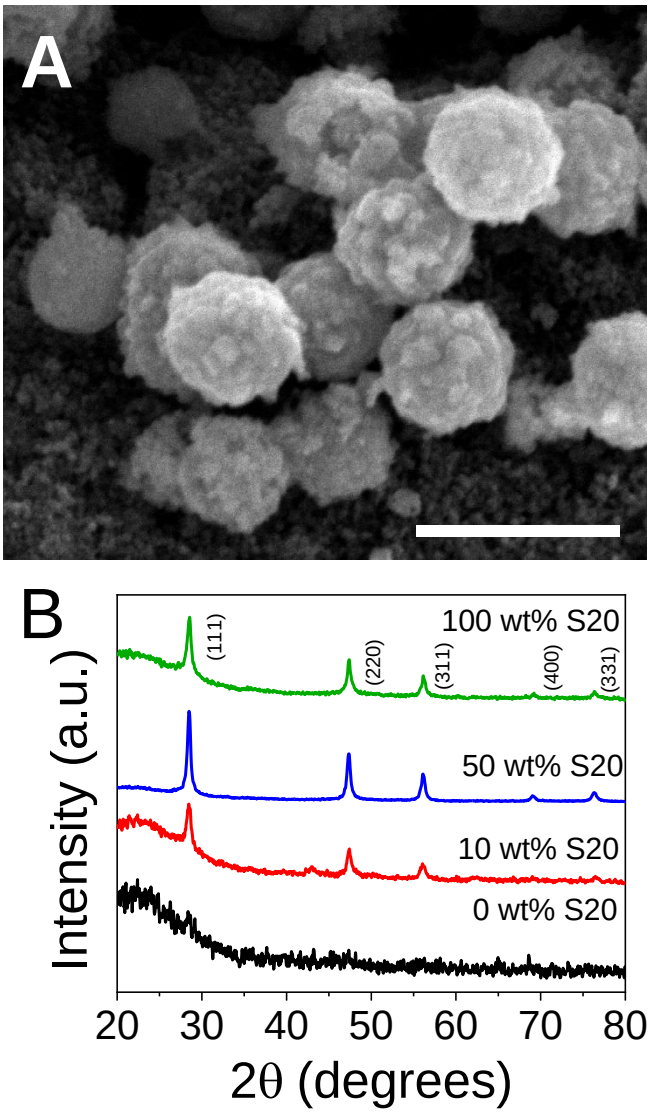

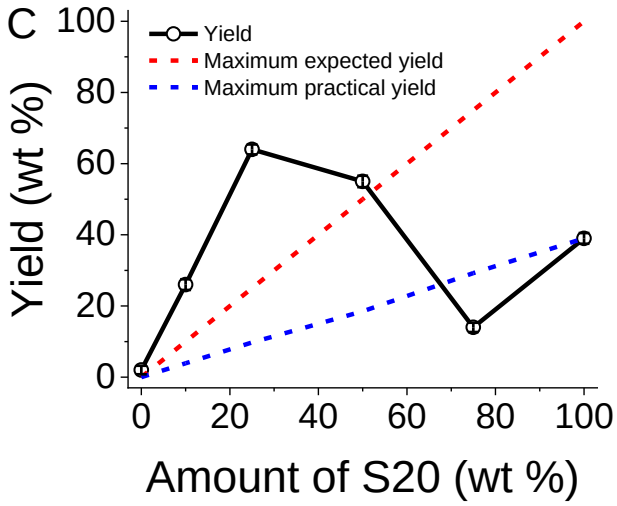

Figure 5.1: The SEM image shown in A) is the product of the reduction of 50 mol% of S20 mixed with S500 reduced at 450°C. Scale bar represents 1 µm. B) The diffractograms of mixed silica showing peaks corresponding to crystalline silicon after reduction at 450°C, in all samples except for 100 mol% S500. Samples containing mixed sizes are given in mol% of S20. The measured yield is shown in C) alongside the maximum expected and maximum practical yield (see text) for different mol% mixtures of S20 and S500 (see text for details).

The SEM image in Figure 5.1A for the reduction with an equal mixture of S20 and S500 showed that the latter have maintained their spherical shape upon MgTR at 450ºC, with specks on their surfaces. These specs resemble the freshly formed crystalline silicon reported for Stöber silicas reduced at 650°C[21]. The products of the mixed silica reductions all contained crystalline silicon, confirmed by XRD (Figure 5.11B). In order to understand the extent of reduction of larger particles and distinguish this with simply a reduction of small particles, the yields were calculated (Figure 5.1C). We created two hypothetical cases to be compared with the results. In the first case, 'the maximum expected yield', it was assumed that only small particles reacted at 450°C, and a maximum yield of 100% was achieved. In the mixed sample, a maximum yield will then equal to the percentage of small silica particles within the original sample. For example, a 75:25 wt% mixture of large and small particles should only give a 25 mol% yield. These maximum expected yields are shown in red in Figure 5.1C. Any increase in observed yield beyond this case provides direct evidence that larger particles were also reduced due to the triggering effect from the smaller particles. In the second hypothetical case, the 'maximum practical yield', experimental data from our previous work was used where the reduction of S20 alone gave a measured yield of 39 mol% at 450°C [23] as opposed to 100% assumed

in the first hypothetical case. Hence, for a mixture containing only 25 wt% S20, a yield of 39% of 25 wt% sample should be practically achieved (i.e. 9.75 mol%, shown in blue in Figure 5.1C). Any increase in the measured yield with respect to this second scenario suggests that either larger particles were also reduced (likely) or that S20 were reduced with higher yield due to the presence of S500 (unlikely). We note the dip in the yield for ther S20:S500 75:25 mixture, and the reason for this will be covered in the discussion section.

We observed that the measured yield from the “mixed” sample (black line in Figure 5.1C) exceeded both the maximum expected and maximum practical yield when S20 was <75% in the mixture. For example a sample with 25 wt% of S20, the maximum practical yield is 9.75 mol% and maximum expected yield is 25%. The measured yield however was found to be 62 mol%, showing that the synergistic effect of mixing the S20 and S500 particles increased the yield significantly. It is thus clear that S500 particles have been reduced (it is not possible to determine what proportion of S500 had been reduced). To further confirm that the larger particles were in fact being reduced at 450°C, samples post-MgTR were analysed using TEM (Figure 5.2). S500 silica remained unreacted at 450°C (Figure 5.2A and B). The particles in these images were intact and non-porous spheres, which confirms the XRD and yield results (shown in Figure 5.1) that no reaction has occurred. However, a dramatic change in the S500 particle microstructure was observed when this sample was mixed with S20 before MgTR (see Figure 5.2C and D). Interestingly, the mild nature of this low-temperature reduction the retained the spherical structure, while the formation of smaller crystals was evident, which is in stark contrast to those shown in Figure 5.2A and B. This, along with other results, confirmed the reduction of silica to Si at 450°C with a yield of 62 mol%. This change in microstructure only when the silicon crystals are formed strongly corroborates with the MgTR pathways reported elsewhere[18]. The appearance of crystalline phases, in an otherwise amorphous precursor silica, were seen throughout the particles (Figure 5.2E, red arrows), which further confirms that S500 particles have been reduced to crystalline silicon.

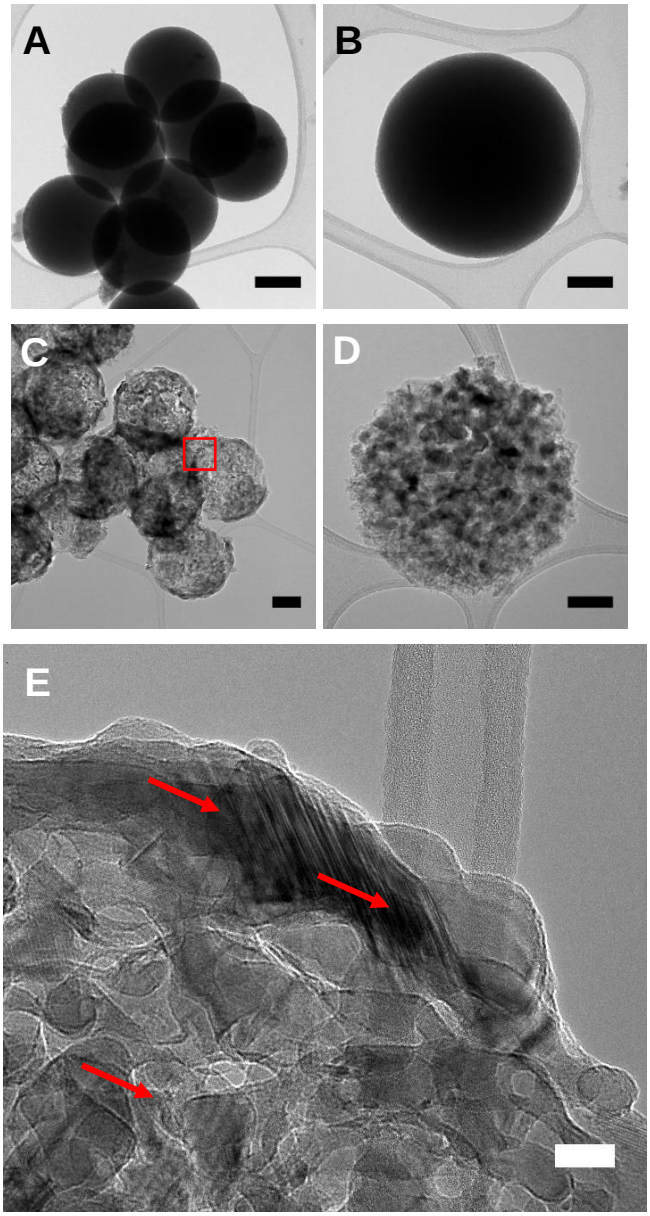

Figure 5.2: TEM images of Stöber silica heated with Mg to 450°C are shown. In A) and B) S500 was the only silica source. In C) and D), a 50-50 wt% mixture of S500 and S20 was used. A higher magnification of the red marked area in image in C) is shown in E) with crystalline phases marked by red arrows. Scale bars are 200 nm (A, C), 100 nm (B, D) and 20 nm (E).

It appears that the presence of both small and large particles provides thermal regulation, while also triggering the reduction of larger particles. As reported earlier, the MgTR reaction is able to proceed at 450°C for particles ≤20 nm, the exothermic heat released from the reduction of small particles is likely to provide the activation energy need to trigger the reduction of large particles. This synergistic effect between the reduction of large and small particles has until now, not been reported in the literature. While this low temperature MgTR enabled by the nanoscale effects is novel, we wanted to understand if this effect applies beyond the model Stöber silica colloids.

5.5.2. Reduction of commercial silicas

If it is possible to trigger the reduction of commercially available cheaper SiO_2 at low temperatures (<450˚C) using a minority amount of nanoparticles, MgTR will become increasingly viable commercially. In order to determine whether such synergy could be applied to other silicas, the reduction was performed with commercial silica samples. Syloid AL 1-FP (Grace), a porous silica gel with 6μm particle size was chosen to represent a sample containing large particles (>>20 nm). This sample will be called Sy. We have already shown that fumed silica (F7), a commercially available 7 nm silica, was able to undergo MgTR at temperatures as low as 380°C, so we chose this silica to trigger the MgTR of Sy. In order to establish a baseline, initially each sample was reduced separately at 450°C and 650°C. The XRD results of the products are given in Figure 5.3A. Both samples produced crystalline silicon at 650°C as expected, however only F7 showed conversion to Si at temperatures ≤450°C, in agreement with our previous work.

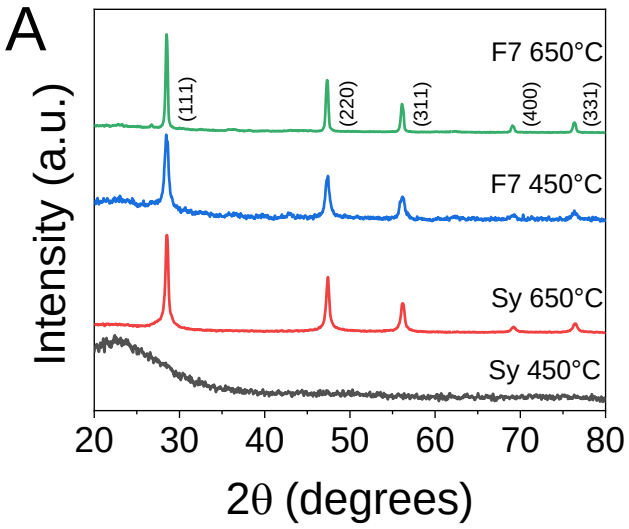

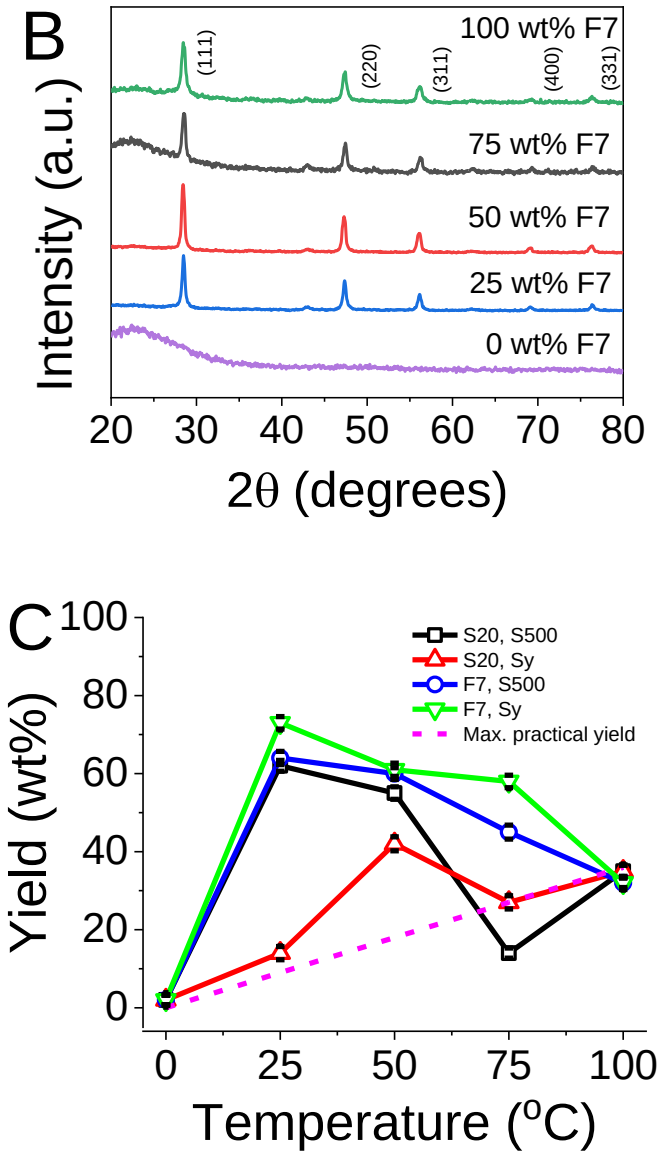

Figure 5.3: (A) The diffractogram of the reduction products at 450°C of commercial silica samples are given. The samples were reduced separately (not mixed). B) XRD of F7, Sy and their mixtures reduced at 450°C. C) The yields for silica mixed at different mol% and reduced at 450°C. S20 and F7 are small, or 'trigger' particles. The maximum practical yield is included as a comparison.

Next, silica nanoparticles (F7) and large silica (Syloid, Sy) were mixed at various ratios (F7 mixed with Sy from 0 to 100 wt%). These mixtures were reduced at 450°C and the XRD results are shown in Figure 5.3B. Every sample containing F7 produced crystalline silicon, while evident from the lack of peaks in Figure 3B, Sy without F7 did not produce any crystalline Si. This is the first report of bulk silica being reduced to silicon at 450°C. This shows that the triggering effect of particles ≤20 nm is

widely applicable and opens the possibility of reducing commercial silica at low temperatures, thereby offering potential routes to economical and sustainable production of porous Si.

We further extended this to two additional mixed systems of S20 (instead of F7) with Sy and separately F7 with S500. The yields for the mixed systems are shown in Figure 5.3C. For S500 in a mixed system, the yield was recorded as 62 mol% at 450°C when 25% of small particles were used (either S20 or F7). In contrast, a pure sample of S500 has to be reduced at temperatures above 700°C in order to achieve a similar yield. This trend can be seen in the mixed Sy samples (e.g. 25 wt% F7 with Sy), whereby a 73 mol% yield is achieved at 450°C. However, it is only possible to exceed this yield for Sy (unmixed) samples at 650°C or above (Table 2). This ability to lower the MgTR temperature requirement by triggering the reduction of a low-cost feedstock using small amount of nanoparticles (≤20 nm) is highly desirable from sustainability and economic standpoints.

In our previous work, we identified the lower temperature limit for MgTR of 380°C using F7 particles. Having shown here that the triggering effect can be applied to commercially available silica, we reduced mixtures of F7:Sy at 380°C. XRD showed that silicon could be formed for this mixture at 380°C (Figure 5.4A). Further, irrespective of the mixture ratio used (25:75 or 50:50), it was found that the yields achieved at 380°C were higher than when reduced at 450°C (Figure 5.4B and Table 1, 2). While the high yield at low temperatures is promising, extensive future work is required to probe the observed complex interactions between temperature and yield. However, we can speculate that the changes in the yield are due to the temperature dependence of the multiple reactions occurring simultaneously. These reactions, which are producing and consuming Si, include the direct reduction of silica to silicon (Eqn. 1 in the introduction), the formation of magnesium silicide (Mg_2Si) which consumes Si and the conversion of Mg_2Si to Si. The kinetics and thermodynamics dictate the balance between these reactions at a given temperature[26,27], which in turn is likely to drive the trend in silicon yields observed in Figure 5.4C. We also speculate that the reason for the dip in the yield observed in Figures 5.1C and 5.3C is due to the size-dependent reactivities that increase the rate constant of the Si formation reaction, thus favouring the consumption of Si beyond a certain ratio of the mixture. It is speculated that smaller particles have a higher effective rate constant than larger particles, so the

rate of heat release from the reaction will be greater. This accumulation of heat could then speed up the reaction which forms Mg_2Si, leading to a depletion of Si. The increased rate of reaction of smaller SiO_2 particles would also result in a higher concentration of Si being formed quickly, which would also favour the formation of Mg_2Si. Mg_2Si can be oxidised by SiO_2 under Ar atmosphere to once again form Si, however if the remaining SiO_2 consist of 500 nm particles that have not reacted, this oxidation reaction could be hindered if the rate of reaction of 500 nm particles is low due to particle size.

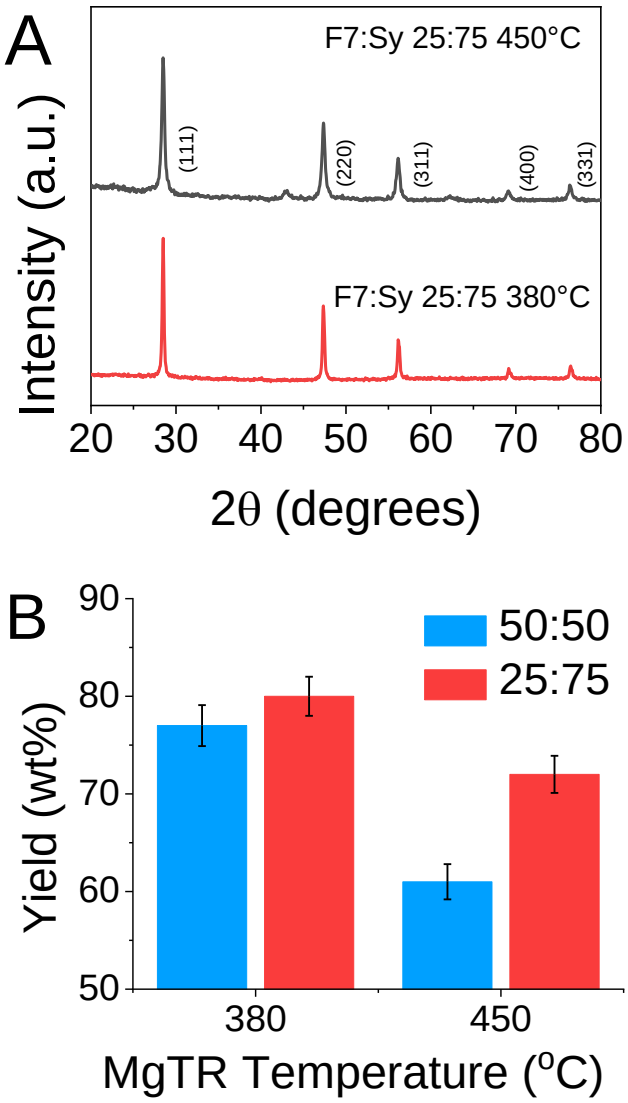

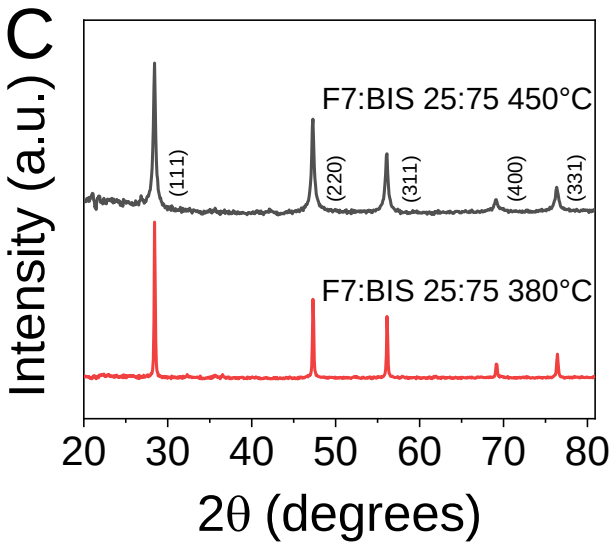

Figure 5.4: XRD (A, C) and yield (B) of mixed systems reduced at 380ºC and 450ºC. (C) Yields for F7-Sy mixed system.

Bioinspired silica was identified in our previous study as the best feedstock for the magnesiothermic reduction – the silicon produced exhibited the highest initial capacity (3270 mAh/g) and best capacity retention over 100 cycles[18]. Therefore, in this study, bio-inspired silica (BIS) was synthesised and reduced with F7 in an effort to produce high yield of electrochemically active silicon using our novel, low-temperature reduction method. BIS was produced using a method that was developed in our group[28] (also described in the Experimental section). This was then mixed with F7, at a ratio of 25:75 F7:BIS. This ratio was chosen since it produced the highest yield in the F7 and Sy mixtures. The mixture was then reduced at 380 and 450°C. The XRD results (Figure 5.4C) showed that all samples contained crystalline silicon. The yield of each sample was measured, and the results are shown in Table 5.1. The yield of F7:BIS 25:75 reduced at 380°C was higher than the same sample reduced at 450°C, similar to that seen in the F7:Sy samples. Another interesting result is that the yield of F7:BIS mixed sample at 380°C (73 mol%) is similar to the yield of BIS alone at 650°C (70 mol%), see Table 5.1.

Table 5.1: The yield of Syloid or BIS-containing samples, mixed with or without F7 nanoparticles are given for various MgTR temperatures (T). Note that Sy or BIS did not reduce at temperature 450 ^{O}C or below, hence for comparison, data from their reduction at 650 ^{o}C is shown.

Sample	**T** *(°C)*	**Yield** *(mol%)*
F7:Sy 25:75	380	80 ± 1.2
	450	72 ± 1.7
Sy	650	64 1.5
F7:BIS 25:75	380	73 ± 1.2
	450	60 ± 1.4
BIS	650	70 ± 1.7

The fact that the yield changes dramatically with temperature suggests that the thermodynamics and kinetics of the competing reactions change with respect to each other. A silicon producing reaction may have a higher rate than a silicon consuming reaction at lower temperatures, which would give rise to higher yields at 380°C compared to 450°C. An understanding of the kinetics and thermodynamics of the reaction will provide insight into the observed trend between yield and temperature and this will be the focus of future work.

5.5.3. Electrochemical performance

Having shown that the triggering effect can be used to convert commercially available silica to porous Si with high yields yet at ultra-low temperatures, the electrochemical performance of the Si with the best yields were investigated next. Since the mixtures containing 25% small particles had the highest yield, they were chosen for electrochemical testing.

S20 particles (alone) are able to undergo reduction at 450°C, hence their electrochemical performance was investigated for comparison with other samples including large particles (alone) and various mixtures of small and large particles. We found that the electrochemical performance of S20 particles that were reduced at 450°C was poor (<250 mAh/g in each cycle), as seen in Figure 5.5A and Table 2. A peak at 0.45V in the differential capacity plot for this sample in Figure S9 indicated that silicon was accessed during charge and discharge[29], but the low capacity was likely due to the low yield 35% at this temperature. This low yield resulted in a lack of connectivity between regions of

Si, isolated by the high amount of unreacted SiO_2 still present in the sample. Thus it is clear that although S20 could be reduced at ultra-low temperatures, the product silicon was not suitable for use in lithium-ion cells.

On the other hand, when S500 sample was used alone, the reduction was only possible at 650°C (with a yield of 55%). The reduced S500 product showed a high initial capacity of 955 mAh/g, dropping to 523 mAh/g after 100 cycles (Figure 5.5A). This performance only slightly exceeded expected maximum capacity of graphite. Further, the need for a high temperature its reduction (650°C) means that S500, when used alone is not an attractive feedstock for producing Si for anodes. However, when a mixture of S20 and S500 was used, a yield of 64% was achieved when the mixture was reduced at 450°C (noted above). This higher yield translated to a high initial capacity of 1020 mAh/g, maintaining 853 mAh/g after 100 cycles (Figure 5.5A). This performance of the mixed system surpasses that of each part of the mixture, which highlights synergistic and beneficial effects of this triggering mechanism. Firstly, it provides a sustainable process by lowering the energy cost required for the reduction reaction. Secondly, it enables higher yields despite reducing the materials at lower temperatures. Finally, the mixed systems exhibit improved electrochemical performance.

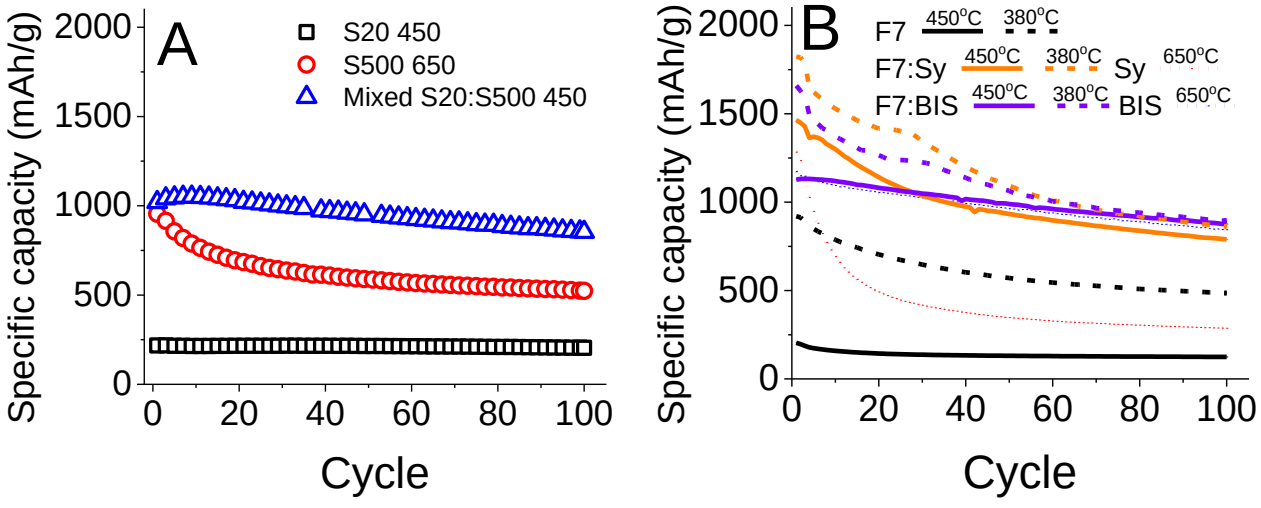

Figure 5.5 A) The specific capacities of Stöber silica particles mixed and unmixed, reduced at 450 °C, are shown over 100 cycles. B) The electrochemical performance of mixed and unmixed silicas – the mixtures used 25% F7. Solid, dashed and dotted lines represent samples reduced at 450°C, 380°C and 650 °C, respectively.

Stöber silicas offer an ease of particle size control at lab scale, thereby enabling a proof of the triggering concept. Further, it serves as a baseline for comparing MgTR yield and electrochemical performance between various samples reduced at different temperatures. However, it is well known that scaling up the synthesis of Stöber silica is challenging due to its process requirements, hence, it is not a commercially attractive silica feedstock for producing silicon anodes. In order to address these issue, we have turned to low-cost, high-volume commercial silicas (F7 and Sy). F7 reduced at both 450°C (yields of 31%), showed poor electrochemical performance with capacities not exceeding 250 mAh/g in each cycle (Figure 5.5B). Again, like S20 reduced at 450°C, this is likely to be due to the low yield. When F7 was reduced at 380°C (yields of 58%), however, its high yield translated to a high initial capacity of 920 mAh/g, fading to 485 mAh/g after 100 cycles. Hence, similar to S20, the silicon produced from F7 at ultra-low temperature was not suitable for use in lithium-ion cells.

The 'large' commercial silica Sy, similar to S500, needs a reduction temperature of 650°C. Although Sy reduced at 650°C achieves a yield of 69% and hence a high initial capacity of 1283 mAh/g (Figure 5B), it has an extremely poor capacity retention, fading to 287 mAh/g after 100 cycles (a capacity fade of 77%). This makes Sy an unsuitable candidate as a sole precursor for an anode material. Sy reduced at 650°C has a high SSA of >300 m^2/g, and this favours SEI formation and irreversible reaction with Li. This explains its dramatic capacity loss within the first 20 cycles. However, for the mixture of F7 and Sy, which could be reduced at 380°C (yield of 80%, noted above), an initial capacity of 1822 mAh/g was recorded (Figure 5.5B). Over 100 cycles, the capacity stabilised to 860 mAh/g. A similar trend was seen for the F7 and Sy mixture reduced at 450°C. We then turned to evaluate the electrochemical performance of bioinspired silica (BIS) as an emerging grade of silicas that are low-cost, high-value materials, yet produced sustainably[30]. When reduced at 450°C, BIS had an initial capacity of 1127 mAh/g, stabilising to 876 mAh/g after 100 cycles, with only 22% capacity fade (Figure 5.5B). This performance was almost identical to BIS reduced at 650°C, which is encouraging because it means that BIS can be produced with significantly lower energy input yet retaining its performance. BIS reduced at 380°C also had similar capacity after 100 cycles, however, there was a higher capacity fade when compared to BIS reduced at 450°C or 650°C. The results from both, the commercial silicas

and BIS, strongly support the fact that the triggering effect has enabled the ultra-low temperature reduction of silicas to higher-performance silicon that are suitable as anodes in Li-ion batteries.

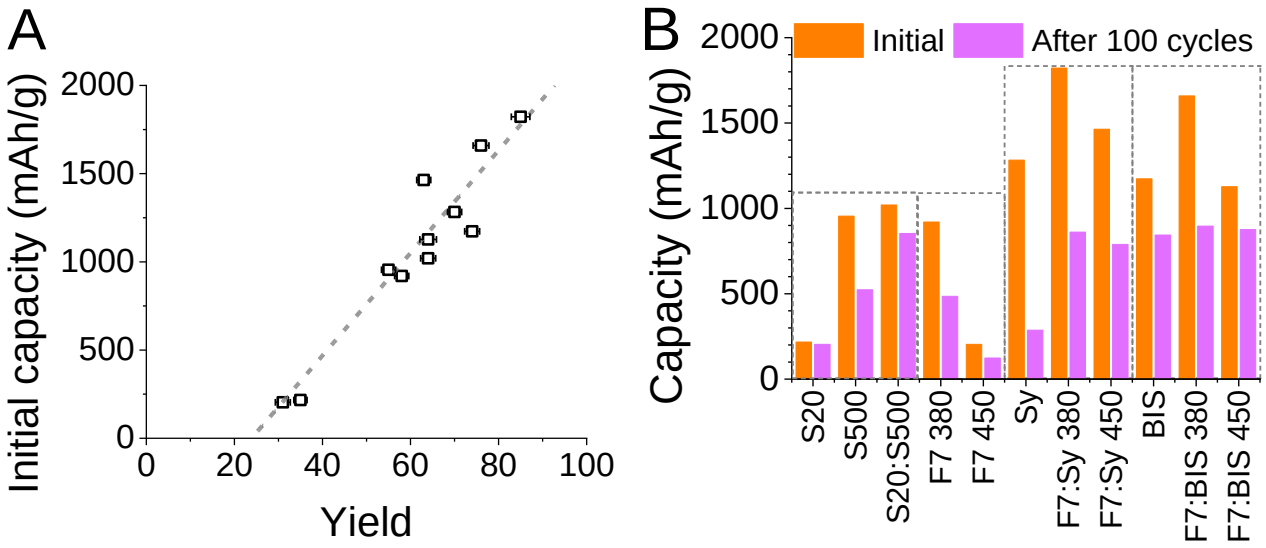

Figure 5.6: A) The initial capacities are compared with their respective yields. B) The capacities for first cycle and after 100 cycles are compared.

It is known that the electrochemical performance is dependent on complex relationships between the yield, purity, porosity (surface area and pore volume) and the interconnectivity of active components. As such, using the results listed in Table 5.2 in an effort to correlate the porosity data with capacities (initial or final) and capacity fade, no trends were obvious (data not shown). However, a linear correlation between the initial capacity and yield can be seen (Figure 5.6A). This is expected because as more silicon is present and accessible, the capacity will be higher. From Figure 5.6B it can be seen that samples reduced at either 380 or 450°C exhibit similar or higher capacities than their sole counterparts reduced at a higher temperature. This is consistent throughout all the samples investigated herein.

Table 5.2: The properties and electrochemical performance of samples post-MgTR using mixed (ratio of 25:75, shown in bold) and unmixed silicas. S20 and S500 are Stöber silicas, F7 is fumed silica, Sy is Syloid and BIS is bioinspired silica. The full porosity data is included in supporting information (Figures S1-S8).

Sample	Yield *(mol%)*	Capacity *(mAh/g)*		Specific surface area *(m^2/g)*	Total pore volume *(cm^3/g)*
		Initial	After 100 cycles		
S20 450°C	35 ± 1.5	217	204	143	0.24
S500 650°C	55 ± 1.6	955	523	179	0.29
S20:S500 450°C	**64 ± 1.4**	**1020**	**853**	**219**	**0.55**
F7 380°C	58 ± 1.8	920	485	70	0.16
F7 450°C	31 ± 1.7	204	124	177	0.47
Sy 650°C	69 ± 1.6	1283	287	348	0.45
F7:Sy 380°C	**81 ± 1.2**	**1822**	**861**	**112**	**0.24**
F7:Sy 450°C	**63 ± 1.6**	**1464**	**789**	**165**	**0.41**
BIS 650°C	74 ± 1.7	1173	844	216	0.77
F7:BIS 380°C	**76 ± 1.5**	**1659**	**896**	**105**	**0.27**
F7:BIS 450°C	**64 ± 0.8**	**1127**	**876**	**231**	**0.51**

5.6. Conclusion

We have shown for the first time that by taking advantage of the triggering effect of nano-sized silica particles, larger particles can be reduced at 380°C, giving yields that could previously only be achieved at 650°C or above. The silicon produced through this method exhibits superior electrochemical performance when compared with silicon made at higher temperatures. The highest yields can be achieved with a mixture containing 25 wt% small particles. The highest initial capacity of 1822 mAh/g was achieved with a sample containing F7 and Sy with a weight ratio of 25:75, reduced at 380°C, while the mixed silicas containing BIS showed the least capacity fade over 100 cycles.

There are multiple benefits of the triggered reduction we have presented here. Firstly, silica made up of larger particles which have previously been reduced at high temperatures and demonstrated to have good electrochemical performance can now be reduced at ultra-low temperatures to give the same, or better performance. Silica consisting of particles ≤20 nm can undergo reduction ≤450°C however, here we have shown that reducing these types of silica singularly does not produce high performance porous silicon. The second benefit is therefore that through triggering, a synergistic

effect is observed between small and large particles, which minimised the impact of low performing small particles while also dramatically reducing the energy requirements. Indeed, our preliminary calculations show that lowering the MgTR temperature from 650°C to 380°C leads to a reduction by 45% in the total reduction energy cost. Finally, we have also shown that this strategy of triggering the MgTR at low temperatures is not restricted to Stöber silica and is transferrable to commercial silicas made via different synthesis routes. As such, cheap feedstock which is available in large volumes can be converted into high performance porous silicon anodes at low temperatures.

Taken together, the discovery of achieving silicon production at low temperatures by using bulk silica precursors, yet offering stable and high capacities has the potential for a sustainable, economical and scalable method for producing high-value silicon for applications in the energy sector. Further, given the widespread use of metallothermic and other solid state reactions in wider industry, our findings have far-reaching potential. The next steps towards making the ultra-low temperature MgTR commercially relevant is building an understanding of the reaction mechanisms at low temperatures. A kinetic and/or thermodynamic study would prove indispensable in revealing how the side reactions affect the yield and porosity observed herein.

5.7. Acknowledgements

The authors thank EPSRC for funding this research (EP/L016818/1, EP/P006892/1 and EP/R025983/1). M.Y. thanks the CDT for Energy Storage and its Applications. Dr Jake Entwistle (Lancaster University) and Prof. Gregory Beaucage (University of Cincinnati) are thanked for helpful discussions.

5.8. References

1 P. Hagenmuller, Preparative methods in solid state chemistry, Academic Press, 1972.

2 S. E. Dann, Reactions and Characterization of Solids, Royal Society of Chemistry, Cambridge, 2000.

3 D. Larcher and J. M. Tarascon, Nature Chemistry, 2015, 7, 19–29.

4 M. N. Obrovac, L. Christensen, D. B. Le and J. R. Dahn, Journal of The Electrochemical Society, 2007, 154, A849.

5 C. Shen, M. Ge, L. Luo, X. Fang, Y. Liu, A. Zhang, J. Rong, C. Wang and C. Zhou, Scientific Reports, 2016, 6, 1–11.

6 F. Shi, Z. Song, P. N. Ross, G. A. Somorjai, R. O. Ritchie and K. Komvopoulos, Nature Communications 2016 7:1, 2016, 7, 1–8.

7 Y. He, L. Jiang, T. Chen, Y. Xu, H. Jia, R. Yi, D. Xue, M. Song, A. Genc, C. Bouchet-Marquis, L. Pullan, T. Tessner, J. Yoo, X. Li, J.-G. Zhang, S. Zhang and C. Wang, Nature Nanotechnology, 2021, 16, 1113–1120.

8 C. K. Chan, H. Peng, G. Liu, K. McIlwrath, X. F. Zhang, R. A. Huggins and Y. Cui, Nature Nanotechnology, 2008, 3, 31–35.

9 H. Wu and Y. Cui, Nano Today, 2012, 7, 414–429.

10 D. H. Filsinger and D. B. Bourrie, Journal of the American Ceramic Society, 1990, 73, 1726–1732.

11 M. P. Stewart and J. M. Buriak, Advanced Materials, 2000, 12, 859–869.

12 D. Losic and A. Santos, Electrochemically engineered nanoporous materials, 2015.

13 J. Entwistle, A. Rennie and S. Patwardhan, Journal of Materials Chemistry A, 2018, 6, 18344–18356.

14 Z. Bao, M. R. Weatherspoon, S. Shian, Y. Cai, P. D. Graham, S. M. Allan, G. Ahmad, M. B. Dickerson, B. C. Church, Z. Kang, H. W. Abernathy, C. J. Summers, M. Liu and K. H. Sandhage, Nature, 2007, 446, 172–175.

15 Z. Favors, W. Wang, H. H. Bay, Z. Mutlu, K. Ahmed, C. Liu, M. Ozkan and C. S. Ozkan, Scientific Reports, 2014, 4, 5623.

16 N. Liu, K. Huo, M. T. McDowell, J. Zhao and Y. Cui, Scientific Reports, 2013, 3, 1–7.

17 C. Li, C. Liu, W. Wang, Z. Mutlu, J. Bell, K. Ahmed, R. Ye, M. Ozkan and C. S. Ozkan, Scientific Reports, 2017, 7, 1–11.

18 J. E. Entwistle, G. Beaucage and S. v. Patwardhan, Journal of Materials Chemistry A, 2020, 8, 4938–4949.

19 M. Waitzinger, M. S. Elsaesser, R. J. F. Berger, J. Akbarzadeh, H. Peterlik and N. Hüsing, Monatshefte fur Chemie, 2016, 147, 269–278.

20 Handbook of the Physicochemical Properties of the Elements, , DOI:10.1007/978-1-4684-6066-7.

21 S. A. Martell, Y. Lai, E. Traver, J. MacInnis, D. D. Richards, S. MacQuarrie and M. Dasog, ACS Applied Nano Materials, 2019, 2, 5713–5719.

22 Y. Lai, J. R. Thompson and M. Dasog, Chemistry - A European Journal, 2018, 24, 7913–7920.

23 M. Yan and S. v. Patwardhan, RSC Advances, 2021, 11, 35182–35186.

24 W. Stöber, A. Fink and E. Bohn, Journal of Colloid And Interface Science, 1968, 26, 62–69.

25 I. S. Curtis, R. J. Wills and M. Dasog, Nanoscale, 2021, 13, 2685–2692.

26 T. Henmi, T. Shiono, K. Matsubara, T. Kiyomura, Hiroki Kurata, T. Wakasugi, A. Okada and K. Kadono, Wiley Online Library, 2020, 2, 66–75.

27 K. K. Larbi, M. Barati and A. McLean, Canadian Metallurgical Quarterly, 2011, 50, 341–349.

28 J. Manning, E. Routoula and S. Patwardhan, jove.com.

29 M. N. Obrovac and L. J. Krause, Journal of The Electrochemical Society, 2007, 154, A103.

30 C. Brambila, P. Boyd, A. Keegan, P. Sharma, C. Vetter, E. Ponnusamy and S. v Patwardhan, 2022, 15, 40.

6. Large-scale manufacturing of porous silicon via the magnesiothermic reduction: a techno-economic analysis

Maximilian Yan [a,b], Sarah Martell[b], Mita Dasog[b], Solomon Brown[a] and Siddharth V. Patwardhan[a]*

[a] *Department of Chemical and Biological Engineering, The University of Sheffield, Mappin Street, Sheffield S1 3JD, United Kingdom.*

[b] *Department of Chemistry, Dalhousie University, 6274 Coburg Road, Halifax, NS B3H 4R2, Canada.*

* *Corresponding author, s.patwardhan@sheffield.ac.uk*

6.1. Contributions

I performed the technoeconomic calculations and prepared the manuscript. SP helped with the editing of the manuscript. Experimental planning and data collected for this paper were jointly performed by me and SM. In particular, SM performed two-step reductions and measured the associated yield. I performed low-temperature (360°C and 380°C) and baseline reductions as well as the yield measurements for both reductions. I also performed electrochemical testing. SM led, while I assisted with the synthesis of the Stöber particles used in the two-step, baseline and low-temperature reduction. MD and SP advised on the experimental planning and SB advised on planning of the techno-economic analysis.

Large-scale manufacturing of porous silicon via the magnesiothermic reduction: a techno-economic analysis

Maximilian Yan[a,b], Sarah Martell[b], Mita Dasog[b], Solomon Brown[a] and Siddharth V. Patwardhan[a]*

[a] *Department of Chemical and Biological Engineering, The University of Sheffield, Mappin Street, Sheffield S1 3JD, United Kingdom.*

[b] *Department of Chemistry, Dalhousie University, 6274 Coburg Road, Halifax, NS B3H 4R2, Canada.*

** Corresponding author, s.patwardhan@sheffield.ac.uk*

6.2. Abstract

Lithium-ion batteries play a central role in the electrification of our energy systems. This technology still suffers from low energy density, and porous silicon has been recognised as a promising, high-energy density anode material. The demand for porous silicon is therefore expected to increase in the coming decades and to meet this demand, magnesiothermic reduction process (MgTR) has shown promise as a scalable method of production. However, it is still unknown whether MgTR is economically feasible at larger scales. In this work, the total cost of production (TCOP) at scales between 300-1500kg/batch are calculated using experimentally verified data. Fixed costs make up the greatest proportion of TCOP, at £32/kg at the largest scale, with a payback time of 10 years. Total variable costs (feedstock and energy) was £22/kg. When recently reported modifications to MgTR – a two-step and a low-temperature methods – were considered, the variable costs reduced to £14/kg and £17/kg respectively. The TCOP for the two-step and low-temperature methods were £46/kg and £48/kg respectively. These results provide the first evidence that the MgTR is a highly competitive and scalable process for producing anode grade porous silicon. The variable costs can be lowered in the future by changing the conditions, and the most effective ways to do this are presented in this study.

6.3. Introduction

In the shift towards a net zero carbon economy, the demand for high energy density lithium-ion batteries (LIBs) is increasing fast[1]. Although they are currently dominating the electric vehicle market, the issue with low mileage has yet to be tackled. A typical mass market EV has a mileage of 67 kWh, equivalent to 224 Wh/kg at cell level, capable of achieving a mileage of only 168 miles in a single charge[2]. This energy density is still far below the target of ≥350 Wh/kg by the year 2030 set by the US Department of Energy and the Batteries Europe strategy[3,4]. At present, the anode material of choice is graphite, however, in order to meet these targets, higher energy density materials need to be considered. Furthermore, between 50-70% of the raw graphite is lost when it is upgraded to spherical, battery grade graphite, making it a highly inefficient process, thus multiplying demand and raising supply chain issues [5]. Silicon is one of the most promising anode materials because it possesses a high specific capacity of 3579 mAh/g[6] and is produced from silica, an abundant feedstock. Pure silicon is made by the carbothermal reduction of silica at 2000°C[7]. Converting this into porous silicon which is suitable for use in LIBs requires electrochemical etching, which is a top-down, surface method, making it not only unsustainable, but difficult to scale[8]. The magnesiothermic reduction (MgTR) is an alternative method which can produce porous silicon directly from a wide range of silica feedstock at 650°C[9]. Mg and SiO_2 in powder form are mixed together then heated in a furnace at a chosen temperature between 650°C and 800°C. The time required to reach completion is dependent on the feedstock properties and parameters. There is no systematic study that includes more than one silica type reduced under different parameters, to identify the point of reaction completion. Though the reaction has been shown to produce Si after 30 minutes[10] the reaction is usually held for much longer times (6 hours) to ensure reaction completion[11], under an inert atmosphere. Once the mixture is cooled, it is etched in aqueous HCl to remove Mg containing species, leaving behind porous Si and unreacted SiO_2.

Typically, the MgTR reaction is carried out at 650°C for 6 hours and achieves a yield of 60% with excellent porosity that is desired for the electrochemical performance. Increasing the reaction temperature to 850°C achieves the yield of 90% but at a loss of porosity, while operating at 500°C to

retain the porosity, decreases the yield to less than 10%[12]. A high yield of Si is important as with any other manufacturing process, however, the silicon produced needs to have the correct porosity for energy storage application. The tension between high temperature requirement to achieve higher yields and producing silicon with desired porosity for its performance makes it difficult to improve the efficiency without sacrificing the electrochemical performance. Additionally, to improve the purity of the product, excess unreacted SiO_2 have to be removed using highly toxic HF. This is not only wasteful due to the loss of the unreacted feedstock, but also is unsafe. Multiple ways have emerged in the literature showing that it is possible to modify the process to improve the energy efficiency of the process and the yield of porous silicon produced.

One such modification is the two-step process, which needs 650°C for only 30 minutes to trigger the reduction, before cooling to 300°C to carry out the reaction for 6 hours[13]. This method is potentially advantageous economically as most of the reduction time is spent at a lower temperature, hence it is likely that less energy is required overall to maintain the temperature during the dwelling stages. Another modification to the MgTR process is to reduce the operating temperature. It was shown recently that the reaction can be carried out at 380°C by exploiting the high reactivity of nano-sized particles[14]. The likely economic benefit of this method is that the temperature of the furnace never exceeds 380°C, therefore it has the potential for minimising the overall energy consumption and cost. As a third strategy, without lowering the maximum temperature requirement, it was demonstrated that the yield at 750°C could be increased from 55% to 92% by using a rotating furnace during the reduction step to minimise mass transfer limitations[15]. Other works have shown that the MgTR can produce silicon with properties that are suitable for high-capacity lithium-ion cells using low-cost feedstock such as sand[16], crushed glass[17], and clays[18]. The studies described above can help reduce or remove the tension between temperature requirement to achieve high yield and porosity needed for the electrochemical performance, thereby presenting multiple strategies for improving the process to make the MgTR more economical and increasing its viability for scale up.

Despite the huge potential of MgTR for scale-up and recent process improvements, the process economics of producing silicon via the traditional MgTR method is not known. Therefore, neither the

commercial viability of MgTR can be explored, nor the savings from implementing improved methods be quantified. In this work we use well-established factorial methods to estimate the total cost of producing porous silicon via the MgTR process. We then aim to implement experimentally verified process modifications, specifically the two-step and low temperature methods. The total cost of production (TCOP) will be estimated and analysed to gain process insights. The results will be then used to propose future improvements and to identify ways to reduce the variable costs (VC), annualised fixed costs (FC) and TCOP.

6.4. Process overview

The process consists of primarily solids handling equipment with liquid handling equipment during the downstream processing steps. Dry powders of Mg and SiO_2 are mixed before being transferred into a tubular furnace and heated to a desired temperature under inert atmosphere. The solid mixture is then cooled and mixed with aqueous HCl. Compounds containing Mg react with HCl to form $MgCl_2$ which remains in solution, while solid Si and unreacted SiO_2 remain as solids suspended in the solution. After all Mg containing species have been reacted, the suspension is passed through a filter to separate the solids. A filter cake is obtained which, when dried, leaves a powder consisting of Si and unreacted SiO_2. A block diagram of the process is shown in Figure 6.1.

Figure 6.1: A flow diagram showing the individual steps in the process. Steps which include reactions are coloured in blue.

6.4.1. Reaction stoichiometry

Under an inert atmosphere, Mg and SiO_2 undergo a redox reaction, whereby SiO_2 is reduced to Si (Reaction 1). Competing intermediate reactions can occur, which consume and produce Si, affecting the yield. Mg can react with Si to form Mg_2Si, and this can further react with SiO_2 to form Si again. If Mg_2Si is not converted back into Si before being removed from the furnace, it reacts with HCl and O_2 during the dissolution step to form SiO_2 and $MgCl_2$, resulting in a loss of Si yield.

$$2Mg_{(s)} + SiO_{2(s)} \rightarrow 2MgO_{(s)} + Si_{(s)} \quad \text{Reaction 1}$$

Given that Mg_2Si ultimately ends up as SiO_2 and $MgCl_2$, only Reaction 1 is used to calculate stoichiometric requirements. The overall yield is defined as the moles of elemental Si divided by the total moles of Si + SiO_2 in the product. Any Mg still present in the reaction after the furnace, as well as MgO produced are removed during the dissolution steps via Reaction 2 and 3 respectively.

$$Mg_{(s)} + 2HCl_{(aq)} \rightarrow MgCl_{2\,(aq)} + H_{2\,(g)} \quad \text{Reaction 2}$$

$$MgO_{(s)} + 2HCl_{(aq)} \rightarrow MgCl_{2\,(aq)} + H_2O_{(l)} \quad \text{Reaction 3}$$

6.5. Methods

6.5.1. Demand and costing

To perform an economic analysis of the process including capital and operating costs, a production capacity had to be defined. The demand for porous silicon was found from strategies outlined by government organisations. In the UK, the Society of Motor Manufacturers and Traders (SMMT) estimates, based on the UK electric vehicle infrastructure strategy, that the manufacturing capability in the UK will have to reach 60 GWh/y by 2030. This is equivalent to 895,000 million EVs/y assuming a mass market EV such as the Nissan Leaf is capable of storing 67 kWh in a single charge. In such a vehicle, 25 kg of graphite is needed for the anode. The Batteries Europe Strategy has set a target of 20% of graphite anodes to be replaced by Si anodes by 2030. The yearly silicon demand for anodes in the UK by 2030 was calculated as follows:

$$Si_{demand} = 0.2 \times \frac{kg\ graphite}{EV} \times \frac{no.of\ EV}{year} \quad \text{Eqn. 1}$$

The demand for silicon was estimated to be 45 tonnes/year of Si. The production capacity was therefore 180 kg/d, assuming 1% of the market demand and 5 days/week, 50 weeks/year of operation. Scheduling and equipment configuration is outside the scope of this study, so it was assumed that

this quantity was produced in 1 batch, and that 1 batch can be completed in a day. The demand calculation provides an order of magnitude and allows the effect of scaling up to a greater capacity on the TCOP to be explored.

6.5.1.1. Plant design and equipment selection

Existing industrial equipment were chosen as outlined in chemical engineering equipment design literature[19,20], based on the physical requirements of the MgTR process (Figure 6.1). Once the appropriate equipment were selected, the size of each equipment was calculated based on parameters and conditions from the literature and our own experimental results. From this, the capital cost of the equipment could be estimated from well-established factorial methods[21]. The selection and sizing of each major equipment is outlined below. Where available, specific costing charts and correlations were used[22], otherwise, a more general costing equation was used [21]. Given the limited information available, design with this level of detail gives a "preliminary cost" and is associated an error of ±30%[19]. In all cases where exact values and percentages were not available, estimates were made conservatively to give an overestimate of costs.

6.5.1.2. Spiral ribbon powder mixer

From practical observations, mixtures of Mg and SiO_2 powders are free flowing and do not segregate. A requirement is that shear force or high impact is not applied during the mixing stage to avoid oxidation of Mg, or premature triggering of the reduction, hence, common equipment such as high-speed impeller mixers and ball mills were not chosen. A horizontal spiral ribbon mixer was chosen, and this is suitable for processes with mixing times between 30 mins and 2 hours, with a maximum specific power requirement of 12 kW/m^3 [23]. The purchased cost was calculated based on this power requirement.

6.5.1.3. Rotary kiln furnace

The reactants have to be under an inert atmosphere during the heating stage. It was recently shown that a tumbling motion of the powders during the reduction process helped to minimise reaction mass transfer limitations, enabling better heat dissipation and a higher yield to be achieve[15]. Based on these conditions, a demand of silicon of 300 kg/batch and ease of loading and unloading such a large quantity of particulate material, an indirect-fired rotary kiln was chosen. In this type of kiln, the reactants are sealed within a cylinder and is heated from the outside, allowing the flame to be isolated from the reactants. Given the reducing atmosphere and batch operation requirements, few other furnaces are suited for the MgTR at large scale. Another important requirement is that the reactant mixture needs to be agitated to promote mass transfer processes. Conveyor-belt type furnaces which operate under a reducing atmosphere is an alternative [ref: industrial and process furnaces principles], however the powder is moved along a belt, rather than being mixed. At lower temperatures, a fluidised bed is another alternative however this type of equipment would require a large amount of reducing gas and would be uneconomical. The rotary kiln furnace can be operated in batch or continuous mode, under reducing or oxidising atmospheres, and are employed in other sectors for reduction reaction, making it a well-developed piece of equipment [ref: rotary kilns, transport phenomena and transport processes]. Data sheets obtained from a rotary kiln furnace supplier (Feeco International) indicated that a throughput of 91 kg/hr – 18 MTPH could be achieved with an indirect-fired rotary kiln, and the demand of silicon calculated here falls comfortably within these limits. The sizing factor for this piece of equipment was its maximum power output, and this was used to calculate the purchased cost of the kiln[21].

6.5.1.4. Stainless steel vessel

A glass-lined stainless-steel reactor was chosen for the dissolution step due to the requirement of aqueous HCl. The sizing factor was its volume, calculated based on the molar quantity of HCl required for a batch of a certain size, and the concentration used. The cost of the reactor based on its volume and including the impeller was estimated[22].

6.5.1.5. Plate filter

The selection criteria for filters described in[19] was used. Based on experimental observations, settling of the solids can be seen if the mixture is left unstirred for an hour, indicating that the particles are flocculated. The solids can be effectively filtered using a cellulose paper with a nominal retention of 11 µm. While the mixture is initially an opaque brown colour, the filtrate is clear. The solids exhibit a slow settling behaviour of <0.1 cm/s, and a slow filtering behaviour in the order of cm/h. These filtration characteristics indicate that a plate filter is suitable for this process. The sizing factor used for the filter was the filter area. A filter area was calculated from the quantity of solids that needed to be filtered, along with a nominated filter cake thickness of 3 cm. The cost was found using a plate filter design chart[22].

6.5.1.6. Tray dryer

Industrial drying, in principle, requires the wet powder or cake to be spread over a large surface area and hot, dry air to be passed over it. The sizing factor for a stacked, cabinet dryer was its surface area, and the cost of this equipment was calculated using the costing equation from[21].

Table 1: Summary of the design requirements and factors used to estimate the cost of the equipment. *Design requirement for the plate filter was determined from lab-scale filtration measurements.

Equipment	**Key design requirements**	**Costing factors**
Spiral ribbon powder mixer	Non-shearing, low impact	Maximum power output
Rotary kiln furnace	Reactant tumbling motion, inert atmosphere	Maximum power output
Stainless steel vessel	Corrosion resistant, agitated	Maximum volume
Plate filter	Suspended particles settling time, cake thickness*	Surface area
Tray dryer	Low technology	Surface area

6.5.1.7. Indexed capital cost and annual fixed cost

The capital cost includes the combined cost of all the major equipment selected for this process. A Lang factor was applied to estimate a delivered cost[21]. The latest available Chemical Engineering Process Cost Index (CEPCI) was applied to estimate a present-day cost (indexed capital cost). Due to the requirement of handling corrosive material, a cost factor of 4 was applied to the indexed capital cost to calculate the inside battery limit (ISBL). From this, the outside battery limit (OSBL) was estimated, and combined with ISBL to give a total capital cost. Factors accounted for under fixed costs include operator salaries, maintenance, property taxes, rent of land, plant overheads and environmental costs. These were estimated based on the total capital cost[21]. These factors add up to give the annual fixed costs.

Note that the annual fixed costs are only dependent on the capital cost of all the equipment and are not affected by process efficiencies or reaction conditions. The annual fixed cost was calculated based on a 10-year payback time at a typical 15% annual interest rate[21]. The specific fixed cost (FC) in £/kg Si was found by dividing the annual fixed cost by the annual Si production target.

6.5.1.8. Variable cost and total cost of production

The amount of energy and feedstock required to produce silicon contribute to the variable cost of the process. This cost was therefore heavily influenced by the conditions and efficiencies of the process. For the spiral powder mixer and stainless-steel vessel, typical power requirements quoted in the literature were used to estimate the total amount of energy consumed for 1 batch. For simplicity, it was assumed the plate filter separated the solids by gravity flow.

Energy is required in the ramping stage of the heating step to increase the temperature of the rotary kiln furnace and the reactants to the maximum reduction temperature (sensible heat). During both the ramp and dwell stages, heat is lost through conduction, convection and radiation. To calculate this, the surface area of the kiln was required, so a cylindrical geometry was assumed, with a typical length to diameter (L/D) ratio of 5. Therefore, the total energy required by the kiln included sensible heat, plus the heat lost during the ramp and dwell stages.

The final major equipment which contributed to the energy cost was the tray dryer. Energy is required to drive off moisture from the filter cake. The physical process occurring during the drying of the product were split into the following components: increase in temperature of the solvent (acetone) in the filter cake to its boiling point, increase in temperature of the solid to the solvent boiling point (both sensible heat), and vaporisation of the solvent at boiling point (latent heat). The total heat supplied was calculated based on a typical energy efficiency of 80%. The methods of energy consumption of each major equipment are summarised in Table 6.2.

Table 6.2: The methods of energy consumption of each major equipment are shown.

Equipment	**Method of energy consumption**
Spiral ribbon mixer	Specific power requirement
Rotary kiln furnace	Sensible heat, heat loss (conductive, convective, radiative)
Stainless-steel vessel	Specific power requirement (impeller), cooling duty
Plate filter	None, gravity flow filtration
Tray dryer	Sensible heat, latent heat

The variable cost and annual fixed cost combine to give the total cost of production (TCOP), which is quoted in this work as £/ kg Si produced. Figure 6.2 summarises the procedure for calculating annual fixed cost, variable cost and TCOP. For ease of comparison, energy, feedstock and fixed costs will be quoted as specific, normalised to the Si batch size, so their units will be £/kg Si.

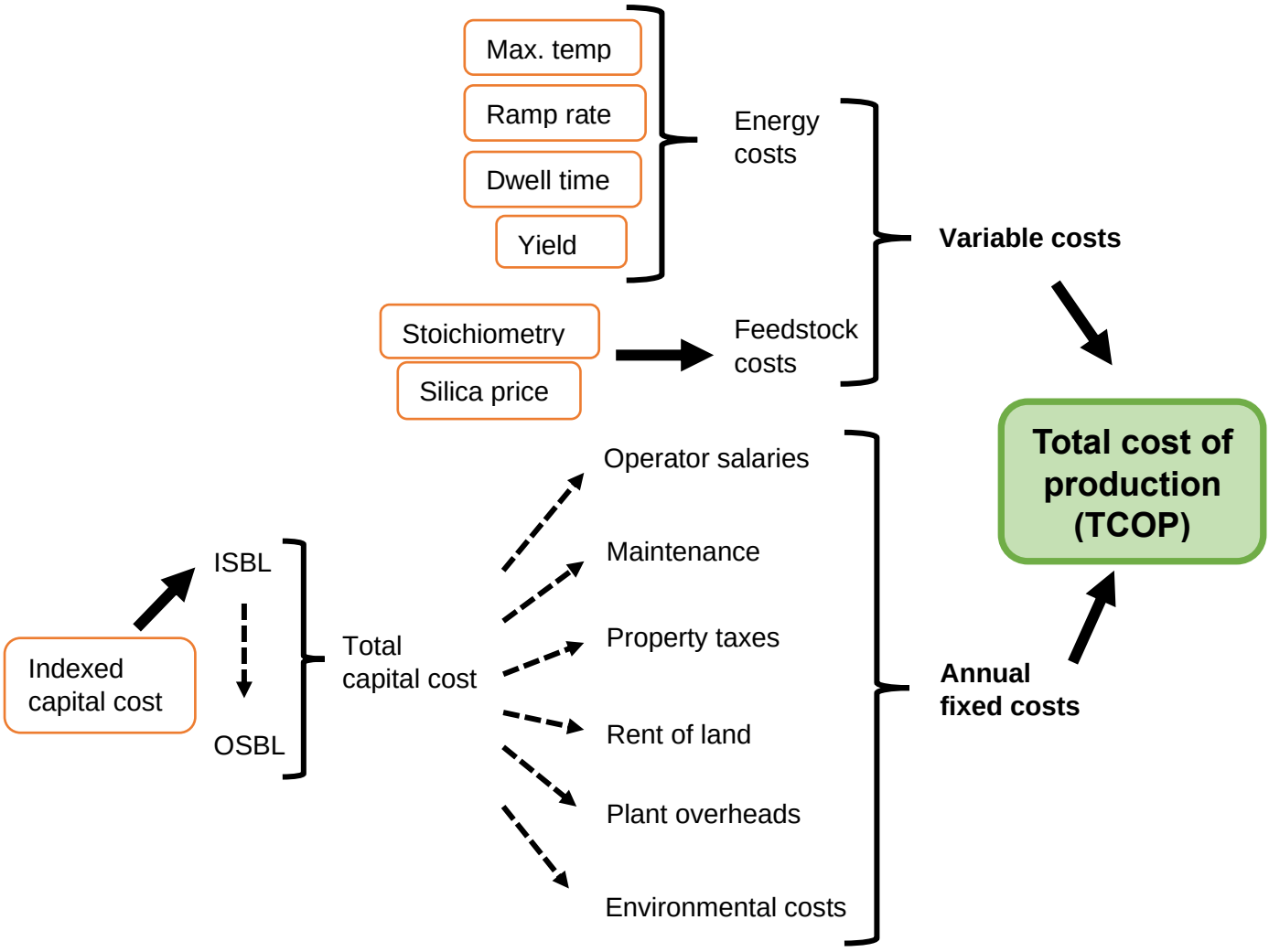

Figure 6.2: Procedure for calculating annual fixed costs, variable costs and the total cost of production. Orange boxes indicate variables which will be investigated in this study. Entities at the end of a dashed arrow were estimated as a percentage of the entity at the beginning of the arrow. Entities at the beginning of a solid arrow are combined to give entities at the end of the arrow.

6.6. Results

6.6.1. Baseline and energy costs

The baseline conditions were chosen to be 650°C maximum reduction temperature, 5°C/min ramp rate and 6-hour dwell time. These conditions are seen throughout the literature, with slight variations whereby a higher temperature of 750°C or shorter dwell time of 5 hours are used. For the baseline conditions, the energy supplied to the kiln made up 99.7% of the total energy consumed by the process in a single batch (Figure S1). In the heating step, energy was required in the dwell and ramp stages. As the reaction temperature and time are fixed, the energy consumed during the dwell stage remains constant. Figure 6.3a shows that as the ramp rate increased from 5°C/min to 20°C/min and the contribution to the total energy use from the ramp step reduces from 18% to 4%. In fact, below a ramp rate of 2°C/min, the energy required for the ramp stage dominates, while beyond this, the dwell energy takes the biggest proportion of specific energy cost. Therefore, the greatest savings can be seen by decreasing the dwell energy.

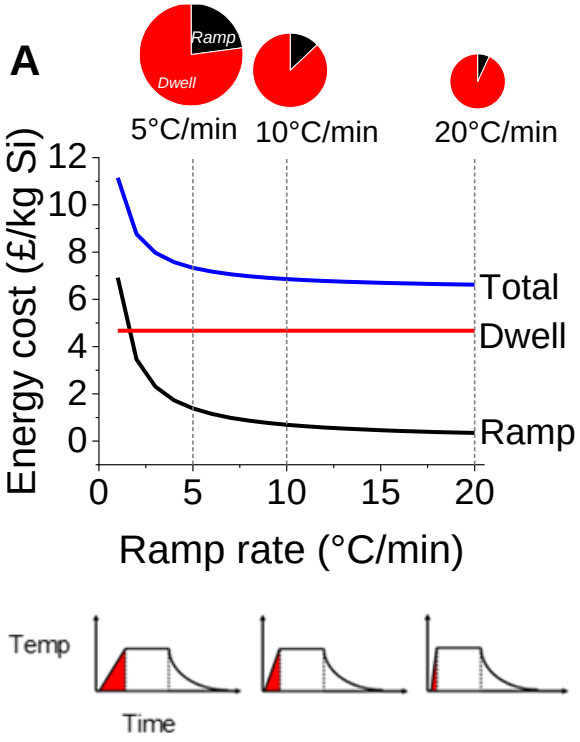

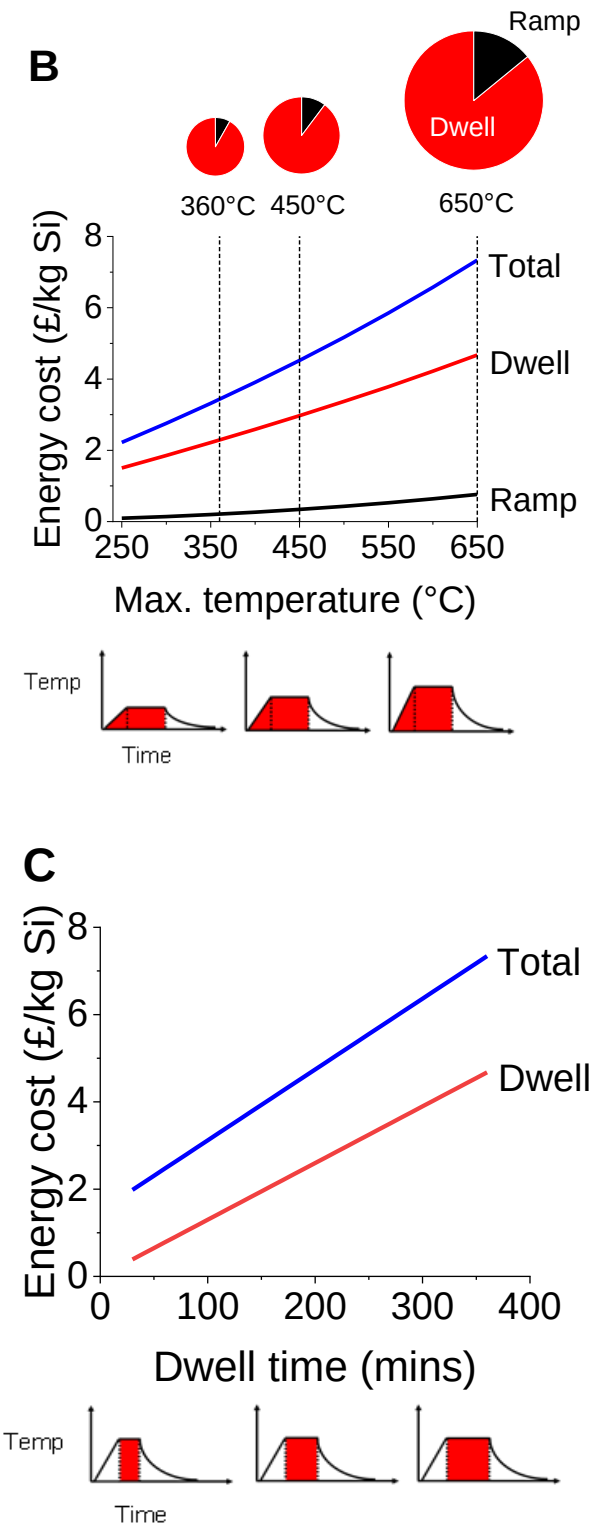

Figure 6.3: The changes in ramp, dwell and total energy cost vs a) ramp rate, and b) maximum temperature are shown. C) The dwell and total energy cost vs dwell time is shown. The baseline yield, temperature and dwell time were kept constant at 60% and 650°C and 6 hours, respectively. The pie charts show the proportions of ramp and dwell energies at different ramp rates. The time-temp graphics represent the heating profile and are to help the reader visualise the change in energy consumption with increasing ramp rates.

One way to reduce the energy consumed during the dwell step is to operate MgTR at a lower temperature. While we have recently shown that MgTR can operate at temperatures as low as 380°C[14], its impact on energy consumption is yet unknown. We therefore compared the energy costs between 250°C to the baseline 650°C (Figure 6.3b). The results show that the energy consumed during the dwell stage is between 85% to 91%, which is far greater than the contribution from the ramp stage. Therefore, changing parameters to minimise the energy consumed in the dwelling step would provide the greatest economic benefit to the process. While Figure 6.3b shows that the energy consumption during the dwell step can be reduced by performing MgTR at low temperatures, it is also likely that a similar effect is possible by reducing the dwell time. Hence, we looked at the energy savings from changing the dwell time. Figure 6.3c shows that by going from a 6-hour to a 30-minute dwell time can lower the energy consumption by up to 68%. Note that this reduction is similar to going from a dwell temperature of 650 to 250°C (Figure 6.3b).

After establishing the effects of ramp rates, operating temperature and the dwell time, we sought to create various scenarios described below by utilising experimental results from the literature and evaluate the effects of various conditions on the process economics. First, the specific energy cost of producing Si was calculated for the baseline conditions (scenario1: 650°C, 5°C/min ramp rate and 6-hour dwell time, Figure 6.4). The specific energy cost of the process was found to be £7.40/kg Si. We then varied each of the yield, ramp rate, dwell time and maximum temperature individually to create scenarios based on the conditions reported in the literature. The scenario 2 assumed 100% yield – while data on yield from the literature was inconsistent, ambiguous or not always reported, 100% yield was chosen as an optimistic value. While Figure 6.3a shows that increasing the ramp rates is beneficial for reducing the energy usage, it was shown in the literature that ramp rates higher than 10°C/min would cause excessive sintering and damage to the pores of the product silicon [24], and hence we limited the ramp rate to 10°C/min (scenario 3). As it is also reported that silicon could be formed in as little as 30 minutes[25], this formed scenario 4. Scenario 4 assumed an operating temperature of 380°C based on our previous work on the MgTR at 380°C[14]. For each of these scenarios, the total energy costs were predicted (Figure 6.4).

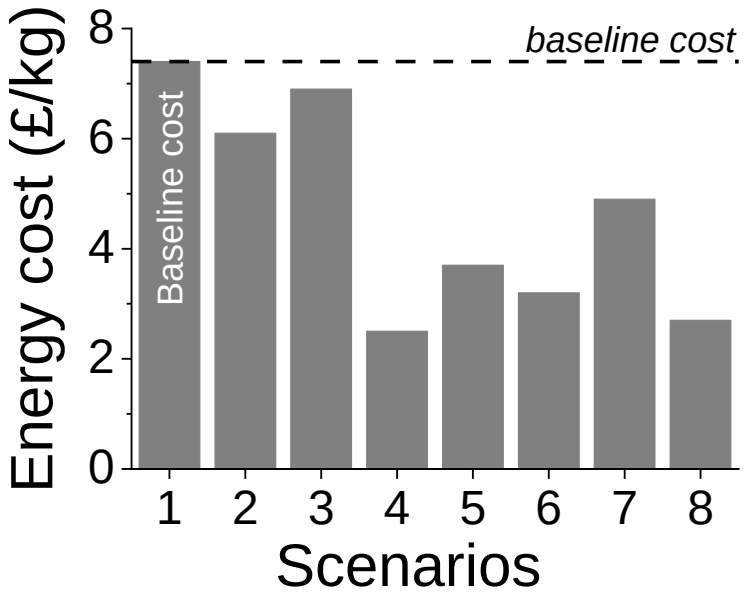

Figure 6.4: Effects of changing each condition individually on the total energy cost (scenarios 2-5), compared to the baseline energy cost (scenario 1). Scenarios 6-8 show specific energy costs between for various low-temperature cases, calculated using the experimental data. The scenarios are as follows, also see text: 1 = baseline (650°C, 6hr dwell time with a yield of 60%), 2 = yield is 100 mol%, 3 = ramp rate is 10°C/min, 4 = dwell time is 30 min, 5 = operating temperature is 380°C, 6 = 650°C and 300°C in a 2 step method with 88% yield, 7 = 380°C for 6 hrs with 80% yield, and 8 = 360°C for 3 hrs with 76% yield.

It is clear that changing maximum temperature or dwell time made the biggest difference to the specific energy cost of the process. At this point, each parameter was varied with the assumption that the yield remained the same, however in reality the yield, which is a result of the reaction kinetics and thermodynamics, is dependent on all these reaction parameters. By inputting the yield measured for various experimentally verified scenarios into the model, the specific energy costs for each scenario were calculated and compared (Figure 6.4, scenarios 6-8). In scenario 6, the conditions for the two-step method described in our previous work [13] were used. The first step was a dwell time of 30 minutes at 650°C, followed by the second step, which was a dwell time of 6 hours at 300°C, resulting in 88% yield. In scenarios 7 and 8, the conditions and yield described in[14] were used. This low temperature process was further optimised in ongoing work (manuscript in preparation), giving yields of 80% and 76% for scenario 7 and 8 respectively.

When energy costs were calculated using actual experimental data (scenarios 6-8), scenario 8 had the lowest specific energy cost, followed closely by Scenario 6. A surprising result was that scenario

6, with a maximum reduction temperature of 650°C had a lower energy cost than scenario 7, which did not exceed 380°C. This was because the majority of the dwell time (6 hours) in scenario 6 was spent at 300°C, while only 30 mins was spent at 650°C. Additionally, the yield achieved was higher in Scenario 6, which meant that less energy was consumed heating up excess reactants. These results confirm that the greatest savings in specific energy cost could be seen by lowering the dwell time, especially at higher temperatures, and the maximum temperature of the reduction. Since scenarios 6 and 8 (a 2 step method and one step method at 360°C respectively), which are based on experimental data, require low energy inputs, we investigated them further in order to identify additional improvements.

6.6.2. Feedstock costs

A wide variety of silica, waste and virgin, porous and non-porous can be used in the MgTR to produce porous silicon, highlighting its versatility. We have shown in our mechanistic study that different types of silica, when reduced at the same temperature above 650°C led to porous silicon with very different electrochemical performances[12]. From a survey of the literature, many other types of silica have been reduced and demonstrated to have high performance in lithium-ion cells[11]. However, it was noted in that review that rarely were the same set of conditions used in multiple studies. Therefore it is not possible to compare the economics of Si production from various SiO_2 feedstock. Moreover, as the productions costs and the electrochemical performance varies for Si produced from different feedstock, the costs of energy storage cannot be compared either. As such, in the section, we explore the effects of Mg cost and feedstock ratio.

Silica, Mg and HCl are the three key feedstocks required for MgTR. Amongst these three feedstocks, Mg contributed the most (63%) towards the total cost of feedstock (Figure S2). Commercially available bulk silica has a low price around £1.00/kg, with quartz sand costing considerably less, around £0.10/kg. Feedstocks such as waste glass bottles and agricultural waste would have a purchase cost lower than quartz sand, however, there would be a processing cost to remove impurities. A search of the literature reveals that the market price of Mg was between £3.20/kg to £10.00/kg (USD 4.00 to

USD 12.50/kg), depending on suppliers and agreed contracts[26]. The cost of HCl varied depending on the concentration and volume purchased. This was set at an upper bound of £1 for every kg of Mg that was used in the process.

Next, we explored the specific feedstock cost for different unit costs of Mg for various scenarios discussed above. The total amount of feedstock required was dependent on the expected yield of Si, so the costs shown in Figure 6.5a were calculated using the yield found experimentally for scenarios 1 (baseline), 6 (two-step method) and 7-8 (one step method at 380°C and 360°C respectively) discussed above. Scenario 6 had the highest yield measured, so consequently it had the lowest specific feedstock cost, followed by Scenario 7.

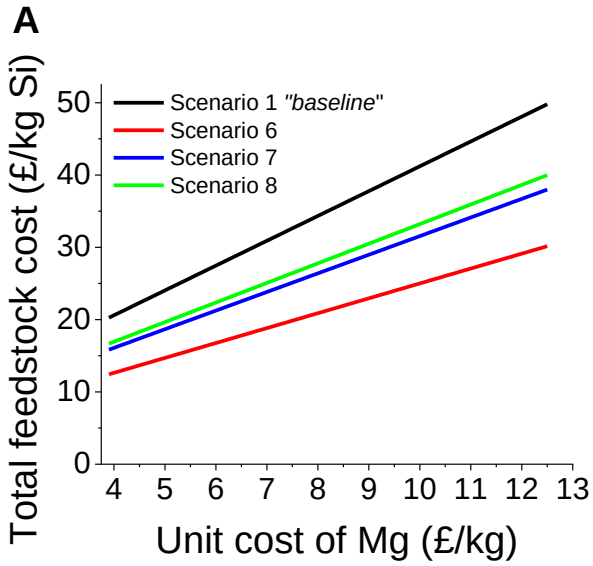

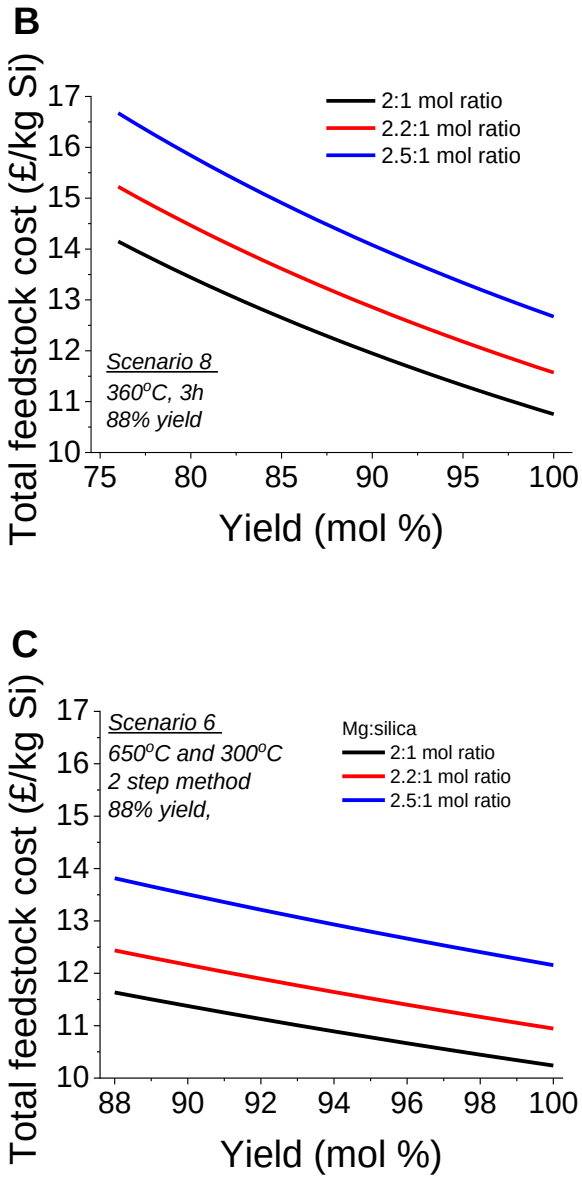

Figure 6.5: (a) The proportions of total feedstock cost of each reagent are shown. (b) The specific cost of feedstock was calculated from the unit cost of Mg[26], HCl, and SiO_2 from the literature and the yield of silicon at different conditions, measured experimentally. The effect of changing yield and mole ratio of Mg:SiO_2 on the total cost of feedstock for c) Scenario 8 and d) Scenario 6. The market price of Mg assumed here was £3.90/kg.

The yield and mole ratios are factors that can be changed by optimising the reaction. In both Scenarios 6 and 8, feedstock costs can be lowered by changing the yield and the Mg:silica molar ratios (Figure 6.5B-C). From a practical perspective, changing the mole ratio of Mg:SiO_2 is more straightforward than increasing the yield. While the results indicate that using the lowest Mg:silica ratio is beneficial, experimental results have shown that a slight excess of Mg is necessary to avoid side reactions such as the formation of Mg_2SiO_4, which can reduce the yield and quality of the product[11]. The amount of

excess Mg needed can be minimised, especially considering some of the recent developments to improve the efficiency of MgTR process, such as the rotational tube furnace method, the use of small particles, and the use of salt. An additional factor to consider is that the rate of reaction is also affected by the size of the particle size of the Mg^{27} and although this means the reaction can be sped up, the higher rate of heat release destroys the pores of the silicon, hence it lowers its quality. The cost of purchasing and handling smaller particles of Mg would also be higher. Nevertheless, it is clear that building a sound understanding of the reaction kinetics and mechanisms is essential in identifying suitable strategies to use less magnesium and improve the yield of the reaction whilst avoiding the formation of wasteful by-products.

6.6.3. Fixed cost and total cost of production

The FC of the process was estimated based on the total capital cost. To calculate the total capital cost (including delivery and installation), equipment for each unit shown in the BFD (Figure 6.1) were chosen using appropriate selection criteria, sized based on the production target of 300 kg/batch and applying a Lang factor. A Chemical Engineering Process Cost Index (CEPCI) was applied to the capital cost to calculate the indexed capital cost for 2021. In order to investigate the effect of scale on the cost of the process, this calculation was repeated for a range of plant capacities, up to 1500 kg/batch and the results are shown in Figure 6.6A. The largest contributor to the capital cost was the stainless-steel vessel required for removing all Mg-species (unreacted Mg, oxide and silicide) via dissolution in HCl. This high cost come from (i) the need for a glass-lined stainless-steel vessel due to the corrosive nature of HCl, and (ii) the high volume of HCl required.

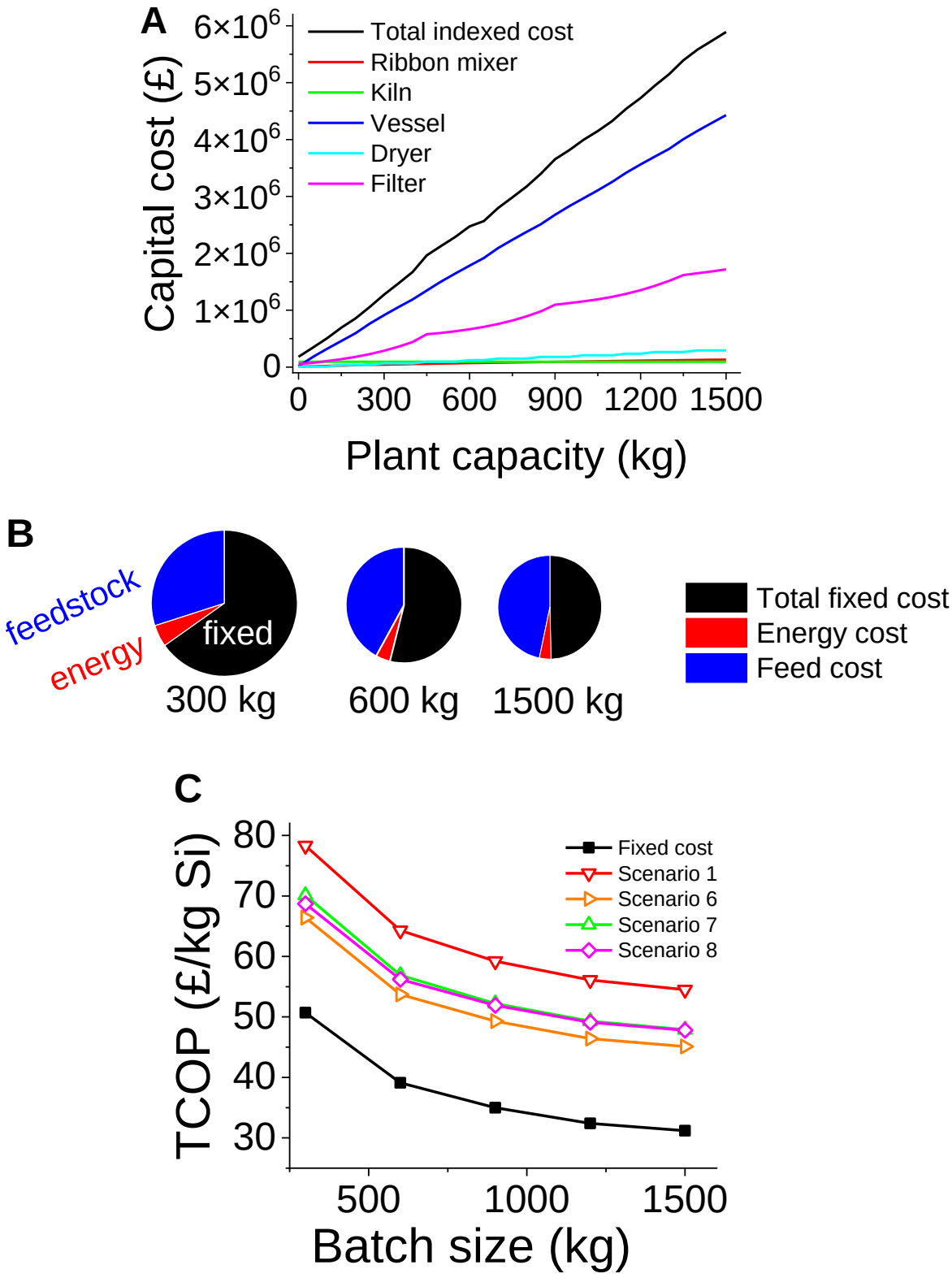

Figure 6.6: A) Indexed capital cost of the MgTR in a batch process, at different capacities. The individual equipment costs at each capacity were combined to give the purchased cost. B) The pie charts show the proportion of energy, feed and fixed costs at different scales for a 380°C reduction temperature (Scenario 7). The sizes of the pie charts represent the relative total variable cost. C) The TCOP for scenarios 1, 6, 7 and 8 are shown for batch sizes between 300 and 1500 kg. Fixed cost included for reference and is the same for all scenarios.

FC accounts for the costs of running the plant, including operator salaries, waste removal and maintenance. Each component of FC was calculated as a percentage of the indexed capital cost. Variable costs (VC) which included energy and feedstock costs were added to FC to give the TCOP. The proportions of fixed, energy and feedstock costs change at different scales, and are shown in Figure 6.6B for 300, 900 and 1500 kg scales at 650°C. At 300 kg scale, majority of the cost comes from FC. The specific energy cost accounts for the smallest proportion of the total cost. Though the TCOP decreased at larger scales, the proportions of each cost changed by different amounts. As shown in Figure 6.6B, at 300 kg scale the biggest proportion of the cost came from FC, however at 1500 kg scale, FC was comparable to feedstock cost. FC is dependent on the capital cost of equipment hence equipment sizing will have an effect, and it is not affected by changes in process conditions and efficiencies that occur during daily operations. In practice, the cost of feedstock would also decrease from bulk buying however, the savings uncertain as it is dependent on supplier and economic climate. The specific energy cost also decreased at larger scales due to relatively lower heat losses from the kiln.

The TCOP of Si made under various scenarios at different scales are shown in Figure 6.6C. For each scenario and batch size, the VC was added to the FC to give the TCOP. The price of Mg and SiO_2 used was £3.90/kg and £1.00/kg respectively. In the baseline scenario (1), the TCOP at 300 kg was £79/kg Si, the highest of all the scenarios. This is still far lower than the current market price of SiO active material (£160/kg) [28]. Scenario 6 was found to be the cheapest at all batch sizes due to lower VC. The lowest energy cost was calculated in this scenario, and the lower Mg:SiO_2 ratio used in the feedstock meant that less Mg was required to produce Si. Scenario 7 and 8 represented the low temperature process and were both similar in operating conditions and yield of Si and hence had similar TCOP. The TCOP of the MgTR is therefore competitive, even at 300 kg/batch scale. For scenario 6 and 8, the lowest TCOP that could be achieved was £46 /kg Si and £48 /kg Si.

To make a fair comparison of Si to the presently used anode material graphite, the cost of energy storage (pence/Ah capacity) was calculated using experimental data. Figure 6.7 shows the capacity

cost for Si produced from MgTR at temperatures between 350°C and 650°C. Data used in these calculations are shown in Table S1. For the capacity cost calculations, the stable capacities achieved after 100 cycles were used.

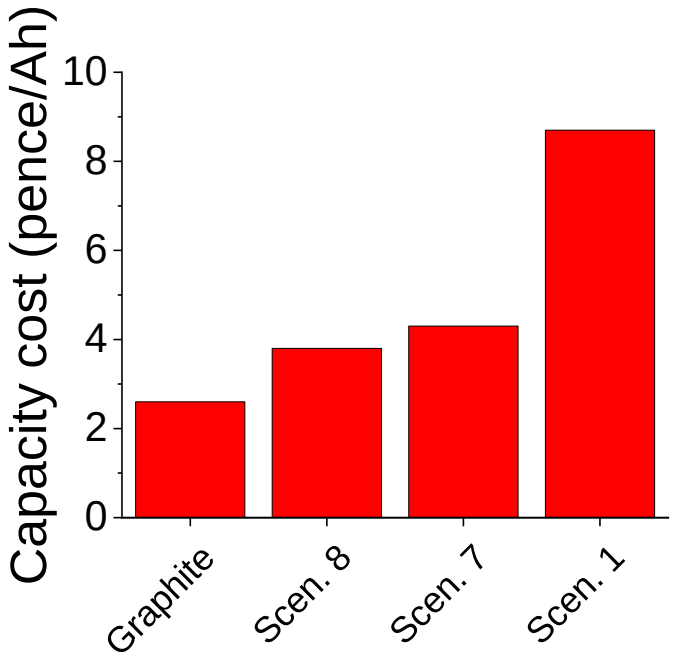

Figure 6.7: 100th cycle capacity cost of silicon made at different temperatures are shown in comparison to the graphite market price.

The energy density of the anode in kWh/kg is dependent on the voltage, and the configuration of the constructed cell. These can vary with application so to compare silicon to graphite, the chosen unit for capacity cost was pence/Ah. Graphite at a market price of £10/kg and a capacity of 372 mAh/g was still 28% cheaper than Si (2.75 vs 3.8 pence/Ah) in the best case scenario of 360°C. Graphite is a mature technology hence it benefits from cost savings associated with large scale manufacturing. It also means that there is little scope for improvement of this technology. The higher cost of Si comes with the benefit of being able to make incremental and large improvements to the capacity of current cell technology, as it can be added to graphite electrodes in varying amounts. Due to the stoichiometry, greater gravimetric energy density can be achieved with silicon, more than can be achieved with graphite. While the increase in the amount of silicon used in a cell would increase the specific capacity of the cell, the increase in overall energy density would depend again on the

application. In larger applications such as electric vehicles where the weight of the battery pack comes mostly from the casing, the increase in energy density seen by replacing the anode with silicon (even at 100%) would be minimal. This is taking into account that a typical EV with an average of 67 kWh energy density has 25 kg of graphite (total pack weight in a car is ~500kg), and that increasing the capacity of the anode alone beyond a threshold value of 1000 mAh/g will yield no additional benefit to the overall capacity of the cell. Silicon is required to achieve a higher capacity in a way that graphite cannot, hence there is a functionality benefit to the higher cost of silicon. Given the feedstock flexibility of the MgTR, and the overall ease of operation (requires only non-specialised conditions and equipment) this process has the potential to be adopted throughout the world, giving adopters supply chain independence, and to some degree, resilience to external economic factors. Under certain economic conditions where there is a short supply of anode-grade graphite and high demand, the market may see a lower cost of silicon than graphite due to the MgTR's feedstock flexibility and ease of operation advantages.

The Si with the lowest capacity cost was made from Scenario 8, and this had a corresponding 100th cycle capacity of 1000 mAh/g. It is clear that there is plenty of room for improvement, as the initial capacity was much higher, and the high surface area resulted in poor first cycle efficiency and degradation over 100 cycles. In order to improve its overall performance, a deeper understanding of the low-temperature kinetics and pore formation mechanism of the MgTR is required. This would enable the fine tuning of the reaction conditions to produce Si with better properties while still operating economically and efficiently.

6.6.4. Improving and optimising the MgTR

6.6.4.1. One-step process

It is possible to carry out the reduction at 360°C using the one-step process and achieve a yield of 76% (scenario 8 above), with the lowest energy costs. In order to explore ways to lower energy costs further, the effects of the ramp rate, dwell time, maximum temperature and yield for scenario 8 were considered. The ramp rate had little effect on the total energy cost for any given temperature (Figure

6.8A), which is consistent with the findings shown in in Figure 6.3 that the energy consumed during the ramp stage only made up a small proportion of the total energy consumed. For any ramp rate considered, it is clear that by lowering the temperature from 360°C to 200°C reduces the energy costs linearly from ~£2.60/kg Si to ~£1.20/kg Si. Next, the effect of varying the dwell time between 0.5h to 3h was considered over a temperature range of 200-360°C.

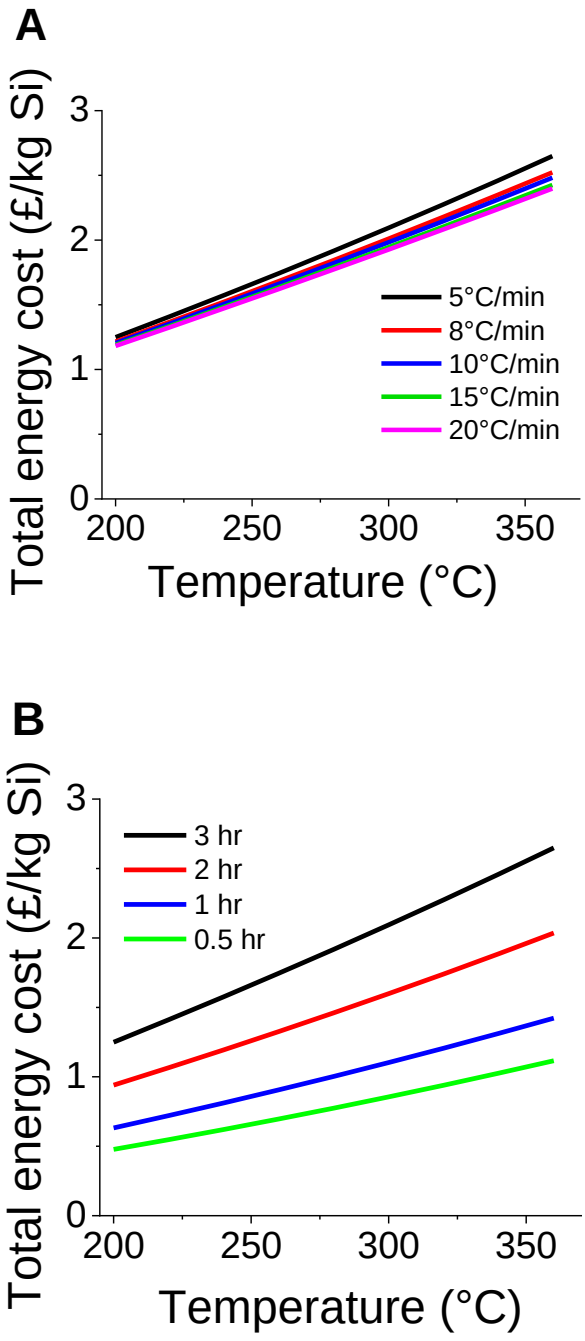

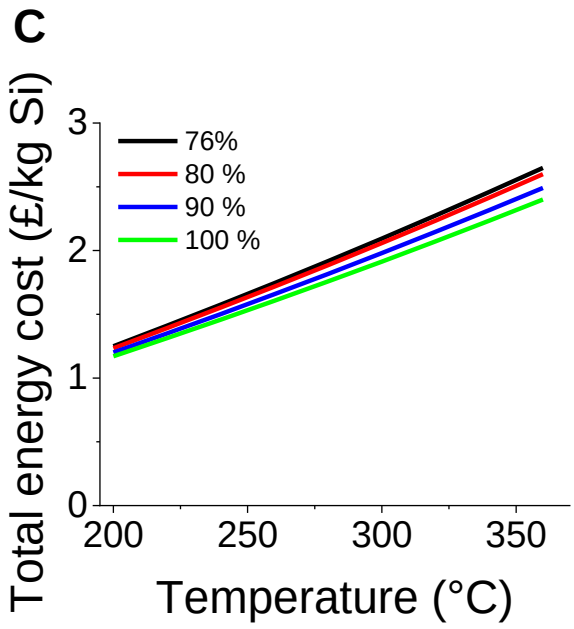

Figure 6.8: Effect of changing the A) ramp rate, B) dwell time and C) yield at different temperatures on the total energy cost of the process.

It can be seen in Figure 6.8B that decreasing the dwell time at a given temperature would make it possible to achieve much lower specific energy costs. Interestingly, changing both the temperature by 100°C (from 360°C) and dwell time from 3h to 1h can reduce the energy costs from ~£2.6/kg Si to ~£0.9/kg Si, thus showing a significant improvement – something that is worth exploring experimentally. Lastly, maximising the yield from the experimentally reported 76% to a hypothetical 100% would result in little energy savings at a given temperature (Figure 6.8C). This is most likely due to the fact that an already high yield has been achieved experimentally. It is important to note that the predictions shown here are for hypothetical situations with the purpose of indicating the best way to lower total energy costs. Realising these situations would require further experiments in the future, beginning with a study on the dwell time and strategies to lower temperature requirements.

6.6.4.2. Two-step process

Upon inspection of the relative contributions to the total energy consumption of the two-step process, it was clear that the second dwell step made up the greatest proportion (70%) of the total energy consumption (Figure 6.9A).

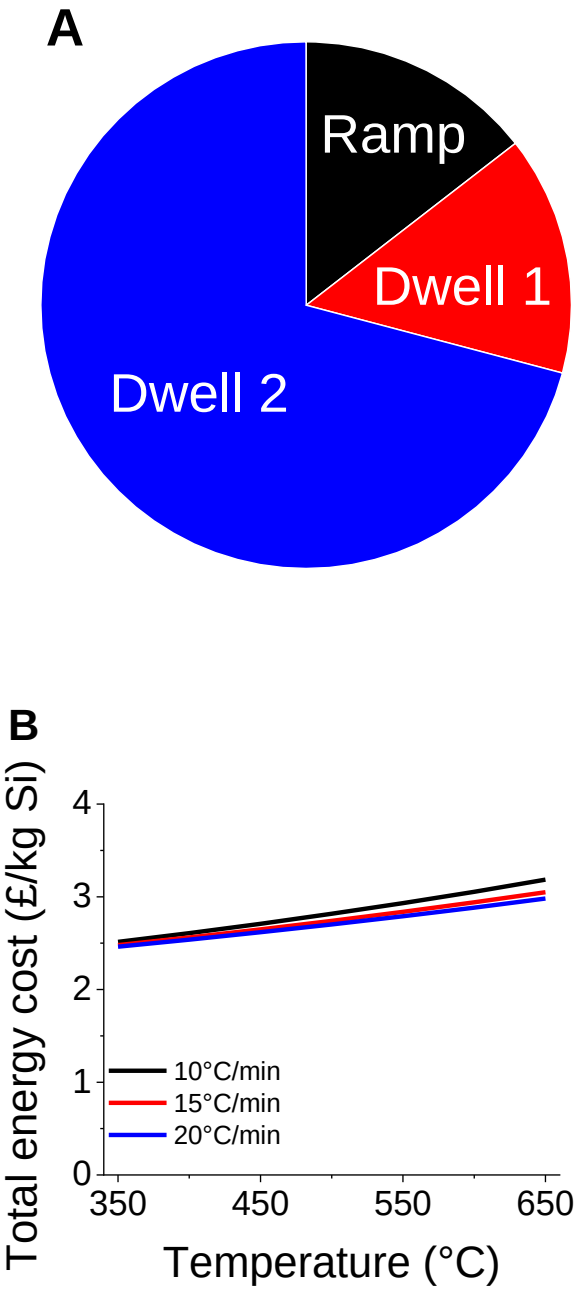

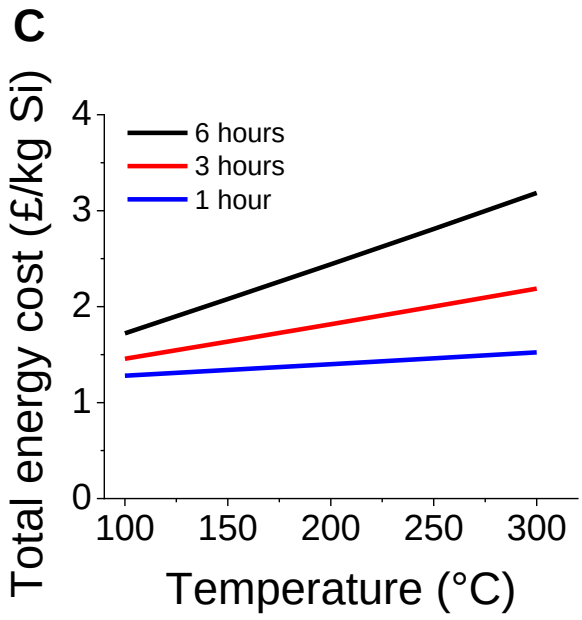

Figure 6.9: A) Proportion of energy costs for two-step reduction method. Effect on energy required of changing B) the ramp rate at different first step temperatures and C) the dwell time for the second step at different temperatures.

The ramp and first dwell stages consumed almost equal amounts of energy. Increasing the ramp rate and decreasing the first dwell temperature, as shown in Figure 6.9A, provides little potential for cost savings. Going from 650°C to 350°C, using a ramp rate of 10°C/min only lowers the total energy cost from £3.00 to £2.50/kg Si, a savings of only 17%. At 350°C the decrease in energy cost going up to 20°C/min is negligible, given that a high ramp rate of 10°C/min was already being used for the two-step method (Figure 6.9B). Decreasing the second step dwell time from 6 hours to 3 hours at 300°C had the potential to cut energy cost by 32%, and by more than 50% if the dwell time was dropped to 1 hour (Figure 6.9C). Similar to the one step method considered above, a high yield of 88% obtained for the two-step method means that negligible improvements in the energy cost would be gained by increasing the yield further (data not shown). As such, for the two-step method, these results provide support to undertake future work on decreasing the dwell time of the second step.

6.6.4.3. Fixed cost

The equipment with the highest indexed cost was the stainless-steel vessel so decreasing this would make the biggest impact on the FC. For a fixed batch size, a fixed number of moles of HCl would be required, and the volume can be calculated for a chosen concentration. 1M concentration is typically used and this corresponds to a high fixed cost of £51 /kg Si at 300 kg/batch. The effect of using more concentrated HCl, hence needing smaller vessels was investigated next. It is assumed that this change in HCl concentration does not affect the choice of material used for the vessel (glass-lined stainless-steel). It can be seen from Figure 6.10 that as the concentration increased, the total volume required decreased and so does the capital cost since the vessel size reduced. Therefore, the FC also decreased, and the greatest drop in FC was seen when the concentration was increased from 1 to 3M. At this point, the cost of the vessel became comparable to the other equipment (calculation not shown) and hence further savings diminished even when using more concentrated HCl.

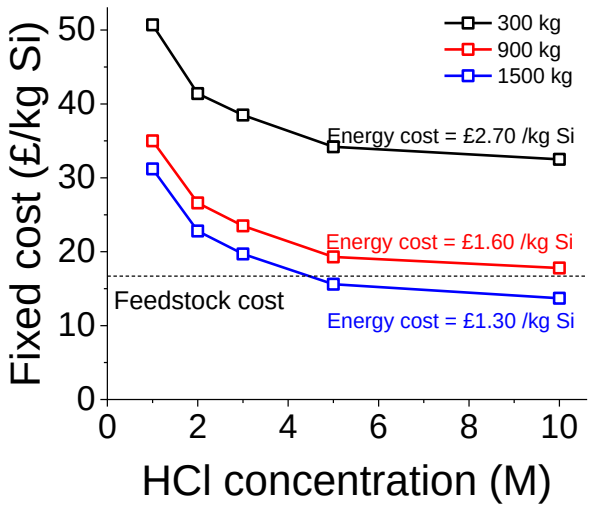

Figure 6.10: Fixed costs for different HCl concentrations are shown for 300, 900 and 1500 kg/batch scales Energy and feedstock costs are for Scenario 8.

The volume and number of reactors that are used can be further minimised by considering a continuous etching process using a PFR whereby a much smaller volume could be used by controlling

the residence time of the reactants. Reactor modelling calculations based on experimentally obtained dissolution kinetic data would be needed to ensure suitable dimensions and flowrates are chosen.

6.7. Conclusions

The TCOP of silicon via the MgTR is cheaper than the current market price of anode grade SiO. To be competitive with the market price of graphite, both variable and fixed costs have to be lowered. However comparing the TCOP of Si made by the MgTR to that of polycrystalline Si and graphite is an unfair comparison, since the properties of each of these materials are completely different.

Feedstock accounted for 46% of TCOP. The flexibility of SiO_2 feedstock allows the MgTR to benefit from supply chain independence. The feedstock costs can be lowered by replacing an expensive feedstock for a cheaper one or improving the yield. The properties of each type SiO_2 are very different, therefore changing one feedstock for another will result in different reaction kinetics, yield, and product quality. Therefore, exchanging SiO_2 feedstocks and improving yield require an understanding of the reaction kinetics.

At the largest scale considered in this study, fixed cost accounted for 50% of TCOP. This was due to the high volume, and therefore high capital cost of the stainless-steel dissolution vessel. By increasing the concentration of HCl from 1M to 3M, fixed cost was decreased by 36%.

Energy costs accounted for 14% of TCOP, at the largest scale, using either the two-step reduction method or 360°C method. Using either of these methods instead of the baseline brought the energy cost down by 60%. Further improvements are of course, still possible, and has the potential to lower energy costs by a further 20%, however, the yield and properties of the Si are intimately connected to the reduction conditions. Therefore, a MgTR ‘toolkit’ would prove invaluable in effectively changing the conditions to improve process economics and maintain feedstock flexibility without sacrifice to produce yield and quality. The effect of changing certain conditions have been laid out in this paper and supported as much as possible by experimental data. To have the greatest impact on the economics of the process these changes should be put to practice, beginning with minimising the

costliest step. To effectively put these changes into practice, further experimental investigation is needed, and this can be carried out in different ways. A study of different combinations of conditions will result in a high-resolution data set but requires large amounts of experiments and repeats. An understanding of the kinetics of the reaction would enable us to predict the required conditions for a range of feedstocks.

6.8. Acknowledgements

The authors thank EPSRC (EP/L016818/1, EP/P006892/1 and EP/R025983/1) and Energy Storage CDT for funding this research. M.Y. thanks Mitacs and UKRI for funding through the Globalink Doctoral Exchange Award. Dr Jude Ejeh and Dr. Jake Entwistle are thanked for helpful discussions.

6.9. References

1 Faraday Report Annual Gigafactory Study, *UK electric vehicle and battery production potential to 2040*, 2020.

2 Nissan Leaf Specifications, https://www.nissan.co.uk/vehicles/new-vehicles/leaf.html#C400_cmp_story_839a-modal, (accessed May 22, 2022).

3 Samm Gillard, 2021.

4 European Technology and Innovation Platform, *Batteries Europe Strategic Research Agenda*, 2020.

5 D. W. Olson, R. L. Virta, M. Mahdavi, E. S. Sangine and S. M. Fortier, *Geological Society of America*, 2016, **520**, 66–67.

6 M. N. Obrovac, L. Christensen, D. B. Le and J. R. Dahn, *Journal of The Electrochemical Society*, 2007, **154**, A849–A855.

7 D. H. Filsinger and D. B. Bourrie, *Journal of the American Ceramic Society*, 1990, **73**, 1726–1732.

8 D. Losic and A. Santos, *Electrochemically engineered nanoporous materials*, 2015.

9 Z. Bao, M. R. Weatherspoon, S. Shian, Y. Cai, P. D. Graham, S. M. Allan, G. Ahmad, M. B. Dickerson, B. C. Church, Z. Kang, H. W. Abernathy, C. J. Summers, M. Liu and K. H. Sandhage, *Nature*, 2007, **446**, 172–175.

10 D. Cho, M. Kim, J. Hwang, J. H. Park, Y. L. Joo and Y. Jeong, *Nanoscale Research Letters*, 2015, **10**, 1–8.

11 J. Entwistle, A. Rennie and S. Patwardhan, *Journal of Materials Chemistry A*, 2018, **6**, 18344–18356.

12 J. E. Entwistle, G. Beaucage and S. v. Patwardhan, *Journal of Materials Chemistry A*, 2020, **8**, 4938–4949.

13 S. A. Martell, Y. Lai, E. Traver, J. MacInnis, D. D. Richards, S. MacQuarrie and M. Dasog, *ACS Applied Nano Materials*, 2019, **2**, 5713–5719.

14 M. Yan and S. v. Patwardhan, *RSC Advances*, 2021, **11**, 35182–35186.

15 N. Yoon, C. Young, D. H. Kang, H. Park and J. K. Lee, *Electrochimica Acta*, 2021, **391**, 138967.

16 Z. Favors, W. Wang, H. H. Bay, Z. Mutlu, K. Ahmed, C. Liu, M. Ozkan and C. S. Ozkan, *Scientific Reports*, 2014, **4**, 5623.

17 C. Li, C. Liu, W. Wang, Z. Mutlu, J. Bell, K. Ahmed, R. Ye, M. Ozkan and C. S. Ozkan, *Scientific Reports*, 2017, **7**, 1–11.

18 J. Ryu, D. Hong, S. Choi and S. Park, *ACS Nano*, 2016, **10**, 2843–2851.

19 D. W. Green and M. Z. Southard, *Perry's Chemical Engineers' Handbook*, McGraw-Hill Education, New York, Ninth Edit., 2019.

20 J. R. Couper, W. R. Penney, J. R. Fair and S. M. Walas, *Chemical Process Equipment: Selection and Design*, Elsevier, Oxford, Third Edit., 2012.

21 R. K. Sinnott and G. Towler, *Chemical Engineering Design*, Elsevier Ltd, Oxford, Fifth Edit., 2009.

22 M. Peters and K. D. Timmerhaus, *Plant Design and Economics for Chemical Engineers*, McGraw-Hill, Inc, Singapore, Fourth Edi., 1991.

23 E. Paul, V. A. Atiemo-Obeng and S. M. Kresta, *Handbook of Industrial Mixing: Science and Practice*, John Wiley & Sons Ltd, New Jersey, 2004.

24 N. Liu, K. Huo, M. T. McDowell, J. Zhao and Y. Cui, *Scientific Reports*, 2013, **3**, 1–7.

25 D. Cho, M. Kim, J. Hwang, J. H. Park, Y. L. Joo and Y. Jeong, *Nanoscale Research Letters*, 2015, **10**, 1–8.

26 E. L. Bray and S. DeLoach-Overton, *USGS Mineral Industry Surveys*, 2021.

27 Z. Yang, Y. Du, G. Hou, Y. Ouyang, F. Ding and F. Yuan, *Electrochimica Acta*, 2020, **329**, 135141.

28 Xiamen TOB New Energy Technology Co., Ltd., https://www.tobmachine.com/lithium-ion-battery-carbon-coated-silicon-as-si-anode-material_p917.html, (accessed June 10, 2022).

7. Conclusions and outlook

7.1. Conclusions

The increase in demand for porous silicon due to the growth of the lithium-ion battery market has prompted the work presented in this thesis. The carbothermal reduction is a suitable, well-established process for producing electronic grade silicon where high-purity wafers are required. Electronic grade silicon is not suitable as an anode material for lithium-ion batteries, and therefore the huge amounts of energy required by the carbothermal process is not warranted.

The magnesiothermic reduction is the most promising replacement for the carbothermal reduction, as it operates at ~650°C and produces porous silicon as opposed to a dense ingot. This process was studied in this thesis, in particular, the economics of the process, as well as strategies to improve the process in favour of the economics.

Prior to the studies in this thesis, it was generally accepted that the onset of reduction could be seen at 450°C, giving a poor yield (<10%), and that the yield increased when higher temperatures were used. The reduction is most often carried out at a minimum of 650°C which is the melting point of Mg. At and above this temperature the reaction could proceed to give an appreciable yield. The work presented in Chapter 4 of this thesis demonstrated for the first time the dependence of reaction onset temperature on particle size of the silica. A cut-off exists at 20 nm, whereby particles smaller than this would not undergo a reduction at 450°C. 20 nm particles could be reduced by Mg at 450°C, producing a yield of 35 mol% while 7 nm fumed silica could be reduced at 380°C, producing a yield of Si of 60 mol%. The latter yield was comparable to that achieved at 650°C.

By taking advantage of the high reactivity of smaller particles, larger particles could be triggered to reduce at 380°C by addition of fumed silica as seen in Chapter 5 of this thesis. This triggering effect occurred not only in non-porous Stöber particles, but also in Syloid, a commercial porous silica. It was found that at mixture containing 25% fumed silica and 75% Syloid could be reduced at 380°C, giving

a yield of 80 mol%. Poor electrochemical performance was seen in Syloid reduced at 650°C, whereby its specific capacity faded by 75% after 100 cycles and its 100th cycle capacity was 300 mAh/g. However when reduced as a mixture with fumed silica at 380°C, the capacity fade after 100 cycles was only 53%, and its 100th cycle capacity was a staggering 860 mAh/g. By exploiting the triggering effect, silica which would otherwise produce silicon with poor performance could be converted into silicon with superior performance and at much lower temperatures. Given that the reduction has not previously been reported to proceed at such low temperatures, little is understood about the mechanisms of the reaction. A curious trend is the increase in yield when the reduction temperature was lowered from 450 to 380°C. This indicates closely competing reaction kinetics, and different reactions are favoured at different temperatures within this range. If the low temperature reduction method were to be considered for scale-up, future work should focus on building an understanding of the kinetics and mechanisms between 380 and 450°C.

From a process economics perspective, lowering the reduction temperature, decreasing dwell time and increasing the ramp rate decreases energy costs. It was shown in Chapter 6 that lowering the temperature from 650°C to 360°C or using the two-step method decreases energy costs by 63 and 57% respectively, compared to the baseline method. At the largest scale considered in this study (1500 kg/batch), the total cost of production of the the one-step (360C) and two-step methods were £47.8 and £45.1 /kg Si respectively. The greatest impact could be made by lowering the fixed costs, which accounted for 50% (£31.5 /kg Si) of the total cost of production at this scale. This can be done by minimising the volume of HCl, and therefore the reactor size and cost, by using higher concentrations (≥3M). The fixed costs could be lowered by 36% going from 1M to 3M. It is likely that the pore properties and performance of the Si would be unaffected by etching in higher concentrations, and a small, well-designed study could confirm this. A continuous dissolution step would also help with lowering the capital cost, as this would allow the reactor size, and therefore the capital cost to be minimised. Although energy costs account for the lowest portion, heat recovery would reduce energy consumption even further by reusing the heat that is rejected during the cooling step of the process. The biggest impact to energy cost could be made by lowering the dwell time of

the one-step process and lowering the dwell time of the second step in the two-step process. Feedstock costs at the largest scale accounted for 47% of the total cost of production. Using a lower Mg:SiO_2 mole ratio would decrease the feedstock cost since Mg was the most expensive feedstock.

7.2. Outlook

A number of changes could be made to the process parameters in favour of process economics however it is important to remember that a tension exists between the different heating steps, the yield, and the properties of the resulting silicon. From existing studies, it is possible to predict how each of the dwell time, ramp rate and reduction temperature affect the pore properties, and to a lesser extent, the yield. However, it is impossible to predict the result of changing a combination of these conditions. Therefore a 'black box' still exists in our understanding and to remove it would allow us to efficiently tune and optimise the reaction without performing large amounts of iterative experiments. For example, it is well known that higher ramp rates encourage sintering, due to rapid heat build-up and insufficient dissipation. This heat build-up is a result of rapid external heat input, causing the reaction to proceed at high rates, releasing even more heat due to its exothermic nature. This might mean that a lower dwell time could be used, or even a lower temperature. Investigating a combination of just 3 different ramp rates for each of 3 different temperatures and 3 different dwell times to find a trend would require a minimum of 27 reductions. This number quickly multiplies to over 100 reductions when investigating the effect of adding salts or performing repeats. Yet, even with a dataset this large, it would still be difficult to then 'translate' these results to other types of silica, given the wide variety of existing types.

The MgTR has been studied heavily since it was first reported in 2007, and a range of reduction conditions and silica feedstocks have been used. High yields and specific capacities have been reported in many studies however rarely were the same set of conditions and feedstocks used in multiple studies. This indicates from a materials chemistry perspective that there may not be a single type of silica which possesses a specific set of properties ideal for the MgTR to proceed and produce

high performing silicon. Rather it indicates that silica with different properties require different conditions to be converted into high performing silicon.

Throughout the temperatures considered here, the SiO_2 remains a solid, which means that that the reaction is mass transfer limited. Thus, feedstocks with different structural properties will undergo the reduction via different mechanisms and kinetics. Reaction kinetics are dependent on the reaction conditions, so a set of conditions which works for one type of feedstock may not for another. Being able to map the different kinetics and mechanisms to feedstock properties is the first step in determining the optimum conditions for any given silica type.

The choice of feedstock depends on its price and availability, both of which are affected by geopolitical factors. It follows that, economically, there may not be an 'ideal' silica, since silica that is available in great abundance today may become severely affected by supply chain issues tomorrow, causing its price to soar. If the same set of product properties could be achieved with different types of silica simply by changing the reduction conditions, then the choice of silica could be made based solely on its market price. This would ensure that the MgTR remains feedstock versatile and supply chain independent.

An ideal strategy would describe the best combination of reduction conditions to exploit reaction kinetics and thermodynamics, along with the correct particle sizes to use to have better control of reactant distribution and homogeneity whilst still maintaining a low $Mg:SiO_2$ ratio.

Understanding the kinetics and mechanisms would enable a MgTR 'toolkit' to be built, whereby the exact conditions can be stated to convert a given silica feedstock into silicon with a set of desired properties. It may then be possible to improve the yield and product quality while decreasing energy costs or at least, have a meaningful discussion, with quantitative proof, on whether sacrificing one metric while favouring another would improve the overall economics of the process. By painting a complete picture of what is happening at every step of the reaction from a kinetic study, it will be possible to make the changes to the process for economic benefit, without the need for large amounts of experiments.

8. Appendix

8.1. Chapter 4 Supporting information

Electronic Supplementary Information

Exploiting nanoscale effects enables ultra-low temperature to produce porous silicon

*Maximilian Yan and Siddharth V. Patwardhan**

Department of Chemical and Biological Engineering, Green Nanomaterials Research Group, The University of Sheffield, Mappin Street, Sheffield S1 3JD, UK. *s.patwardhan@sheffield.ac.uk

Table S1: Concentration of NH_3 used in Stöber silica synthesis and the resulting silica particle sizes measured by TEM.

[NH_3] (M)	Particle diameter (nm)	Internal specific surface area (m^2/g)
0.01	20 ± 2	45
0.05	75 ± 8	9
1.13	500 ± 17	6

Table S2: Properties of silica and their reduction products at different temperatures are summarised.

Sample	**Silicon Yield (mol%)**	**Specific surface area (m^2/g)**[a]	**Total pore volume (cm^3/g)**
S20	n/a *	189	0.79
S500	n/a *	7	0.01
S20 450°C	35	184	0.24
S20 650°C	56	92	0.19
S500 650°C	50	179	0.29
F7	n/a *	424	0.7
F7 380°C	58	70	0.16
F7 450°C	31	177	0.47

[a] This is total surface area (internal and external).
* This is the feedstock silica samples which has not undergone reduction and hence a yield of silicon is not applicable.

Table S3: Crystal planes identified in Figure S4 and associated d-spacings, 2θ angles and miller indices.

d-spacing (nm)	**2θ (degrees)**	**Miller Indices**
0.32	28	(111)
0.20	48	(220)
0.17	56	(311)
0.14	76	(331)

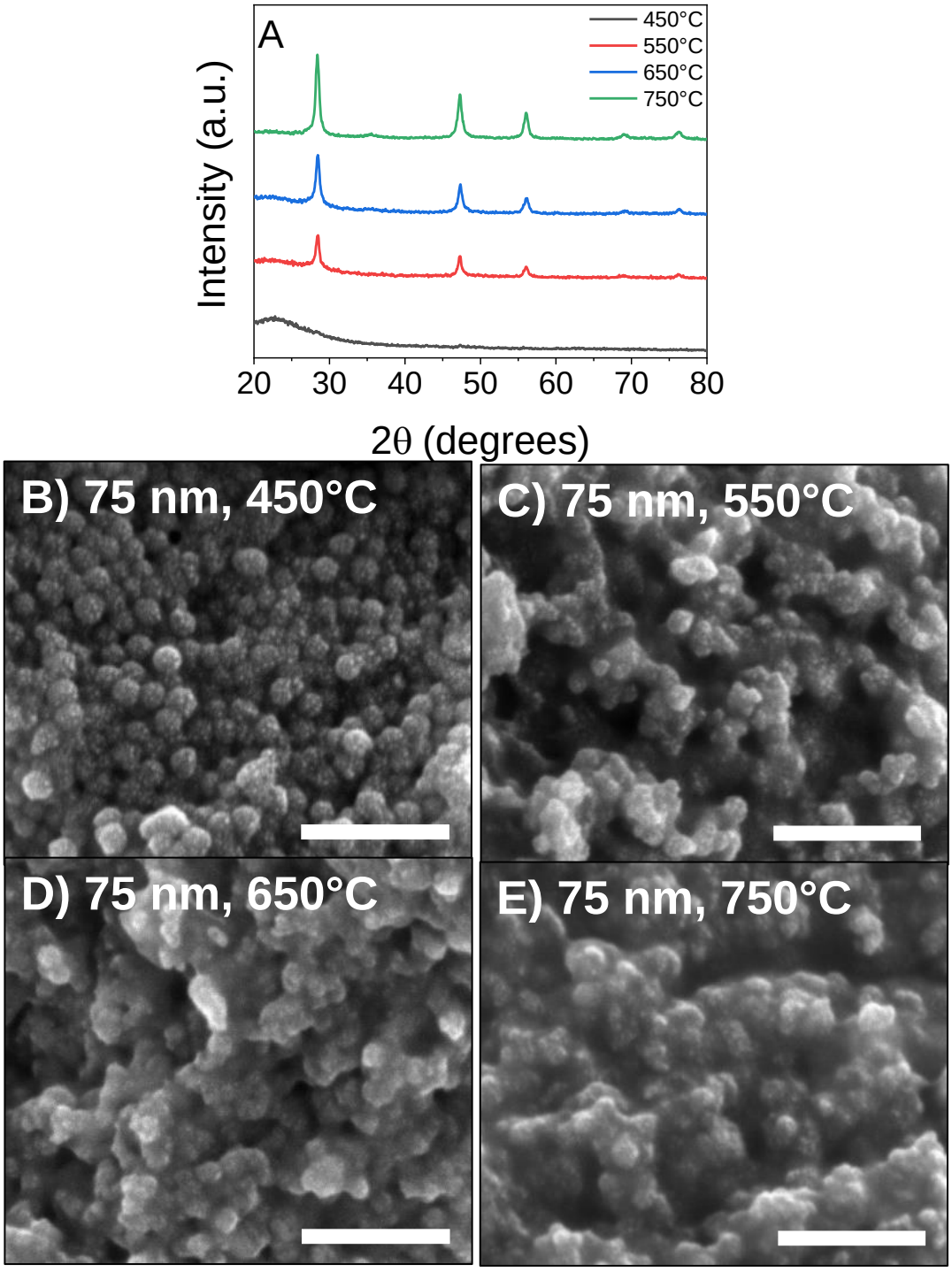

Figure S1: (A) XRD and (B-E) SEM images of 75 nm particles (S75) reduced at different temperatures. Scale bars of SEM images are 500 nm. All data was collected on samples after HCl etching.

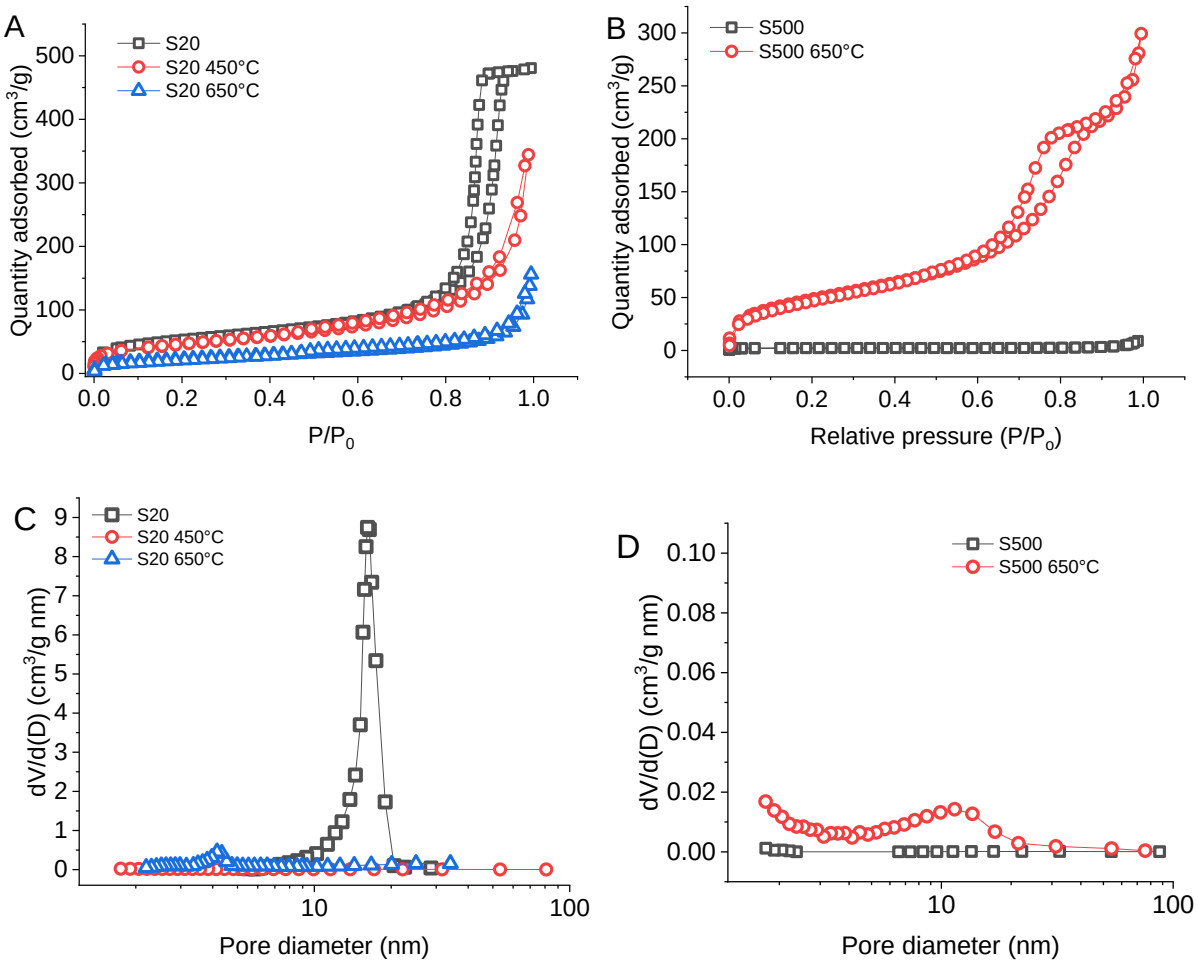

Figure S2: The isotherms for pristine and reduced A) S20 particles* and B) S500 particles are given. C) The BJH desorption pore sizes are shown for C) S20 and D) S500 samples, both reduced and unreduced samples. *While S20 does not have any internal surface area, the data in parts (A) and (C) include external surface area.

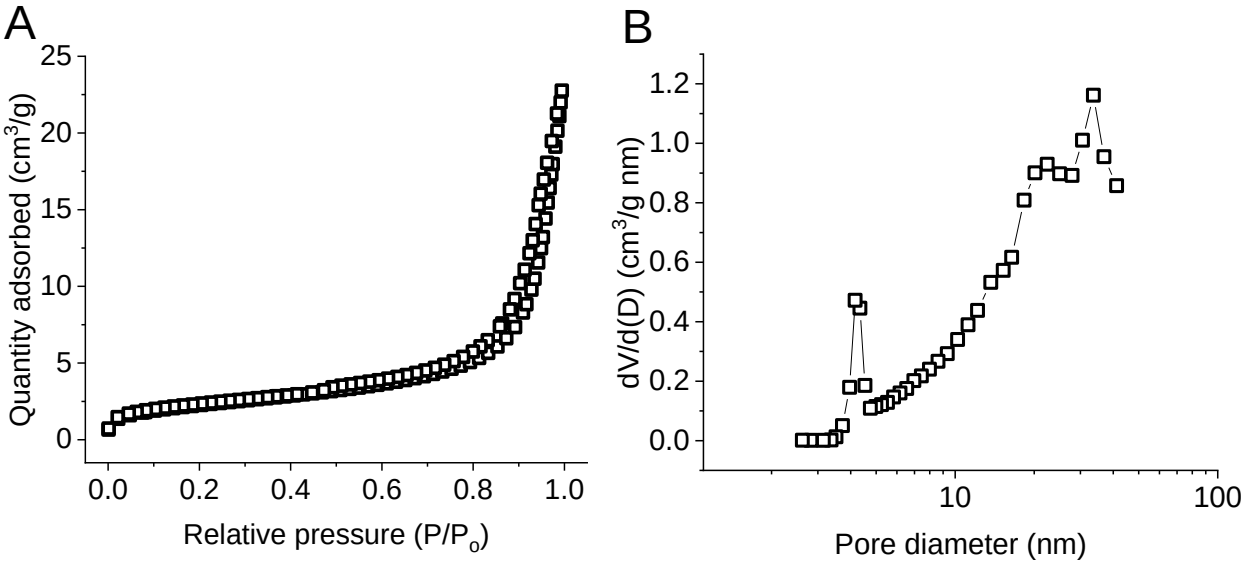

Figure S3: A) Gas adsorption isotherm and B) pore size distribution of 75 nm particles (S75) reduced at 650°C.

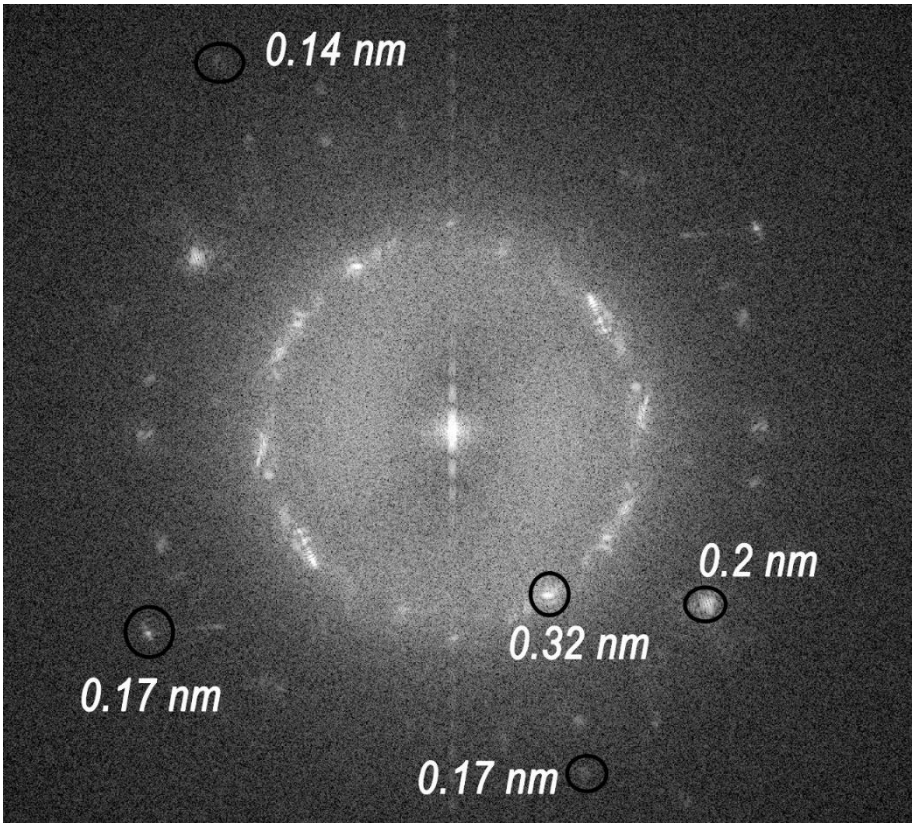

Figure S4: FFT analysis of the TEM image shown in Figure 3B. d-spacings for all identified crystal planes are shown on the image and associated parameters are listed in Table S3.

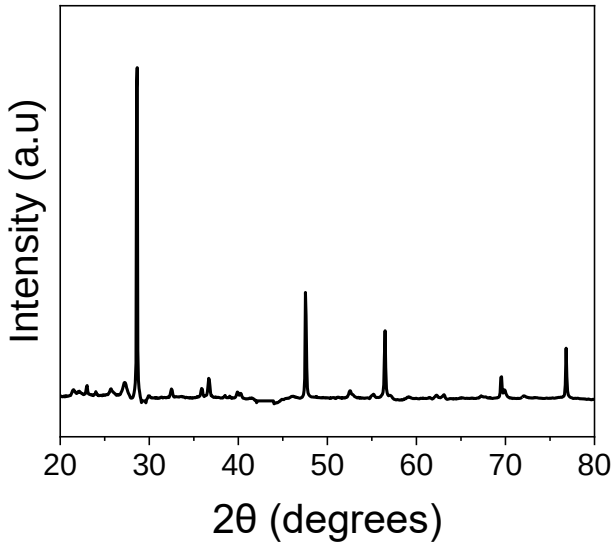

Figure S5: XRD of the reduction of F7 at 380°C after washing in HCl.

8.2. Chapter 5 Supporting information

Electronic Supplementary Information

Nanoscale triggering effect unlocks sustainable manufacturing of high-performance porous silicon anodes

*Maximilian Yan and Siddharth V. Patwardhan**

Department of Chemical and Biological Engineering, Green Nanomaterials Research Group, The University of Sheffield, Mappin Street, Sheffield S1 3JD, UK. *s.patwardhan@sheffield.ac.uk

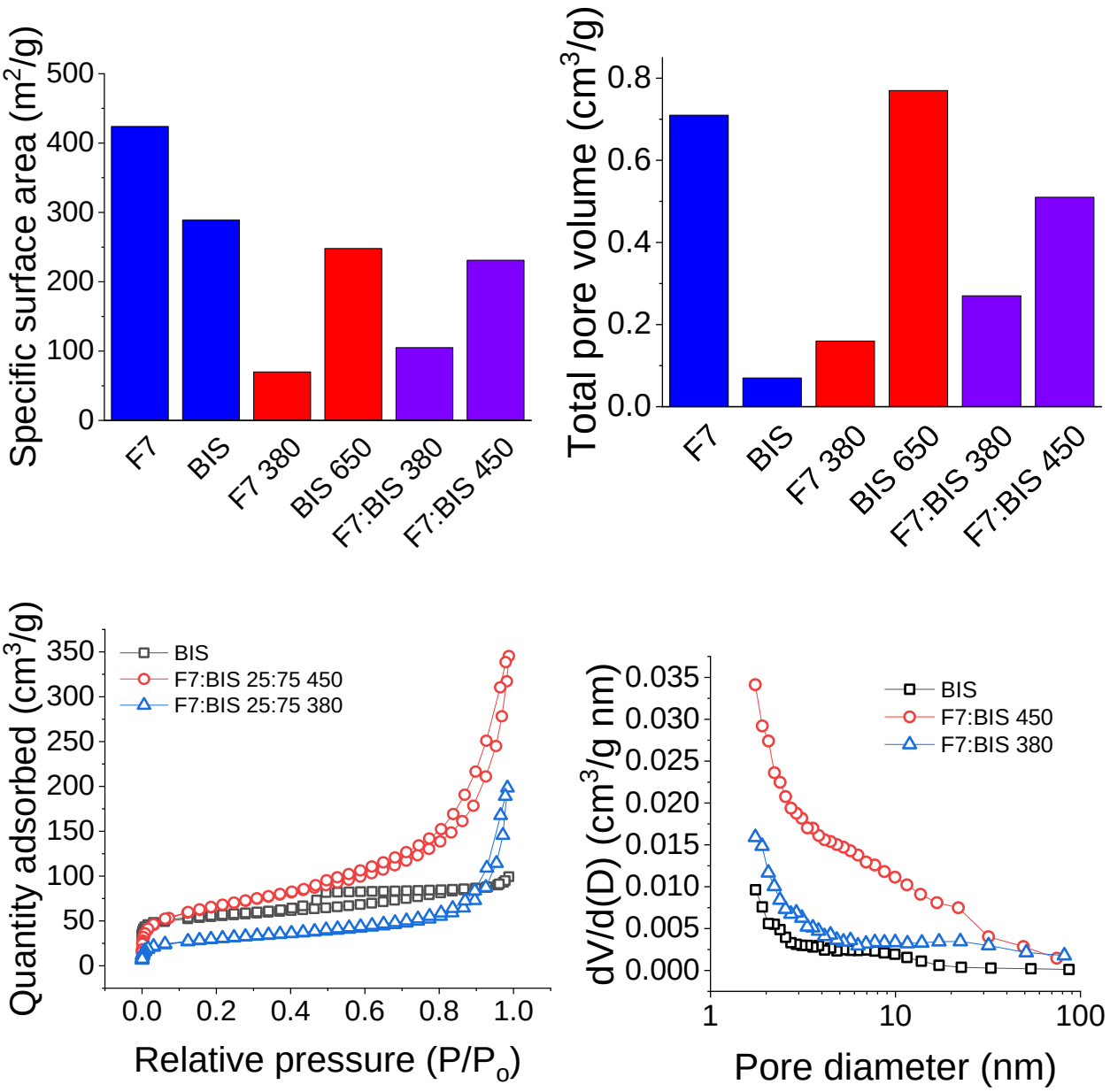

Figure S1: The A) SSA and B) total pore volume of single and mixed A)BIS silica samples are shown. Blue indicate pristine silica, red unmixed reductions are the stated temperatures, purple indicate mixed reductions. Mixed samples were of a 25:75 F7 to BIS weight ratio. The C) gas adsorption isotherms and D) pore size distribution.

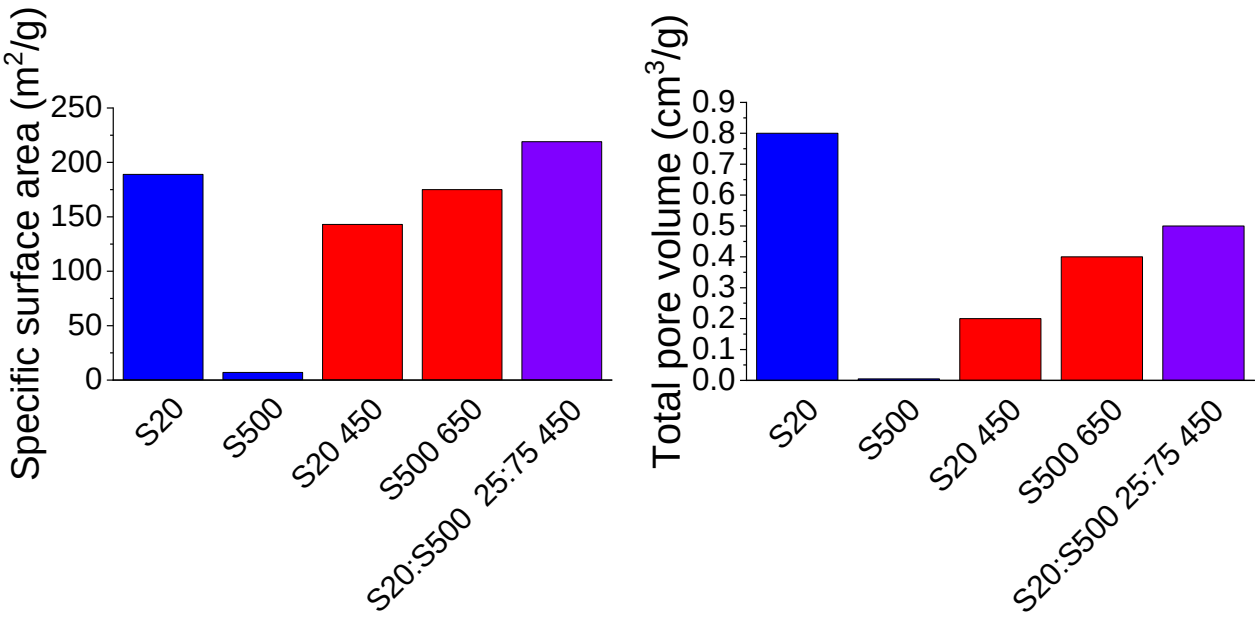

Figure S2: The A) SSAs and B) total pore volumes for pristine, reduced, and mixed reduced silicas are shown. Pristine silicas are coloured blue, reduced silicas red, and mixed reduced silicas purple.

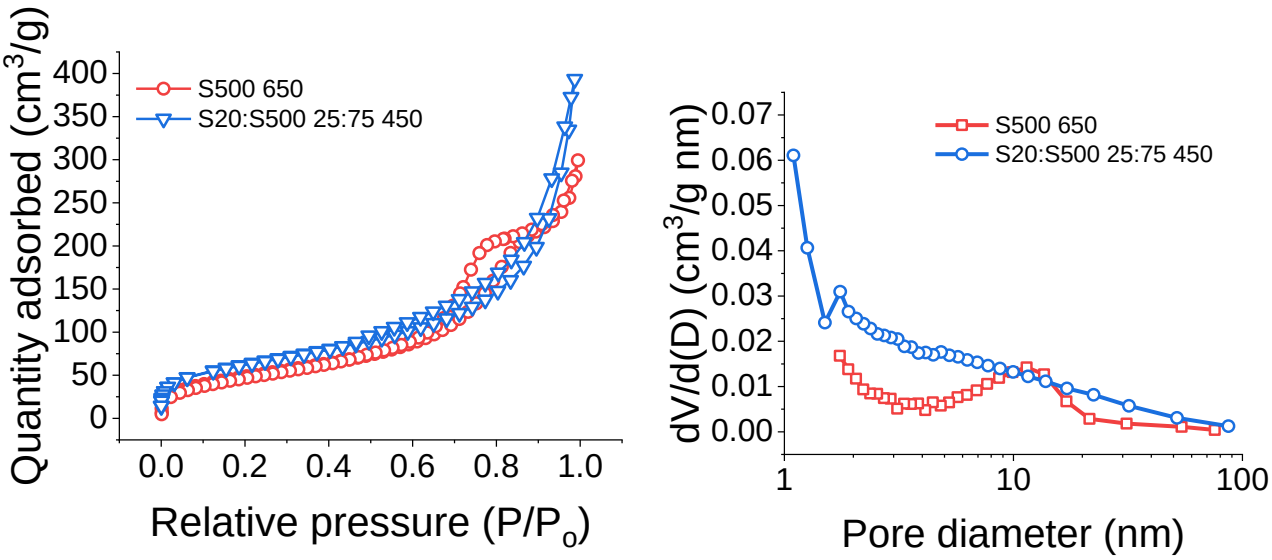

Figure S3: The A) isotherms and B) BJH desorption pore volume data for 500 nm particles reduced alone at 650°C and mixed with 20 nm and reduced at 450°C are shown.

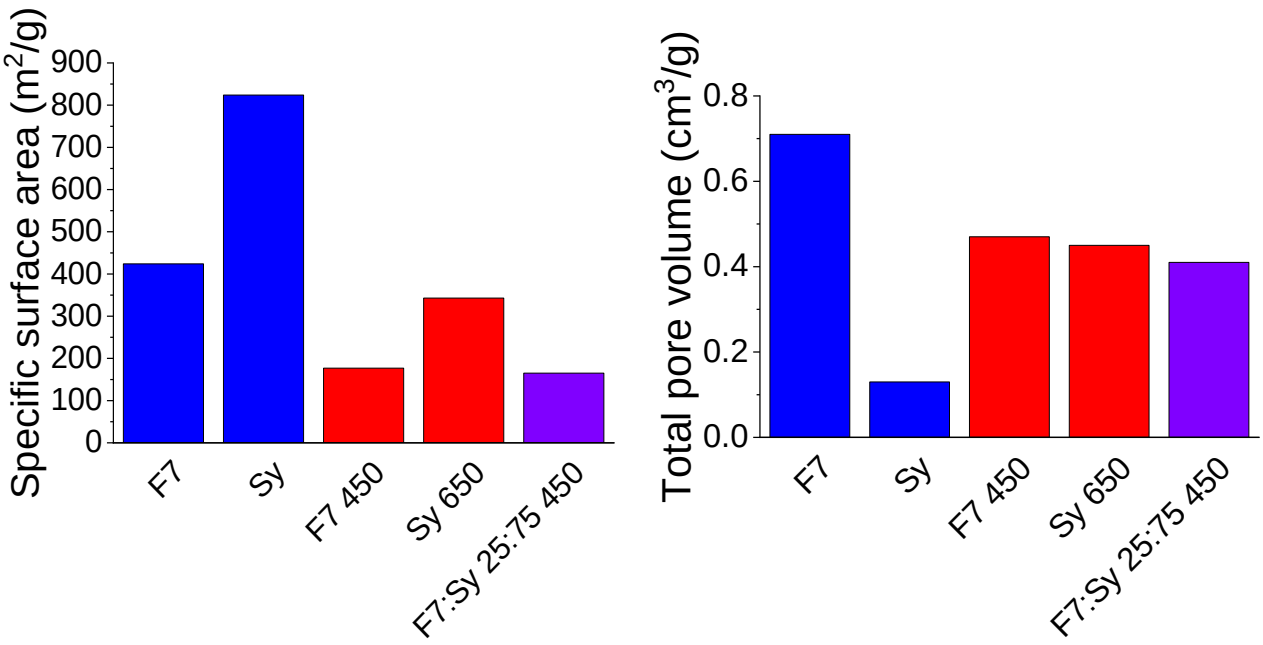

Figure S4: A)SSAs and B) total pore volume are shown for pristine silica (blue), reduced silica (red), and mixed reduced silica (purple).

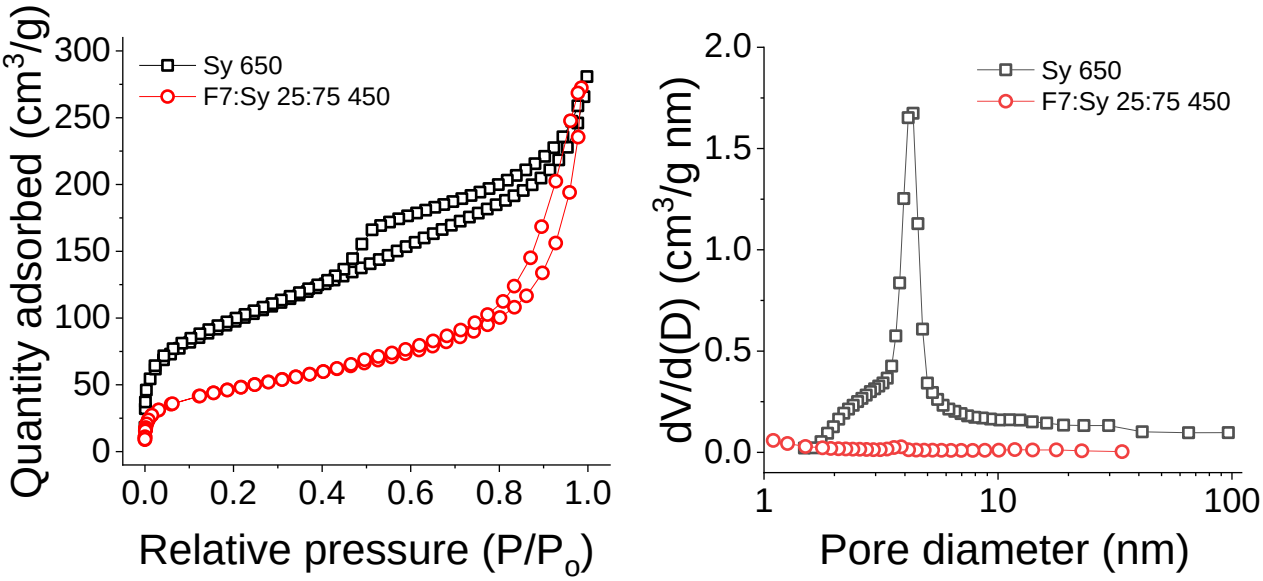

Figure S5: A) Isotherms and B) BJH pore size distribution of Sy reduced at 650°C, and reduced with F7 at 450°C.

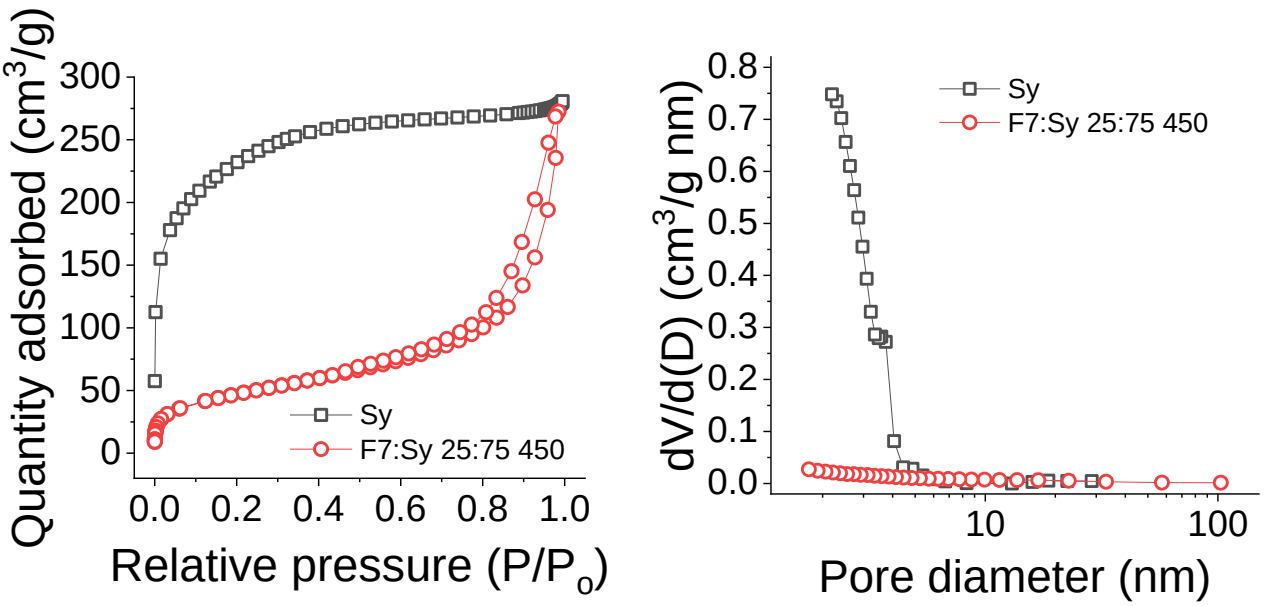

Figure S6: A) Isotherms and B) BJH pore size distribution of pristine Sy and Sy reduced with F7 at 450°C.

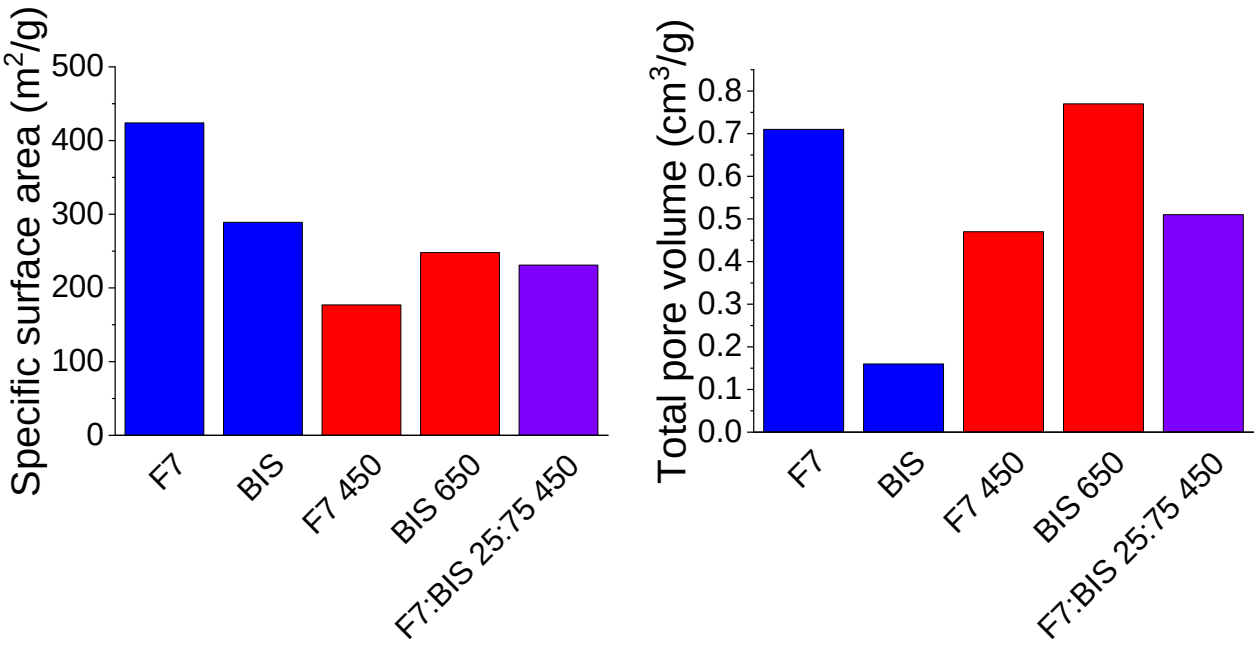

Figure S7: A) SSAs and B) total pore volume of pristine (blue), reduced (red) and mixed reduced (purple) F7 and BIS.

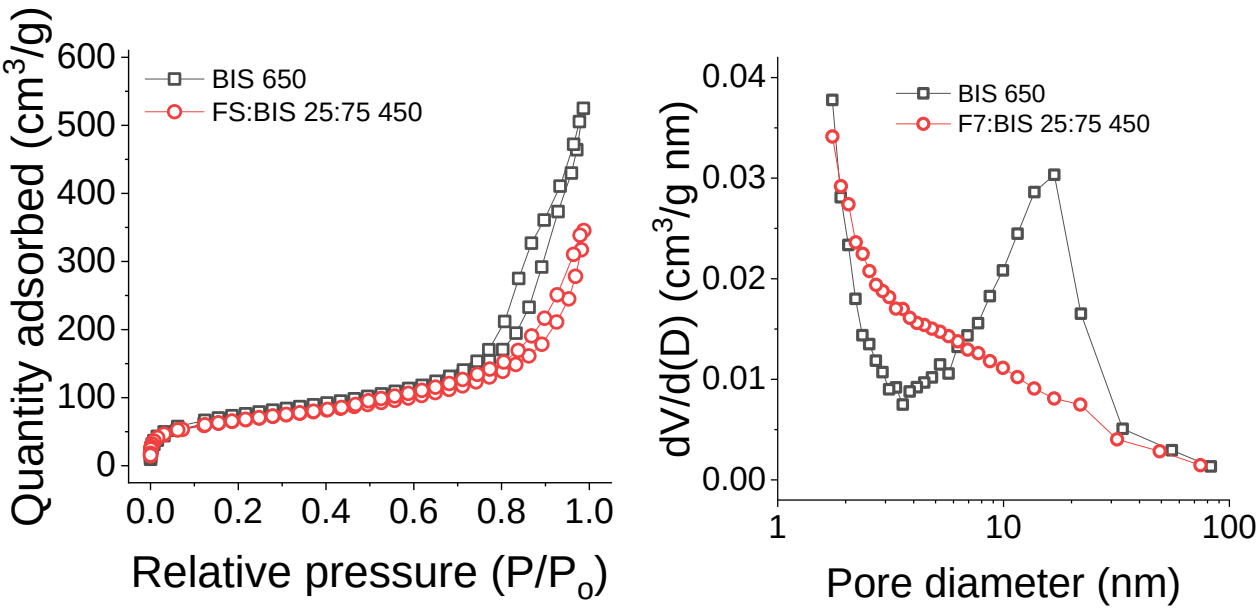

Figure S8: A) Isotherms and B) BJH pore size distribution of BIS reduced at 650°C, and reduced with F7 at 450°C.

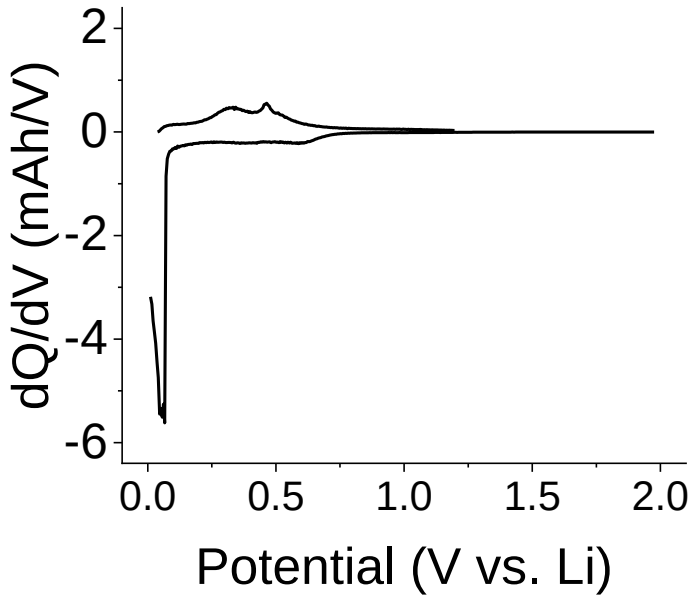

Figure S9: Differential capacity plot of the first cycle of S20 450°C

8.3. Chapter 6 Supporting information

Large-scale manufacturing of porous silicon via the magnesiothermic reduction: a techno-economic analysis

Maximilian Yan [a,b], Sarah Martell[b], Mita Dasog [b], Solomon Brown[a] and Siddharth V. Patwardhan [a]*

[a] *Department of Chemical and Biological Engineering, The University of Sheffield, Mappin Street, Sheffield S1 3JD, United Kingdom.*

[b] *Department of Chemistry, Dalhousie University, 6274 Coburg Road, Halifax, NS B3H 4R2, Canada.*

* *Corresponding authors, s.patwardhan@sheffield.ac.uk*

Assumptions

- Process efficiency (η_p) of 0.8
- Rotary kiln is shaped as a hollow cylinder with length to diameter ratio (L/D) of 5
- The volume of the reactant powder occupies 15% of the total kiln volume
- Wall thickness of rotary kiln is 5% of inner diameter
- The ends of the rotary kiln are capped with cylinders of heights equal to the wall thickness
- Rotary kiln is rotated at a speed of 17 rpm
- Heat loss is by radiation and conduction and convection
- Rotary kiln construction material is stainless steel
- Assume gas fired, with a thermal efficiency (η_{therm}) of 0.8

Conservative estimates:

- Powder volume:
    - Tap density measured in the lab for mixtures of Mg and various SiO_2 powder, in kg/m^3 is underestimated, which will give an overestimate of the total powder volume, hence an overestimate of the size of the reactor, and heat loss.
    - Overestimation of the total powder volume will also give an overestimate of the powder mixer power requirements

- Rotary kiln:
    - The lower bound of thermal efficiency of the rotary kiln was chosen from a quoted typical range[145]
    - Volume loading of the rotary kiln is typically 10-20%. A mid-range value of 15% was chosen.

  - Wall thickness of a stainless-steel furnace is usually around 1% of its inner diameter. 5% was chosen in this case given the rotary and heating requirements.
  - When calculating heat loss, assume that the whole mass of the stainless-steel kiln is heated up to the reduction temperature. This is an overestimate of the total energy required
  - No heat is recycled.

- Agitated vessel:
  - Additional 10% of HCl is added to the stoichiometric requirement to remove Mg.

- Dryer:
  - Additional 10% is added to typical values of filter cake moisture content taken from the literature.

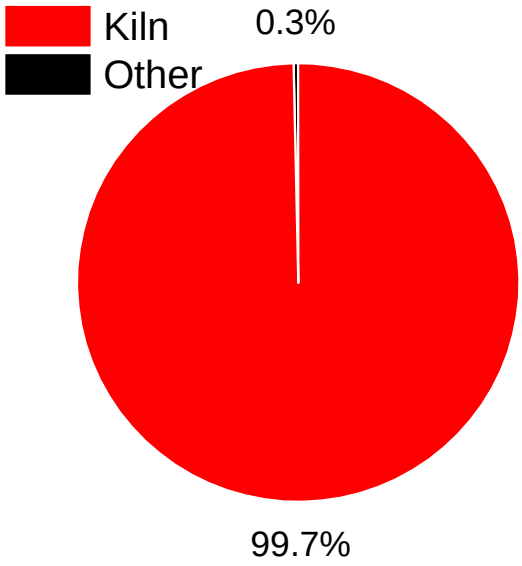

Figure S1: Proportion of energy required by the kiln, compared to the rest of the equipment.

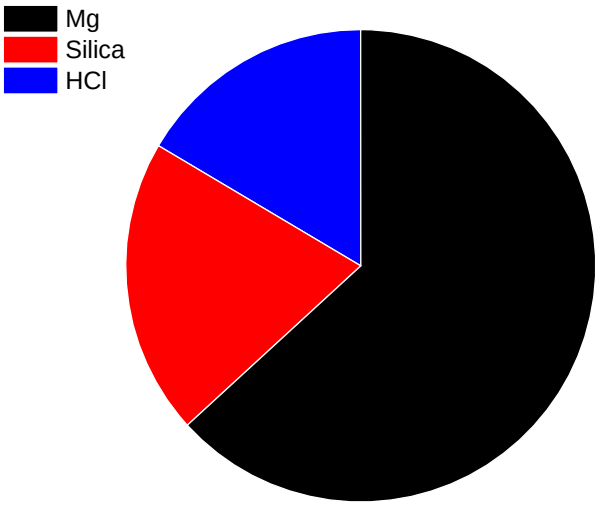

Figure S2: The proportions of total feedstock cost of each reagent are shown.

8.4. TEA conditions and equations

Table S1:

Conditions	Scenario 1 (Baseline)	Scenario 7	Scenario 8
Powder mixing (mins)	30	30	30
Ramp rate (°C/min)	5	5	5
Max temp (°C)	650	380	360
Reduction time (mins)	360	360	180
Dissolution time (hrs)	24	24	24
Yield (mol %)	60	80	76

Table S2:

Conditions	Scenario 6 (two-step)
Powder mixing (mins)	30
Ramp rate (°C/min)	5
1st temp (°C)	650
Reduction time at 1st temp (mins)	30
2nd temp (°C)	300
Reduction time at 2nd temp (mins)	360
Dissolution time (hrs)	4
Yield (mol %)	88

Table S3: Constants used in process calculations. Data collected from NIST Chemical Reference Data, CRC Handbook of Chemistry and Physics, and Perry's Chemical Engineers' Handbook. Thermal efficiency of kiln and process efficiencies were assumed conservatively.

Symbol	Description	Value	Units
C_{p_ace}	Heat capacity of acetone	2.125	kJ/kg K
C_{p_Mg}	Heat capacity of Mg	1.02	kJ/kg K
C_{p_Si}	Heat capacity of Si	0.715	kJ/kg K
C_{p_SiO2}	Heat capacity of SiO2	0.746	kJ/kg K
C_{p_steel}	Heat capacity of steel	0.581	kJ/kg K
Δh_{Mg_diss}	Enthalpy of dissolution of Mg in HCl	-456.7	kJ/mol
Δh_{MgO_diss}	Enthalpy of dissolution of MgO in HCl	144.3	kJ/mol
ε	Emissivity of steel	0.7	unitless
η_{therm}	Thermal efficiency of kiln	0.8	unitless
η_{proc}	Process efficiency	0.8	unitless
h_{vap}	Enthalpy of vaporisation of acetone	509.64	kJ/kg
k	Thermal conductivity of steel	23.02	W/m K
k_{air}	Thermal conductivity of air	0.025	W/m K
μ	Viscosity of air	2.23×10^{-5}	Pa.s
M_{HCl}	Concentration of aqueous HCl	1	$kmol/m^3$
Mr_{Mg}	Molar mass of Mg	24.3	kg/kmol
Mr_{Si}	Molar mass of Si	28	kg/kmol
Mr_{SiO2}	Molar mass of SiO_2	60	kg/kmol
Pr	Prandtl number	0.7	dimensionless
q_{HCl}	Specific power of vessel impeller	1	kW/m^3
q_{mix}	Specific power of a spiral ribbon mixer	12	kW/m^3
ρ_{air}	Density of air	1.784	kg/m^3
ρ_{steel}	Density of steel	7900	kg/m^3
σ	Stefan-Boltzmann constant	5.67×10^{-8}	W/m^2K^4
T_{room}	Room temperature	298	K

Table S4: List of variables

Symbol	Description	units
m_{Si}	Specified target amount of Si to be made	kg/day
ρ_{tap}	Tap density of Mg and SiO2	kg/m^3
R_{ms}	Mass ratio of Mg to Si	unitless
r_m	Ramp rate	°C/min
T_{dwell1}	First step temperature	K
T_{dwell2}	Second step temperature (two-step)	K
t_{dwell1}	Dwell time at first temperature	minutes
t_{dwell2}	Dwell time of second step (two-step)	minutes
t_{p_mix}	Time allocated for powder mixing	minutes
t_{stir}	Time allocated for acid etching step	minutes
u_{cHCl}	Unit cost of HCl	kg/currency
u_{cMg}	Unit cost of Mg	kg/currency
u_{cSiO2}	Unit cost of SiO_2	kg/£
y	Specified yield of Si, based on experiments	1 = 100 mol%

Table S5: Other symbols

Symbol	Description	Unit
c_{feed}	Total feedstock cost	Currency
$c_{feed\_spec\_cost}$	Specific feedstock cost	Currency/kg Si
c_{Mg}	Total cost of Mg	Currency
C_{proc_total}	Total process cost	Currency
$C_{Si\_per\_kg}$	Specific cost of Si	Currency/kg Si
c_{SiO2}	Total cost of silica	Currency
$c_{energy\_spec\_cost}$	Specific energy cost of the process	Currency/kg Si
D	Diameter of rotary kiln	m
h_{asens}	Total heat to raise temperature of acetone from 25-56°C	kJ
h_{avap}	Total latent heat acetone required at 56°C	kJ
h_{cond}	Total conductive heat loss, ramp and dwell	kJ
h_{cond_dwell}	Total conductive heat loss during dwell	J
h_{cond_ramp}	Total conductive heat loss during ramp	J
h_{conv}	Total convective heat loss, ramp and dwell	kJ
h_{conv_dwell}	Total convective heat loss during dwell	J
h_{conv_ramp}	Total convective heat loss during ramp	J
h_{cool}	Total energy required for cooling	kJ
h_{dry}	Total energy required to dry product	kJ
h_{kiln}	Total kiln energy requirement	kJ
h_{Mg}	Energy required to heat Mg feedstock	kJ
h_{p_mix}	Total energy consumed by the mixer	kJ
h_{proc_cost}	Total cost of the process	Currency/kg Si
h_{proc_kWh}	Total energy cost of the process	kWh
h_{proc_total}	Total energy cost of the process	kJ
h_{prod}	Total heat to raise temperature of Si and unreacted SiO_2	kJ
h_{rad}	Total radiative heat loss, ramp and dwell	kJ
h_{rad_dwell}	Total radiative heat loss during dwell	J
h_{rad_ramp}	Total radiative heat loss during ramp	J
h_{SiO2}	Energy required to heat silica feedstock	kJ
h_{stir}	Total energy required for stirring	kJ
h_{supply}	Total energy supplied to the kiln	kJ
h_{total}	Total energy required to heat mass of kiln and reactants	kJ
h_{tube}	Energy required to heat kiln	kJ
h_{vessel}	Total energy required in agitator step	kJ
L	Length of rotary kiln	m
m_{ace}	Mass of acetone to be evaporated in dryer	kg
m_{Mg}	Mass of Mg required	kg
m_{Si}	Mass of Si product required	kg
$m_{SiO2\text{-}feed}$	Mass of SiO_2 feedstock required	kg
n_{HCl}	Moles of HCl required	kmol
n_{MgO}	Moles of MgO produced	kmol
n_{Mg_unre}	Moles of Mg that remains unreacted	kmol
m_{prod}	Mass of product: Si and unreacted SiO_2	kg
Q_{cond_dwell}	Conductive heat loss during dwell (one-step)	W
Q_{conv_dwell}	Convective heat loss during dwell (one-step)	W
Q_{HCl}	Impeller power requirement	kW
Q_{p_mix}	Mixer power requirement	kW
Q_{rad_dwell}	Radiative heat loss during dwell (one-step)	W
R_e	Reynolds number for flow of air perpendicular to length of kiln	unitless
N_u	Nusselt number, assuming turbulent flow regime	unitless
S_{kiln}	Surface area of kiln	m^2

t_{lim}	Time taken to reach specified reduction temp, given the ramp rate	s
V_{HCl}	Volume of HCl required	m^3
V_{RK}	Volume of rotary kiln required	m^3

Table S6: Two-step symbols

Symbol	Description	Unit
Q_{cond_dwell1}	Conductive heat loss during first dwell step (two-step)	W
Q_{cond_dwell2}	Conductive heat loss during second dwell step (two-step)	W
Q_{conv_dwell1}	Convective heat loss during first dwell step (two-step)	W
Q_{conv_dwell2}	Convective heat loss during second dwell step (two-step)	W
Q_{rad_dwell1}	Radiative heat loss during first dwell step (two-step)	W
Q_{rad_dwell2}	Radiative heat loss during second dwell step (two-step)	W

Mass of Si product required: m_{Si} = 300 kg/d

8.4.1. Reaction equations

Amount of SiO_2 and Mg required in mass (kg):

$$m_{SiO2\_feed} = \frac{Mr_{SiO2}\, m_{Si}}{Mr_{Si}\, y\, \eta_p} \quad \text{Equation 1}$$

$$m_{Mg} = R_{ms} * m_{SiO2\_feed} \quad \text{Equation 2}$$

Amount of MgO produced (n_{MgO}) in kmols:

$$n_{MgO} = \frac{2m_{Si}}{\eta_p Mr_{Si}} \quad \text{Equation 3}$$

Amount of Mg unreacted (n_{Mg_unre}) in kmols:

$$n_{Mg\_unre} = \frac{m_{Mg}}{Mr_{Mg}} - n_{MgO} \quad \text{Equation 4}$$

Powder mixer

Powder mixer power requirement:

$$Q_{pmix} = \frac{(m_{SiO2\_feed} + m_{Mg})\, q_{mix}}{\rho_{tap}} \quad \text{Equation M1}$$

$$h_{pmix} = Q_{pmix} * 60 t_{pmix}$$

Indirect fired rotary kiln

First, the volume of the kiln is calculated from the volume of the reactants going in. The volume of the reactant mixture is calculated from its mass and tap density. Equations for surface area were derived on the assumption that the kiln is a hollow cylinder with capped ends. Using typical values for volume loading, length to diameter ratios (L/D), and wall thickness, the external surface area of the kiln was calculated.

Energy is required to heat the reactants and the kiln (sensible heat) during the ramping step and to counter heat losses during the ramping and the dwelling step. Heat is lost through radiation, conduction, and convection from the surface of the kiln. For the two-step procedure, there are two dwelling processes at different temperatures. Heat losses for this procedure is calculated taking this into account in equations K20 – K28.

Volume of rotary kiln (V_{RK}) in m^3:

$$V_{RK} = \frac{(m_{SiO2\_feed} + m_{Mg})}{0.15\ \rho_{tap}} \qquad \text{Equation K1}$$

Surface area of rotary kiln (S_{kiln}) in m:

$$S_{kiln} = 6.215\pi \left(\frac{4V_{RK}}{5\pi}\right)^{\frac{2}{3}} \qquad \text{Equation K2}$$

Total radiative heat loss during ramp (h_{rad_ramp}) in J:

$$h_{rad\_ramp} = \sigma S_{kiln} \left[\frac{12\left(\frac{t_{el} \times r_m}{60} + T_{room}\right)^5}{r_m} - T_{room}^4 \times t_{el} \right]_{t_{el}=0}^{t_{el}=t_{lim}} \qquad \text{Equation K3a}$$

$$t_{lim} = \frac{60(T_{red} - T_{room})}{r_m} \qquad \text{Equation K3b}$$

Radiative heat loss while holding at temperature (Q_{rad}) in W:

$$Q_{rad\_dwell} = \varepsilon\sigma S_{kiln}\left(T_{red}^4 - T_{room}^4\right) \qquad \text{Equation K4}$$

Total radiative heat loss at temperature ($h_{rad\ dwell}$) in J:

$$h_{rad\_dwell} = Q_{rad} \times 60t \qquad \text{Equation K5}$$

Total radiative heat loss (h_{rad}) in kJ:

$$h_{rad} = \frac{h_{rad\_ramp} + h_{rad\_dwell}}{1000} \qquad \text{Equation K6}$$

Total conductive heat loss during ramp ($h_{cond\ ramp}$) in J:

$$h_{cond\ ramp} = \frac{kS_{kiln}}{0.05D}\left[\frac{30}{r_m}\left(\frac{r_m \times t_{el}}{60} + 298\right)^2 - T_{room} \times t_{el}\right]_{t_{el}=0}^{t_{el}=t_{lim}} \quad \text{Equation K7a}$$

$$t_{lim} = \frac{60(T_{red} - T_{room})}{r_m} \quad \text{Equation K7b}$$

Conductive heat loss (Q_{cond_dwell}) in W:

$$Q_{cond\_dwell} = \frac{kS_{kiln}(T_{red} - T_{room})}{0.05D} \quad \text{Equation K8}$$

Total conductive heat loss at temperature (h_{cond_dwell}) in J:

$$h_{cond\_dwell} = Q_{cond\_dwell} \times 60t \quad \text{Equation K9}$$

Total conductive heat loss (h_{cond}) in kJ:

$$h_{cond} = \frac{h_{cond\_ramp} + h_{cond\_dwell}}{1000} \quad \text{Equation K10}$$

Convection heat loss (Q_{conv_dwell}) in W

$$Q_{conv\_dwell} = \frac{kN_u S_{kiln}(T_{red} - T_{room})}{D} \quad \text{Equation K11a}$$

$$R_e = \frac{17\rho D^2}{60\mu} \quad \text{Equation K11b}$$

$$N_u = 0.027 {R_e}^{0.805} P_r^{1/3} \quad \text{Equation K11c}$$

Convection heat loss at temperature (h_{conv_dwell}) in J:

$$h_{conv\_dwell} = Q_{conv\ dwell} \times 60t \quad \text{Equation K12}$$

Convection heat loss during ramping h_{conv_ramp} in J:

$$h_{conv\_ramp} = \frac{kN_u S_{kiln}}{D}\left[\frac{60}{2r_m}\left(\frac{r_m t_{el}}{60} + 298\right)^2 - T_{room} t_{el}\right]_{t_{el}=0}^{t_{el}=t_{lim}}$$ Equation K13a

$$t_{lim} = \frac{60(T_{red} - T_{room})}{r_m}$$ Equation K13b

Total convection heat loss (h_{conv}) in kJ:

$$h_{conv} = \frac{h_{conv\_ramp} + h_{conv\_dwell}}{1000}$$ Equation 14

Energy required to heat kiln (h_{tube}) in kJ

$$h_{tube} = \rho_{steel}\left(\frac{1.171\pi D^3}{4}\right) C_{p\ steel}\ (T_{red} - T_{room})$$ Equation K15

Energy required to heat reactants in kJ

$$h_{SiO2} = m_{SiO2-feed}\ C_{p\ SiO2}\ (T_{red} - T_{room})$$ Equation K16a

$$h_{Mg} = m_{Mg}\ C_{p\ Mg}\ (T_{red} - T_{room})$$ Equation K16b

Total energy required for sensible heat (h_{total}) in kJ:

$$h_{total} = h_{tube} + h_{SiO2} + h_{Mg}$$ Equation K17

Total kiln energy requirement (h_{kiln}) in kJ

$$h_{kiln} = h_{rad} + h_{cond} + h_{conv} + h_{total}$$ Equation K18

Total energy supplied to kiln (h_{supply}) , taking into account thermal efficiency

$$h_{supply} = \frac{h_{kiln}}{\eta_{therm}}$$ Equation K19

Stirred vessel

Energy is required for the impeller and to remove heat from the reaction of HCl with various Mg species. A specific power value from the literature is used to calculate the power requirement of the impeller based on the total volume of acid.

The heat released from the reactions of Mg species (Mg and MgO) with HCl were calculated using reaction enthalpies from the literature. The reaction between Mg and HCl is exothermic, while the reaction between MgO and HCl is endothermic.

Moles of HCl required (n_{HCl}) in kmol:

$$n_{HCl} = \frac{2.2 m_{Mg}}{Mr_{Mg}} \quad \text{Equation V1}$$

Volume of HCl required (V_{HCl}) in m3:

$$V_{HCl} = n_{HCl} M_{HCl} \quad \text{Equation V2}$$

Impeller power requirement (Q_{HCl}) in kW:

$$Q_{HCl} = V_{HCl}\, q_{HCl} \quad \text{Equation V3}$$

Total energy required for the impeller (h_{stir}) in kJ:

$$h_{stir} = Q_{HCl} * t_{stir} * 60 \quad \text{Equation V4}$$

Total energy required for cooling (h_{cool}) in kJ:

$$h_{cool} = (n_{Mg\_unre} * \Delta H_{Mg\_diss} + n_{MgO} * \Delta H_{MgO\_diss}) * 1000 \quad \text{Equation V5}$$

Total energy required in agitator step in kJ:

$$h_{vessel} = h_{stir} + h_{cool} \quad \text{Equation V6}$$

Dryer

The physical processes involved in the drying step include:

- Heating the product to the target temperature (sensible heat)
- Heating the solvent to the target temperature (sensible heat)
- Evaporate solvent at target temperature (latent heat)

°The product after filtration is in the form of a filter cake with acetone as the solvent. The amount of acetone is calculated as a percent of the total mass of the product (256%), from typical values quoted in Walas.

Mass of product as a function of reaction yield (m_{prod}) in kg:

$$m_{prod} = \left(\frac{(1-y)m_{Si}}{Mr_{Si}\, y}\right) Mr_{SiO2} + m_{Si} \qquad \text{Equation D1}$$

Mass of acetone (m_{ace}) in kg:

$$m_{ace} = 2.56 m_{prod} \qquad \text{Equation D2}$$

Total energy required to raise temperature of acetone from 25-56°C (h_{asens}) in kJ:

$$h_{asens} = 31 m_{ace} C_{p\_ace} \qquad \text{Equation D3}$$

Total energy required to vaporise acetone at 56°C (h_{avap}) in kJ:

$$h_{avap} = m_{ace} h_{vap} \qquad \text{Equation D4}$$

Total energy required to heat the solid product from 25-56°C (h_{prod}) in kJ:

$$h_{prod} = 31\left(\frac{(1-y)m_{Si}}{Mr_{Si} y}\right) Mr_{SiO2} C_{p\_SiO2} + 31 m_{Si} C_{p\_Si} \qquad \text{Equation D5}$$

Total energy required for drying (h_{dry}) in kJ:

$$h_{dry} = h_{asens} + h_{avap} + h_{prod} \qquad \text{Equation D6}$$

Scenario 1 (650°C 30 mins, 300°C 6 hours) kiln calculations (at each temperature)

Need to consider that there are 2 dwell steps, which occur at different temperatures and durations. Therefore, the heat loss from each step will be different. The equations below are used to simply calculate the rate of heat loss at each step, and the total energy lost given the time spent at each step.

Radiative heat loss at separate temperatures, in W:

At 650°C:

$$Q_{rad1} = \varepsilon \sigma S_{kiln}(923^4 - 298^4) \qquad \text{Equation K20}$$

At 300°C:

$$Q_{rad2} = \varepsilon\sigma S_{kiln}(573^4 - 298^4)$$ Equation K21

Total energy lost through radiative transfer to environment (h_{rad}) in J:

$$h_{rad\_dwell} = 60(t_{dwell1}Q_{rad1} + t_{dwell2}Q_{rad2})$$ Equation K22

$$h_{rad} = \frac{h_{rad\_ramp} + h_{rad\_dwell}}{1000}$$ Equation K6

Conductive heat loss at separate temperatures, in W:

At 650°C:

$$Q_{cond1} = \frac{625kS_{kiln}}{0.05D}$$ Equation K23

At 300°C:

$$Q_{cond2} = \frac{275kS_{kiln}}{0.05D}$$ Equation K24

Total energy lost through conductive heat transfer to environment (h_{cond}) in J:

$$h_{cond\_dwell} = 60(t_{dwell1}Q_{cond1} + t_{dwell2}Q_{cond2})$$ Equation K25

$$h_{cond} = \frac{h_{cond\_ramp} + h_{cond\_dwell}}{1000}$$ Equation K8

Convective heat loss at separate temperatures (Q_{conv}) in W:

At 650°C:

$$Q_{conv1} = \frac{625kN_uS_{kiln}}{D}$$ Equation K26

At 300 °C:

$$Q_{conv2} = \frac{275kN_uS_{kiln}}{D}$$ Equation K27

Total energy lost through convective heat transfer to environment (h_{conv_dwell}) in kJ:

$$h_{conv\_dwell} = 60(t_{dwell1}Q_{conv1} + t_{dwell2}Q_{conv2})$$ Equation K28

$$h_{conv} = \frac{h_{conv\_ramp}+h_{conv\_dwell}}{1000}$$ Equation K14

Energy cost

Total energy cost of the process (h_{proc_total})in kJ

$$h_{proc\_total} = h_{p\_mix} + h_{supply} + h_{vessel} + h_{dry}$$ Equation E1

Converting kJ to kWh

$$h_{proc\_kWh} = \frac{h_{proc\_total}}{3600}$$ Equation E2

Cost of the process (h_{proc_cost}) in a unit of currency given a unit cost of energy:

$$h_{proc\_cost} = h_{proc\_kWh} * u_{c\_energy}$$ Equation E3

Specific energy cost of the process ($c_{energy\_spec\_cost}$) in currency/kg Si:

$$c_{energy\_spec\_cost} = h_{proc\_cost}/m_{Si}$$ Equation E4

Feedstock cost

Total cost of silica per batch (c_{SiO2}) in a given currency:

$$c_{SiO2} = u_{c\_SiO2} * m_{SiO2\_feed}$$ Equation F1

Total cost of Mg per batch (c_{Mg}) in a given currency:

$$c_{Mg} = u_c * m_{Mg}$$ Equation F2

Total feedstock cost (c_{feed}) in a given currency:

$$c_{feed} = c_{SiO2} + c_{Mg}$$ Equation F3

Specific feedstock cost ($c_{feed\_spec\_cost}$) in currency/kg:

$$c_{feed\_spec\_cost} = c_{feed}/m_{Si} \quad \text{Equation F4}$$

Process cost

Total process cost (c_{proc_total}) in a given currency:

$$C_{proc\_total} = h_{proc\_cost} + c_{feed} \quad \text{Equation P1}$$

Specific cost of Si ($C_{Si\_per\_kg}$) in currency/kg Si:

$$C_{Si\_per\_kg} = c_{energy\_spec\_cost} + c_{feed\_spec\_cost} \quad \text{Equation P2}$$

8.4.2. Annotated Matlab script

The equations above were entered into Matlab so that calculations could be run multiple times quickly for different process conditions. The script is included below:

```
%% Constants

Mr_SiO2 =60;     % Molar mass of SiO2 (kg/kmol)
Mr_Si = 28;      % Molar mass of Si (kg/kmol)
Mr_Mg = 24.3;    % Molar mass of (Mg kg/kmol)
eta_p = 0.8;     % process efficiency (in terms of loss of material that can occur
between each step)
q_mix = 12;      % specific mixing power of a spiral ribbon mixer (kW/m3)

epsilon = 0.7;          % emissivity of steel
sigma = 5.67*10^-8;     % Stefan-Boltzmann constant
T_room = 298;           % Room temp, in K, used to calculate delta T in various
equations

k = 23.02;              % thermal conductivity of stainless steel (W/m K)
k_air = 0.025;          % thermal conductivity of air (W/m K)
rho_air = 1.784;        % density of air (kg/m3)
mu = 2.23*10^-5;        % viscosity of air (Pa.s)
Pr = 0.7;               % Prandtl number

rho_steel = 7900;       % density of steel (kg/m3)
Cp_steel = 0.581;       % heat capacity of steel (kJ/kg K)
Cp_SiO2 = 0.746;        % heat capacity of silica (kJ/kg K)
Cp_Mg = 1.02;           % heat capacity of Mg (kJ/kg K)
Cp_Si = 0.715;          % heat capacity of Si (kJ/kg K)
```

```
eta_therm = 0.8;        % thermal efficiency of a gas fired kiln

dh_Mg_diss = -456.7;     % enthalpy of reaction of Mg with HCl (kJ/mol)
dh_MgO_diss = 144.3;     % enthalpy of reaction of MgO in HCl (kJ/mol)
M_HCl = 1;               % concentration of HCl
q_HCl = 1;               % specific mixing energy of a vessel impeller (kW/m3)

h_vap = 509.64;          % enthalpy of vapourisation of acetone (kJ/kg)
Cp_ace = 2.125;          % specific heat capacity of acetone (kJ/kg K)


%% Variables

m_Si = 300;          % specified target amount of Si to be made (kg/day)
y = 0.60;             % specified yield of silicon, based on old experimental data
(0.6 means 60 mol%)
R_ms = 1;            % mass ratio of Mg to Si (in this case 1 means 1:1 mass
ratio, or 2.5:1 mol ratio)
rho_tap = 916;       % tap density of Mg and SiO2 mixed at this ratio, measured
experimentally (kg/m3)
r_m = 5;             % ramp rate (deg C/min)
T_dwell1 = 650+273;    % maximum temperature set for the reduction (K)
t_p_mix = 30;        % time allocated for powder mixing (minutes)
t_dwell1 = 360;       % dwell time at specified reduction temp (minutes)
t_stir = 24*60;      % time allocated for acid etching step (minutes)

u_c_SiO2 = 3.08/1.3;   % unit cost of SiO2 (kg/£) (1.3 is exchange rate of USD to
GBP)
u_c_Mg = 1.8/1.3;    % unit cost of Mg (kg/£)
u_c_HCl = 1/1.3;     % unit cost of HCl (kg/£)
u_c_energy = 0.0207;       % wholesale cost of natural gas for industry in the UK
is 2.07 pence/kWh. (units in £/kWh)

m_SiO2_feed = Mr_SiO2*m_Si/(Mr_Si*y*eta_p);     % mass of SiO2 feed required,
based on yield and process efficiency (kg)

m_Mg =R_ms*m_SiO2_feed;     % mass of Mg required, given the mass ratio (kg)

n_MgO = 2*m_Si/(eta_p*Mr_Si);      % moles of MgO that will be present in the
product after heating step, based on yield (kmol)

n_Mg_unre = (m_Mg/Mr_Mg)-n_MgO;     % moles of Mg that remains unreacted (kmol)

%% Powder mixer

Q_p_mix = (m_SiO2_feed+m_Mg)*q_mix/rho_tap;     % power requirement of the powder
mixer, based on volume of reactant powder (kW)

h_p_mix = Q_p_mix*t_p_mix*60;  % total energy consumed by the powder mixer in
specified time (kJ)


%% Indirect fired rotary kiln

% Radiative heat loss
```

```
V_RK=(m_SiO2_feed+m_Mg)/(0.15*rho_tap);  % volume of rotary kiln, based on a
typical volume loading of 15% (m3)

S_kiln=6.215*pi*(4*V_RK/(5*pi))^(2/3);    % surface area of the rotary kiln (m2)

D = (4*V_RK/(5*pi))^(1/3); % diameter of the kiln, given a typical
length:diameter ratio of 5:1 (m)

t_lim = 60*(T_dwell1-T_room)/r_m;  % time it takes to reach the specified
reduction temp, given the ramp rate (s)

% The line below this description (h_rad_ramp =) is the integral of the
% radiative heat loss equation. This is to calculate the total heat loss
% during the ramping step. Unit is J.
h_rad_ramp=epsilon*sigma*S_kiln*(((12*(((r_m/60)*t_lim+T_room)^5)/r_m)-
(((T_room)^4)*t_lim))-((12*(((r_m/60)*0+T_room)^5)/r_m)-(((T_room)^4)*0)));

Q_rad_dwell = epsilon*sigma*S_kiln*((T_dwell1^4)-(T_room^4)); % radiative heat
loss at the maximum reduction temperature (W)

h_rad_dwell = Q_rad_dwell*60*t_dwell1; % total heat loss at max reduction temp
(J)

h_rad = (h_rad_ramp + h_rad_dwell)/1000; % total heat loss at ramp and max
reduction temp (kJ)


% Conductive heat loss

% Integral of conductive heat loss equation. This calculates total heat loss
% during ramping step. Unit in J
h_cond_ramp = (k*S_kiln/(0.05*D))*(((30/r_m)*(((r_m*t_lim/60)+298)^2)-
(T_room*t_lim))-((30/r_m)*(((r_m*0/60)+298)^2)-(T_room*0)));

Q_cond_dwell = k*S_kiln*(T_dwell1-T_room)/(0.05*D); % conductive heat loss at max
reduction temp (W)

h_cond_dwell = Q_cond_dwell*60*t_dwell1; % total heat loss at max reduction temp
(J)

h_cond = (h_cond_ramp + h_cond_dwell)/1000; % total conductive heat loss (kJ)


% Convective heat loss

Re = 17*rho_air*D^2/(60*mu);    % Reynolds number for flow of air perpendicular
to the kiln, given a rotational speed of 17 rpm

Nu = 0.027*(Re^0.805)*(Pr^(1/3));   % Nusselt number, assuming turbulent flow
regime

Q_conv_dwell = k_air*Nu*S_kiln*(T_dwell1-T_room)/D;    % convective heat loss (W)

h_conv_dwell = Q_conv_dwell*60*t_dwell1;     %  total convective heat loss (J)

% Heat lost by convection during the ramping step. Integral. Units in J.
```

```
h_conv_ramp = (k*Nu*S_kiln/D)*(((60/(2*r_m))*(((r_m*t_lim/60)+298)^2)-
T_room*t_lim)-((60/(2*r_m))*(((r_m*0/60)+298)^2)-T_room*0));

h_conv = (h_conv_ramp + h_conv_dwell)/1000; % total convective heat loss during
ramp and at max reduction temp (kJ)


% Energy required to heat mass

h_tube = rho_steel*((1.71*pi*D^3)/4)*Cp_steel*(T_dwell1-T_room);   % energy
required to heat the rotary kiln (kJ)

h_SiO2 = m_SiO2_feed*Cp_SiO2*(T_dwell1-T_room);    % energy required to heat SiO2
(kJ)

h_Mg = m_Mg*Cp_Mg*(T_dwell1-T_room);   % energy required to heat Mg (kJ)

h_mass = h_tube+h_SiO2+h_Mg;    % total energy required to heat kiln and reatants
(kJ)

h_kiln = h_rad+h_cond+h_conv+h_mass;    % total energy required by kiln per run
(kJ)

h_supply = h_kiln/eta_therm;    % total energy supplied given thermal efficiency
(kJ)


%% Agitated vessel

n_HCl = 2.2*m_Mg/Mr_Mg; % stoichiometric moles of HCl required, plus an
additional 10% (kmol)

V_HCl = n_HCl*M_HCl; % volume of HCl required (m3)

Q_HCl = V_HCl*q_HCl; % power requirement of the impeller (kW)

h_stir = Q_HCl*t_stir*60; % total energy required by impeller (kJ)

h_cool = (n_Mg_unre*dh_Mg_diss+n_MgO*dh_MgO_diss)*1000; % cooling required to
remove heat from dissolution (kJ)

h_vessel = h_stir+h_cool;   %  energy required by vessel per run (kJ)

%% Dryer

m_prod = (((1-y)*m_Si)/(Mr_Si*y))*Mr_SiO2+m_Si; % total mass of product after
acid etching (kg)

m_ace = 2.56*m_prod;    %total masss of acetone required, assuming product is a
filter cake, with moisture typically weighing 2.33 times the dry product weight
(kg)

h_asens = 31*m_ace*Cp_ace;  % energy required to heat acetone from 25 degC to 56
degC (kJ)

h_avap = m_ace*h_vap;   % energy required to vaporise acetone at 56 degC (kJ)
```

```
h_prod = 31*((1-y)*m_Si/(Mr_Si*y))*Mr_SiO2*Cp_SiO2+31*m_Si*Cp_Si;   % energy
requried to heat product from 25 degC to 56 degC (kJ)

h_dry = h_asens+h_avap+h_prod;  % total energy required by the dryer (kJ)


%% Energy cost

h_proc_total = h_p_mix+h_supply+h_dry+h_vessel; % total energy required by
process for 1 run (kJ)

h_proc_kWh = h_proc_total/3600; % convert J to kWh

h_proc_cost = h_proc_kWh * u_c_energy;  % wholesale cost of natural gas for
industry in the UK is 2.07 pence/kWh. This line gives an answer of total cost of
energy in £

c_energy_specific_cost = h_proc_cost/m_Si;  % cost of energy per kg of Si (£/kg
Si)

%% Feedstock cost

c_SiO2 = u_c_SiO2*m_SiO2_feed;  % total cost of SiO2 (£)

c_Mg = u_c_Mg*m_Mg; % total cost of Mg (£)

c_HCl = u_c_HCl*m_Mg;   % total cost of HCl (£)

c_feed = c_SiO2+c_Mg+c_HCl; % total feedstock cost (£)

c_feed_specific_cost = c_feed/m_Si; % feedstock cost per kg of Si (£/kg Si)


%% Process cost

C_proc_total = h_proc_cost+c_feed;  % total process cost

C_Si_per_kg = c_energy_specific_cost+c_feed_specific_cost; % specific process
cost (£/kg Si)
```